Ageing tests with Gas Electron Multipliers for the ALICE TPC Upgrade

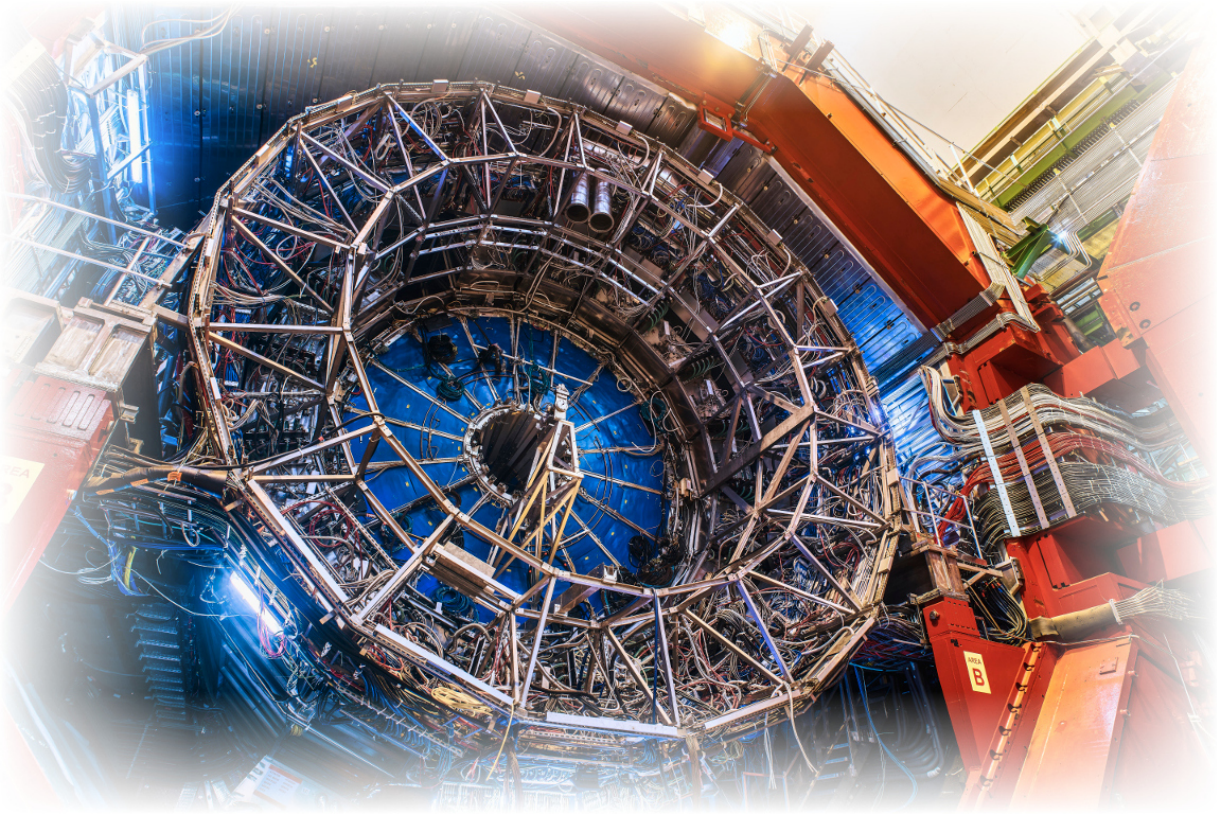

Master thesis

of

Michael Jung

15th May 2019

Goethe University Frankfurt
Department of Physics
Institute for Nuclear Physics

First referee: Prof. Dr. Harald Appelshäuser

Second referee: Prof. Dr. Christoph Blume

"*So today I will lead you into the dark and bloody grounds of anode ageing.*"

Hans Gerhard Fischer - 13$^{\text{th}}$ December 1996
Lecture on Gaseous Detectors
CERN Academic Training Programme

Abstract

During RUN 3 (2021 - 2023) of the Large Hadron Collider, the Time Projection Chamber (TPC) of ALICE will be operated with quadruple stacks of Gas Electron Multipliers (GEMs). This technology will allow to overcome the rate limitation due to the gated operation of the Multi-Wire Proportional Chambers (MWPCs) used in RUN 1 (2009 - 2013) and RUN 2 (2015 - 2018).

As part of the Upgrade project, long-term irradiation tests, so called "ageing tests", have been carried out. A test setup with a detector using a quadruple stack of $10 \times 10\,\mathrm{cm}^2$ GEMs was built and operated in Ar-CO_2 and Ne-CO_2-N_2 gas mixtures. The detector performance such as gas gain and energy resolution were monitored continuously. In addition, outgassing tests of materials used for the assembly process of the upgraded TPC were performed. To reach the expected dose of the GEM-based TPC, the detector was operated at much higher gains than the TPC. It was found, that the GEMs could keep their performance within the projected lifetime of the TPC. Most of the tested materials showed no negative impact on the detector. For the tested epoxy adhesive no certain conclusion could be drawn.

At much higher doses than expected for the upgraded TPC, a new phenomenon was observed, which changed the hole geometry of the GEMs and led to a degradation of the energy resolution. Even though its occurrence is not expected during the lifetime of the GEM-based TPC, simulations were carried out to study this effect more systematically. The simulations confirmed, that a change of the hole geometries of the GEMs, lead to an increase of the local gain variation, which results in a decrease of the energy resolution.

Furthermore the effect of methane as quench gas on GEMs was studied, even though this gas is not foreseen to be used in the TPC. From ageing tests with single-wire proportional counters it is well known that hydrocarbons are produced in the plasma of the avalanches, which cover the electrodes and lead to a degradation of the detector performance. Even though GEMs have a quite different geometry, the ageing tests showed, that also this technology tends to methane-induced ageing. A loss of gas gain as well as a degradation of the energy resolution due to deposits on the electrodes was monitored. A qualitative and quantitative comparison between ageing in GEMs and proportional counters was performed.

Contents

1 The Upgrade of the ALICE TPC **9**
1.1 A Large Ion Collider Experiment . . . 9
1.2 The ALICE Time Projection Chamber . . . 10
1.3 Upgrade with Gas Electron Multipliers . . . 13
1.4 Expected dose of the upgraded TPC . . . 16

2 GEM Ageing Tests **19**
2.1 Experimental setup . . . 20
2.1.1 The gas system . . . 20
2.1.2 The GEM chamber . . . 21
2.1.3 The readout system . . . 23
2.1.4 Calibration of the ADC using argon measurements . . . 24
2.1.5 The LabVIEW software . . . 25
2.1.6 Determination of the gas gain . . . 26
2.1.7 Converting current into charge per area . . . 27
2.1.8 Normalization procedure . . . 28
2.2 Tested components . . . 30
2.3 Long-term measurements in Ar-CO_2 (70-30) . . . 31
2.3.1 Measurement testing the empty outgassing box, screws and frames . . . 31
2.3.2 Measurement testing the epoxy adhesive . . . 38
2.3.3 Measurement testing the resistors and the solder cleaned with acetone . . . 40
2.4 Long-term measurements in Ar-CH_4 (95-5) . . . 42
2.5 Long-term measurements in Ne-CO_2-N_2 (90-10-5) . . . 47

3 Etching Simulations using Garfield^{++} **49**
3.1 Simulated setup and GEM hole geometries . . . 49
3.2 Calculation of the electric field . . . 50
3.3 Garfield^{++} simulations . . . 51
3.4 Results of the simulations . . . 52
3.4.1 Amplification of the different degrees of etching . . . 52
3.4.2 Distribution of the electron avalanche inside a GEM hole . . . 53
3.4.3 Combination of different degrees of etching . . . 54
3.4.4 Ending of the drift of the produced ions on the top electrode . . . 56

4 Comparisons and Conclusions **59**
4.1 The etching process in GEMs . . . 59
4.1.1 Comparison between measurements and simulations . . . 59
4.1.2 Measurements made by the RD51 Collaboration . . . 61

4.1.3 Conclusions concerning the etching phenomenon 61
4.2 CO_2- and CH_4-induced ageing in GEMs 62
4.3 CH_4-induced ageing in proportional counters and GEMs 63
4.3.1 The ageing rate *R*' 63
4.3.2 Converting accumulated charge per area into charge per length 63
4.3.3 Gain drops of the GEM measurements performed in Ar-CH_4 65
4.3.4 Comparison of proportional counters and GEMs 66

5 Summary **69**

Acknowledgments **71**

Appendices

Appendix A Number of produced electrons per 5.89 keV X-ray **75**

Appendix B Determination of the irradiated areas **77**
B.1 Measurement of the profile of the ^{55}Fe source 77
B.2 Mean free paths of 5.89 keV X-rays in gas mixtures 79
B.3 Calculation of the irradiated areas 81

Appendix C Additional measurements in Ar-CO_2 (70-30) **83**
C.1 First measurement with empty box, screws and frames 83
C.2 Second measurement with empty box and frames 84
C.3 Second measurement testing the epoxy adhesive 88
C.4 Measurement testing the SMDs painted with PU 89

Appendix D Additional measurements in Ar-CH_4 (95-5) **91**
D.1 First part of the measurement presented in section 2.4 91
D.2 Second measurement with empty outgassing box 92

Bibliography **100**

List of Figures **103**

List of Tables **105**

List of Abbreviations **107**

Chapter 1

The Upgrade of the ALICE TPC

This chapter will give a short introduction into the physics program of ALICE in section 1.1, before a more detailed introduction into the physics of gaseous detectors will be given. The focus will be kept on the operation and the limitation of Multi-Wire Proportional Chambers in section 1.2 and the working principles of Gas Electron Multipliers in section 1.3. In section 1.4 an upper limit of the expected dose of the upgraded TPC within its projected lifetime will be calculated.

1.1 A Large Ion Collider Experiment

ALICE is an acronym for A Large Ion Collider Experiment and is an experiment located at the Large Hadron Collider (LHC) at CERN. It's main goal is to study strongly interacting matter at extreme temperatures and energy densities with high-energy heavy-ion collisions. If there is a sufficiently high temperature and density during a collision, the nuclei will undergo a transition from hadronic matter to the so called Quark-Gluon Plasma (QGP). ALICE is optimized to study the properties of the QGP as well as its transition to nuclear matter via nucleus-nucleus (especially Pb-Pb) collisions. [1, p. 1]

Since gluons themselves carry color charge, they do not only mediate the strong nuclear force, but also participate in the strong interaction. This leads to a dependence of the strong coupling constant α_s on the distance of objects carrying color charge. At large distances, α_s is strong, which results in the confinement of quarks and gluons into color-neutral objects, such as protons and neutrons, forming normal nuclear matter. At low distances however, the strong nuclear force becomes weak. This, together with a high energy density, leads to the deconfinement of quarks and gluons, which is also called asymptotic freedom and results in a QGP. [2, p. 181 ff.]

The study of a QGP is not only interesting for nuclear physics, but also for cosmological and astrophysical reasons. Cosmology says that extreme temperatures and densities which are necessary for the creation of a QGP prevailed in the early universe, a few microseconds after the big bang. Unfortunately the cosmological QGP is shielded from astronomical observations, due to the subsequent evolution of the universe. In addition, astrophysics predicts that a QGP could also exist in the core of neutron stars, which is also outside the scope of today's measurement. The only known way to study the QGP, is in the laboratory using heavy-ion experiments. [1, p. 1]

During RUN 1 and RUN 2 the LHC delivered Pb-Pb collisions at a center-of-mass energy per nucleon pair $\sqrt{s_{\mathrm{NN}}}$ of 2.76 TeV and 5.02 TeV respectively [3, p. 1]. In addition other collision systems like pp, p-Pb and Xe-Xe at the same as well as lower energies were studied. In this way the interaction volume and the energy densities of the collisions could be varied. Since the

creation of a QGP is only expected in heavy-ion collisions, one can discriminate between effects coming from the QGP or its transition to nuclear matter and pp or p-Pb physics. Therefore these collision systems function as references for the heavy-ion program. [1, p. 1]

To investigate the collisions of heavy ions, the ALICE experiment consists of individual detectors based on different technologies, such as gas detectors, electromagnetic calorimeters, silicon detectors, time of flight detectors and transition radiation detectors. They are build around one of the four interaction points where the two LHC beams collide, as one can see in Figure 1.1. With their different geometries and distances to the interaction point, the detectors can identify particles and measure their properties, such as momentum and charge, as well as their abundances. [4, p. 1 f.]

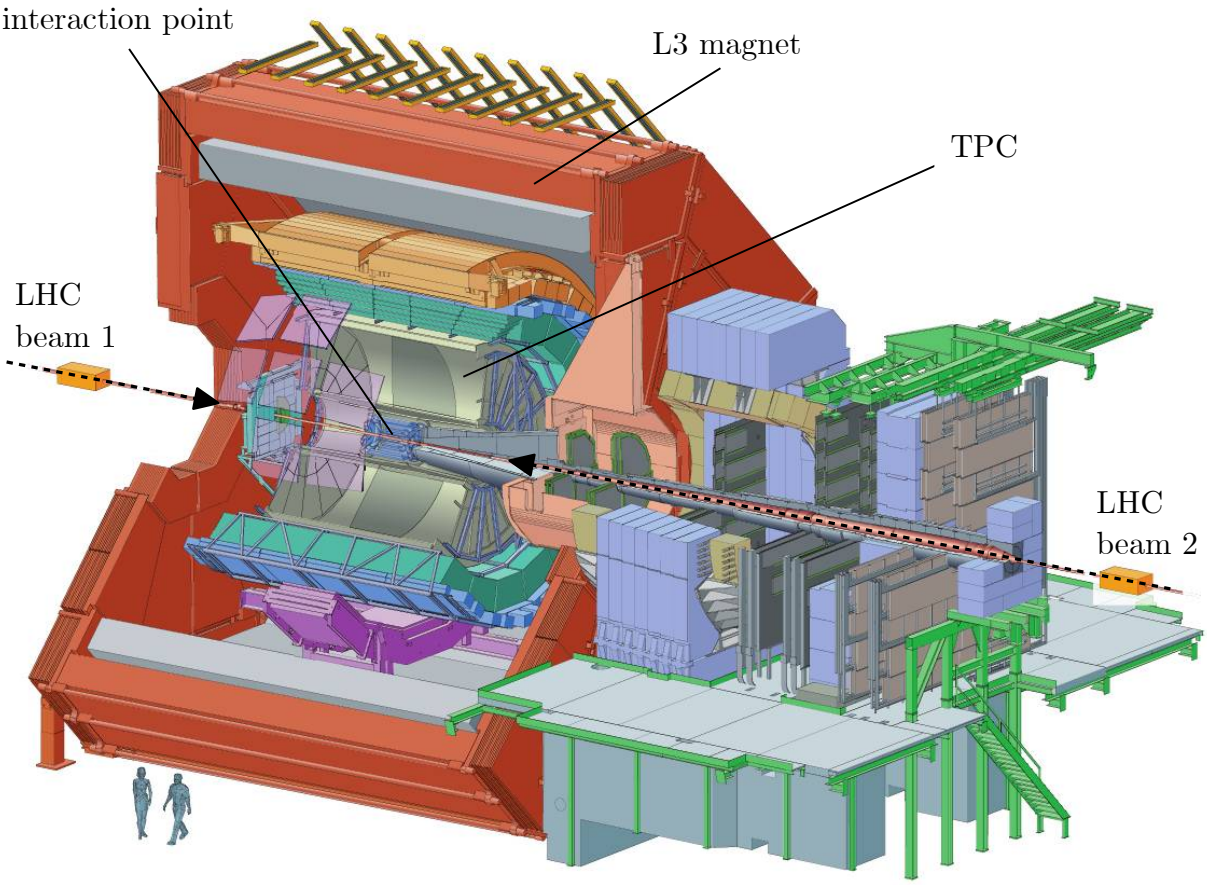

Figure 1.1: Schematic drawing of ALICE, adapted from [4, p. 4].

The results of the measurements are compared to predictions of theoretical models. In this way physical insights into the properties of the QGP can be obtained. Main goals in this field are for example the determination of transport coefficients and the equation of state [5, p. 2].

1.2 The ALICE Time Projection Chamber

The Time Projection Chamber (TPC) is the main device for tracking of charged particles and for particle identification in ALICE. It is optimized to provide high precision momentum and $\mathrm{d}E/\mathrm{d}x$ measurements even at high particle densities in central Pb-Pb collisions. [5, p. 84]

In Figure 1.2 (a), a schematic drawing of the TPC is shown. One can see that the chamber is built as a cylinder which is centered at the interaction point of the two LHC beams. The drawing can be compared to the picture of the TPC, taken during its relocation into the clean room, shown in Figure 1.2 (b).

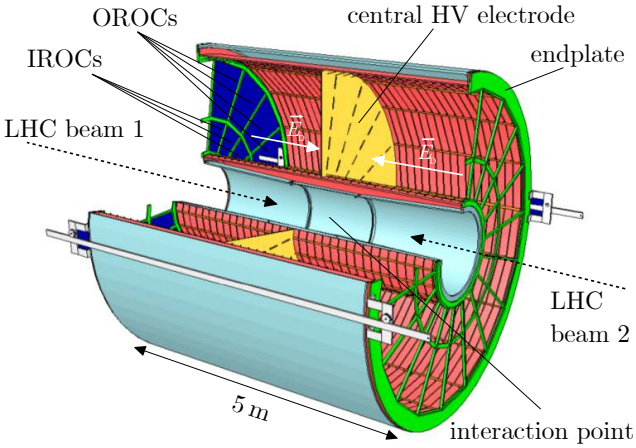

(a) Schematic drawing of the TPC, installed in ALICE.

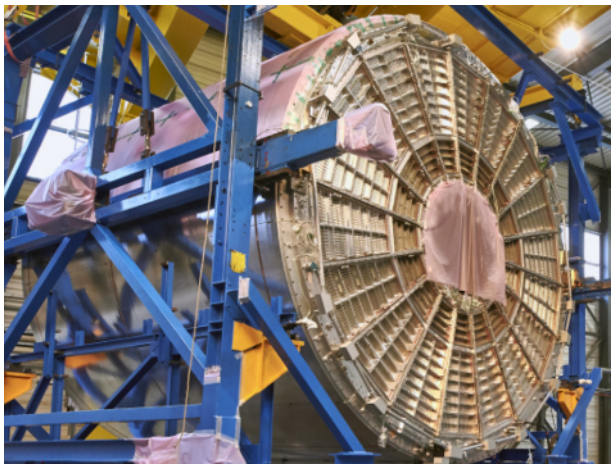

(b) Picture of the TPC, moving into the clean room.

Figure 1.2: The ALICE Time Projection Chamber, schematic drawing adapted from [6, p. 7], picture cut out from [7].

The particles produced by the collisions will cross the TPC, if they leave the interaction point under an angle greater than 18°. All charged particles which go through the TPC will ionize the detector gas along their trajectories due to inelastic collisions with the gas molecules. The number of electron-ion pairs produced in this way is proportional to the amount of energy deposited. This energy deposition per unit length ($\mathrm{d}E/\mathrm{d}x$) is described by the Bethe-Bloch formula and depends strongly on the charge and velocity of the particles traversing the detector. In order to measure the number of electron-ion pairs one has to separate them to avoid recombination. To do so the detector has a central high voltage (HV) electrode which is made of a thin membrane and located at the axial center of the cylinder. With its potential of -100 kV it provides a constant and uniform electric drift field E_D of 400 V/cm across the complete 90 m^3 gas volume. Because of this field the ions will drift towards the central HV electrode whereas the electrons will drift to the Readout Chambers (ROCs) which are mounted on the endplates of both sides of the TPC. These ROCs are subdivided into Inner and Outer Readout Chambers (IROCs and OROCs) and base on the Multi-Wire Proportional Chamber (MWPC) technique with pad readout. In the MWPCs, the electrons are amplified with a gas gain near 10 000 to produce a measurable electric signal. [8, p. 317 f.]

In this way it is possible to measure the projection of the trajectories produced by the particles, to determine their curvature caused by the magnetic field of the L3 magnet and to identify the amount of energy deposited per unit length. With these measurements in combination it is possible to calculate the properties of the particles such as mass, momentum and charge.

The MWPCs of the TPC consist of three different wire grids as it is shown in Figure 1.3. The first layer is the so called gating grid, which can be operated in two different modes. In the so called open gate mode (transparent mode), the potential of the gating grid is set to a constant voltage U_G to admit the incoming electrons to the amplification region. If the gating grid is in

closed mode, the wires are biased with a bipolar field of $U_G \pm 90\,V$ to prevent the ions produced in the amplification region from drifting back into the drift volume. At the same time, electrons coming from the active volume of the detector are also blocked, which results in a dead time of the detector.

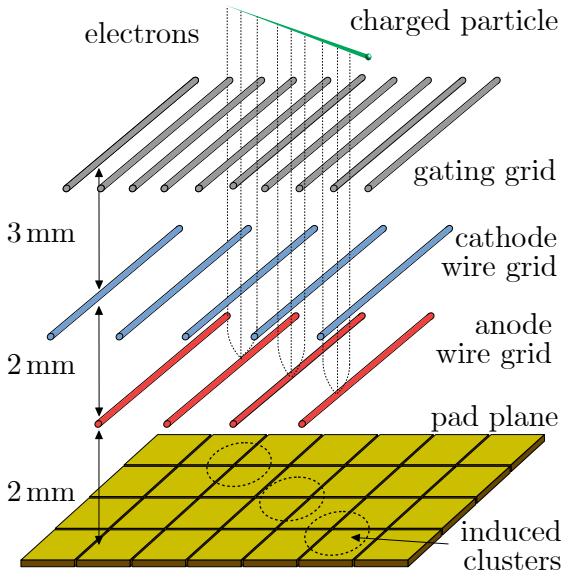

Figure 1.3: Wire geometry of the TPC using the example of an IROC.

After the electrons passed the open gating grid, they will drift towards the anode wire grid and get amplified as one can see in Figure 1.4. Since the electric field strength of the wire is inversely proportional to the distance r ($E \sim 1/r$), the incoming electrons will be accelerated towards the anode and produce an electron avalanche as it is shown in Figure 1.4 (a). In this

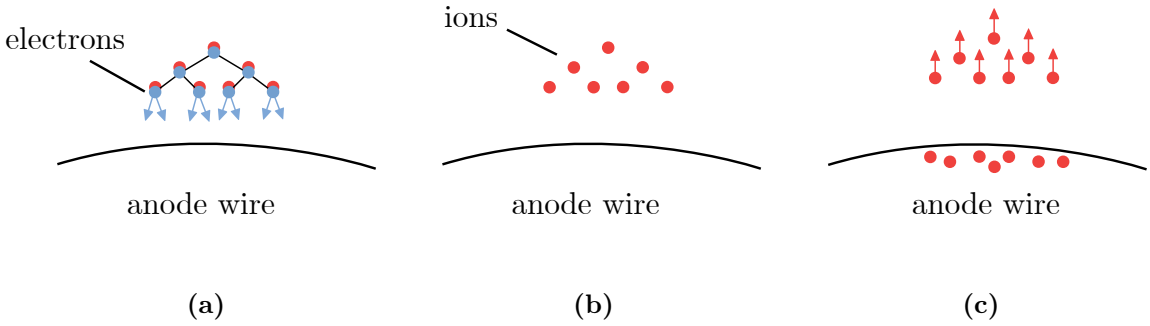

Figure 1.4: Development of an electron avalanche close to an anode wire.

simplest approximation it is assumed, that every electron will produce two more electrons, so that 50 % of the charge in the avalanche is produced in the last mean free path very close to the electrode ($\sim 1\,\mu m$). Due to this short distance, the electrons will end on the electrode quickly after their creation ($< 1\,ns$), as one can see in Figure 1.4 (b). In addition, the electron cloud will also induce an electric signal in the electrodes, but due to their short drift distance the signal is negligible. The ion cloud on the other hand has a drift distance of several micrometers, which

results in a much larger induced signal than the one of the electron cloud. These signals are not only induced in the anode wires as indicated in Figure 1.4 (c), but also in the pad plane and the cathode. Since the signals induced in the anode and cathode grid do not help to reconstruct the trajectories of the particles, only the induced clusters from the pad plane are read out, as one can see in Figure 1.3.

The ions produced by the avalanche at the anode grid will drift towards the pads, the cathode grid or the gating grid. To prevent the ions from drifting back into the drift volume, the gating grid has to be in closed mode, as soon as the ions arrive at the gating wires. Otherwise the ions would create space charge distortions in the TPC which would disturb the drifting electrons. The big advantage of the gating grid is, that the efficiency of the gate in closed mode is better than 0.01 %. The disadvantage of the gate is, that it produces a dead time of the detector which can be calculated by the drift time of the ions and electrons. The ions have to drift from the anode wire to the gating grid which takes about 180 µs in Ne-CO_2-N_2 (90-10-5)[1]. Together with the open time of the gating grid of about 100 µs, which is the maximum drift time electrons need to reach the ROCs starting close to the central HV electrode, this results in a maximum rate of about $f = 1/280\,\mu s \approx 3.5\,kHz$ for the IROCs[2]. [9, p. 3]

1.3 Upgrade with Gas Electron Multipliers

Because of the LHC upgrade project during the long shutdown 2, the accelerator will for RUN 3 deliver Pb-Pb collisions with a rate of about 50 kHz instead of 8 kHz. Since the TPC has a limitation of 3.5 kHz due to the gating grid and was running at about 700 Hz due to the current electronic readout limit, it will also be upgraded. To make use of the future high rate, the MWPCs will be replaced by quadruple stacks of Gas Electron Multipliers (GEMs), which will allow an ungated operation. Together with faster electronics, the TPC will then run in a continuous readout mode. [9, p. 3]

A cross section of a GEM is shown in Figure 1.5 (a). It consists of a 50 µm thick insulating kapton layer which is metallized on both sides with a 5 µm thick copper layer. These metallic layers serve as electrodes and are named top and bottom electrode. Due to the double-conical shape of the holes, which are etched into the GEMs, one has an inner and outer diameter of about 50 µm and 70 µm respectively. This can be seen in the top view of the GEM in Figure 1.5 (b). Another parameter is the distance between the holes, which is called pitch and set to 140 µm for the standard GEM configuration. [9, p. 15]

The production of the foils is realized with a photo-lithographic procedure, which etches double-conical holes into the GEMs. The GEM is painted with photo-resist and is exposed to UV light through a mask which defines the hexagonal pattern of the holes. Afterwards only the photo-resist which was exposed to light can be removed, whereas the rest of the photo-resist remains on the surface. Now the metal layers are exposed to acid to remove the copper which is not covered by photo-resist. After cleaning, the holes in the copper electrodes define the pattern for the etching of the insulator. The kapton is etched from both sides, so that double-conical holes will be produced. [11, p. 531] [12, p. 7]

The major idea of GEMs is, that if one puts an electric potential difference between the top and bottom electrode, the electric field inside of the holes is high enough to produce electron

[1] Ne-CO_2-N_2 (90-10-5) means that 5 % of N_2 was added to Ne-CO_2 (90-10). The normalized ratio of this gas mixture is (85.7-9.5-4.8).

[2] The OROCs have a distance between anode grid and gating grid of 6 mm instead of 5 mm which results in a higher drift time ($\sim$ 336 µs) and therefore in a little bit lower rate of about 3 kHz.

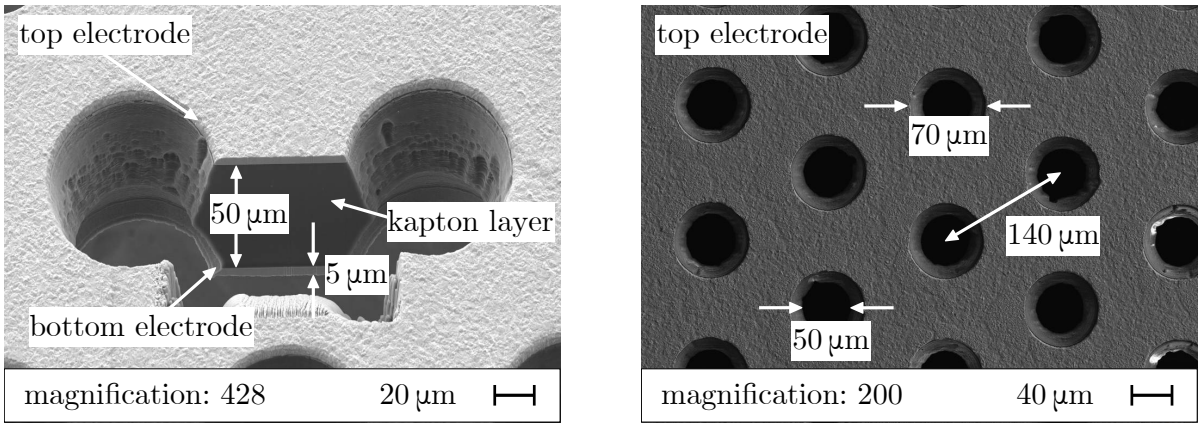

(a) Cross section of two GEM holes.

(b) Top view of a GEM.

Figure 1.5: Images of a GEM made by a Scanning Electron Microscope. Images adapted from [10, p. 10, 12].

avalanches. Electric drift lines can be seen in Figure 1.6 (a). The drift lines are bent from one electrode into the hole and than to the other electrode. Inside the hole, an electric field strength of about 50 kV/cm is achieved applying a voltage of $\Delta U_{\mathrm{GEM}} = 300\,\mathrm{V}$. In Figure 1.6 (b)

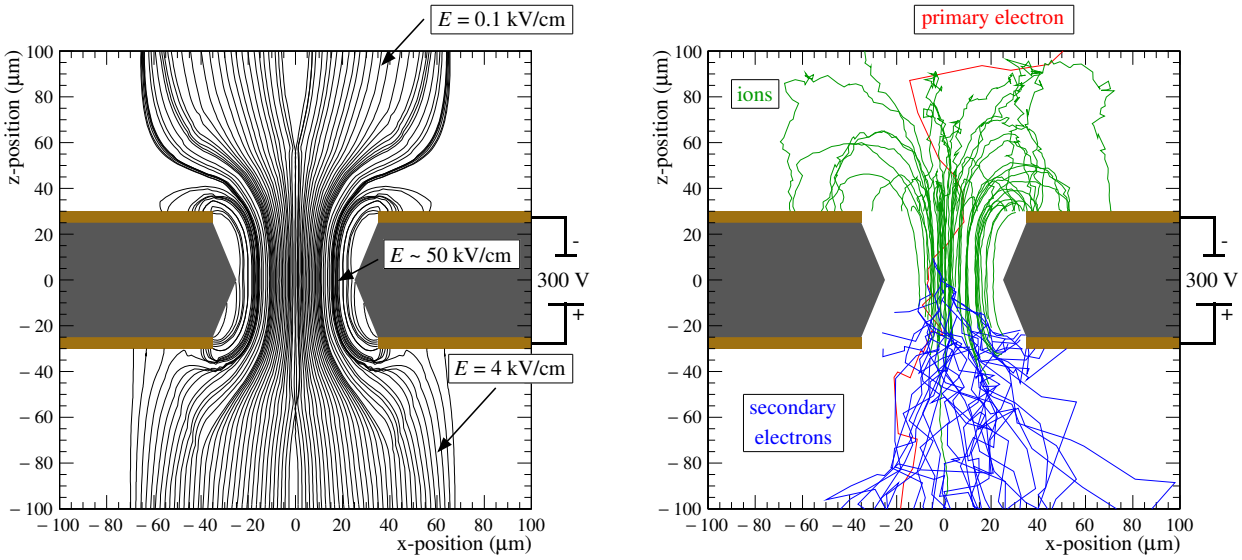

(a) Electric drift lines inside a GEM hole.

(b) Example of one electron entering a GEM hole.

Figure 1.6: 2-dimensional projections of a 3-dimensional simulated single GEM hole.

the simulation of a single electron entering a GEM hole is shown. The primary electron (red) is drifting into the hole and gets accelerated, producing an avalanche of secondary electrons (blue). The number of produced electrons divided by the amount of incoming electrons is called multiplication. It is different from the gain, which is defined by the number of *extracted* electrons divided by the number of primary electrons. Multiplication and gain can be tuned by ΔU_{GEM} as well as by the ratio of the electric field strength inside and beneath the GEM. In contrast to

the ions (green), the drift way of the electrons is dominated by diffusion. By comparing the two Figures 1.6 (a) and (b), one can see that the movement of the ions, especially at high fields, is specified by the electric field lines.

In order to reduce the amount of ions, which can drift back into the drift volume, four GEMs are mounted together in a stack. In this way many ions produced in the lower GEMs will be absorbed by one of the electrodes above. Because of this intrinsic Ion Backflow (IBF) suppression, one can avoid large space charge distortions in the drift volume, without a gated operation. Simulations showed that an IBF of less than 1 % must be achieved by the new amplification system to keep the distortions at a tolerable level. [13, p. 7]

The IBF can be further tuned by mounting GEMs in a stack with different pitches. For the upgrade project of the TPC, GEM foils with four different hole pitches were studied, as one can see in Table 1.1. After detailed Research & Development (R&D) studies it was found that

Name of the foil	Acronym	Pitch
Small Pitch	SP	90 µm
Standard	S	140 µm
Medium Pitch	MP	200 µm
Large Pitch	LP	280 µm

Table 1.1: Overview of the different GEM pitches.

a stack of S-LP-LP-S GEMs can provide a good IBF, depending on the voltage settings. A schematic drawing of such a stack is shown in Figure 1.7. The GEMs are numbered from 1 to 4 starting with the topmost GEM. The electric fields between the GEMs as well as between GEM4 and pad plane are called transfer fields (E_T). They are also numbered from 1 to 4, starting with the field between GEM1 and GEM2. With such a S-LP-LP-S configuration it is also possible to achieve the other requirements for the upgrade, such as operational stability and an energy resolution $\sigma(^{55}\text{Fe})$ better than 12 % using X-rays with an energy of 5.89 keV.

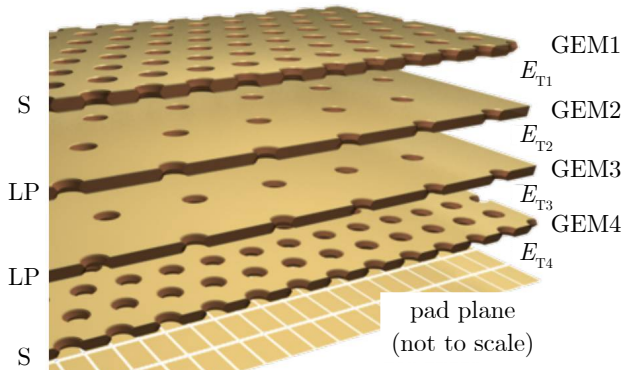

Figure 1.7: GEM stack with the S-LP-LP-S configuration, adapted from [14, p. 10].

By operational stability one understands the stability of the detector in terms of HV, gain and electrical discharges. In addition to the good IBF suppression of a GEM stack, one can also improve the HV stability by sharing the gain of the system between four GEM foils to achieve the total gain of 2000, which is required for a signal-to-noise ratio of 20 in Ne-CO_2-N_2 (90-10-5).

The energy resolution can be measured from the pulse-height spectrum of the 5.89 keV X-rays emitted from a ^{55}Fe source, as one can see in Figure 1.8. It is defined as the ratio of the standard

deviation σ of the photo peak, divided by its position. The smaller the photo peak is, the less fluctuations in the amplification process took place and the better the statistics of the primary electrons is maintained. This leads to a good capability of the detector to discriminate between two individual incoming signals. With an energy resolution of $\sigma(^{55}\mathrm{Fe}) = 12\,\%$, the new GEM system will be able to preserve the $\mathrm{d}E/\mathrm{d}x$ resolution of RUN 1 and RUN 2. [9, p. 17]

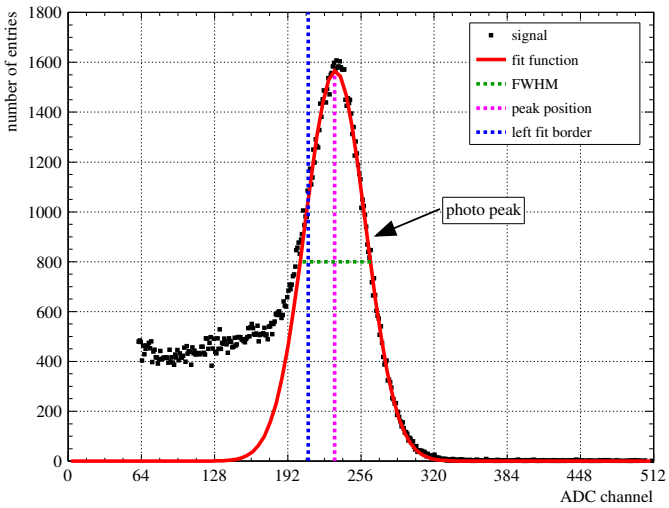

Figure 1.8: Pulse-height spectrum of a ^{55}Fe source in Ne-CO_2-N_2 (90-10-5).

Even if these properties can be achieved with a quadruple GEM stack, the capability of such a stack to keep its performance over the projected lifetime of the upgraded TPC had to be validated. Since changes in the performance of gaseous detectors do not depend on the time the detector is used, but on the amount of charge the amplification system has to face, one has to estimate the amount of charge the detector has to deal with.

1.4 Expected dose of the upgraded TPC

To estimate the total dose of the GEM-based TPC, the estimated charge per length given for the MWPCs in RUN 1 was used and corrected by the different conditions of RUN 3. The maximum dose per cm of anode wire was estimated to be $2.3 \cdot 10^{-13}\,\mathrm{mC/cm}$ per central Pb-Pb collision event in RUN 1 *before* amplification. With an anode wire pitch of 0.25 cm this makes a charge per area of $9.2 \cdot 10^{-13}\,\mathrm{mC/cm^2}$. For the estimation of the dose per cm of anode wire, a charged-particle multiplicity per unit of pseudorapidity $\mathrm{d}N_{\mathrm{ch}}/\mathrm{d}\eta$ of 8000 was assumed. Multiplicity refers to the number of particles and pseudorapidity describes the angle of the particles relative to the beam axis. [15, p. 45, 154 f.]

Since the LHC will run at its design energy in RUN 3, the center-of-mass energy per nucleon-nucleon pair for Pb-Pb will increase to 5.52 TeV. The estimated multiplicity for central Pb-Pb collisions in RUN 3 is 2000 [13, p. 5]. With the the Pb-Pb interaction rate of 50 kHz and the gain of the quadruple GEM stack of 2000, one can calculate the expected dose of the upgraded TPC. Since 90 % of the interactions are minimum-bias events, which are considered to have a multiplicity 5 times lower than central events, this has to be corrected [15, p. 154 f.]. The dose

for three weeks of Pb-Pb collisions calculates to:

$$Q/A_{\mathrm{Pb-Pb}} = \frac{1}{5} \cdot 9.2 \cdot 10^{-13} \,\frac{\mathrm{mC}}{\mathrm{cm}^2} \cdot \frac{2000}{8000} \cdot 2000 \cdot 50\,\mathrm{kHz} \cdot 1\,814\,400\,\mathrm{s} = 8.35\,\frac{\mathrm{mC}}{\mathrm{cm}^2} \tag{1.1}$$

For pp collisions the maximum dose was estimated to be $2.3 \cdot 10^{-16}\,\mathrm{mC/cm}$, which makes $1.15 \cdot 10^{-16}\,\mathrm{mC/cm^2}$. Since the multiplicity for pp collisions is assumed to be 1000 times lower than for Pb-Pb minimum-bias events, the number of charged particles per pseudorapidity is about $(1/5 \cdot 8000)\,/\,1000 = 1.6$ for RUN 1. [15, p. 154 f.]

For RUN 3, $\mathrm{d}N_{\mathrm{ch}}/\mathrm{d}\eta$ can be extrapolated to $\sqrt{s} = 14\,\mathrm{TeV}$ using the fit in [16, p. 321]. This gives an estimation of the charged-particle multiplicity of about 5.4 for RUN 3. With an interaction rate of about 200 kHz [5, p. 10] the dose of 40 weeks of pp collisions calculates to:

$$Q/A_{\mathrm{pp}} = 1.15 \cdot 10^{-16}\,\frac{\mathrm{mC}}{\mathrm{cm}^2} \cdot \frac{5.4}{1.6} \cdot 2000 \cdot 200\,\mathrm{kHz} \cdot 24\,192\,000\,\mathrm{s} = 3.76\,\frac{\mathrm{mC}}{\mathrm{cm}^2} \tag{1.2}$$

The total dose within the projected lifetime of the upgraded TPC of 10 years calculates to:

$$Q/A_{\mathrm{total}} = 10 \cdot \left(8.35\,\frac{\mathrm{mC}}{\mathrm{cm}^2} + 3.76\,\frac{\mathrm{mC}}{\mathrm{cm}^2}\right) = 121.10\,\frac{\mathrm{mC}}{\mathrm{cm}^2} \approx 121\,\frac{\mathrm{mC}}{\mathrm{cm}^2} \tag{1.3}$$

For this estimation it was assumed, that the LHC in RUN 3 will run for 43 weeks per year at its design energy, excluding 9 weeks per year for technical stops and shutdowns. Furthermore, and most importantly, it was assumed that there will be a yearly heavy-ion period of three weeks performed completely with Pb-Pb collisions, resulting in 30 weeks of operation in 10 years. According to [5, p. 11], about 15 weeks of Pb-Pb collisions in RUN 3 are required to fulfill the Pb-Pb program. Therefore the calculated dose only represents an upper limit. Nevertheless, within this work, $121\,\mathrm{mC/cm^2}$ will be referred to as the lifetime of the upgraded TPC.

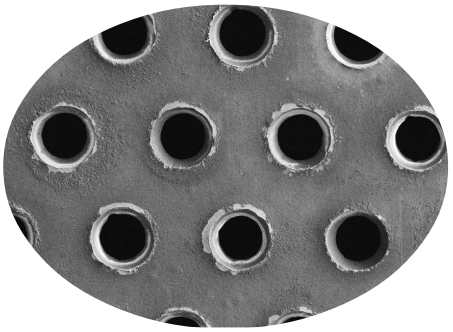

Chapter 2

GEM Ageing Tests

Under ageing of gaseous detectors one understands the radiation-induced degradation of the detector performance. It is a continuous and complex process which starts already with the first usage of the detector and leads to different effects like self-sustained discharges, increasing of dark currents, lowering and non-uniformity of the gas gain and loss of the pulse-height spectrum resolution. Due to the decomposition of the gas molecules in the plasma of the avalanche and the deposition of the different chemical components on the electrodes, ageing depends strongly on the gas mixture used in the detector and/or on impurities in the gas. The pollution of the gas can, among other things, come from the gas system itself, contamination of the detector during the assembly process and outgassing from materials used in the detector. [17, p. 73]

These phenomena were observed because of the intensive studies carried out since the invention of MWPCs introduced in [18] in 1968 by G. Charpak and its more common usage in high energy physics since the 1970s. In 1986 the first workshop about "radiation damage to wire chambers" was held at LBL[1] in Berkeley, summarizing the knowledge about ageing in wire chambers at this time, see [19]. Due to the development of new technologies like large scale straw-type detectors, micro-strip gas detectors and micro pattern gas detectors as well as high luminosity accelerators, a second workshop was held in 2001 at DESY in Hamburg, see [20]. Since the invention of GEMs in 1997 by F. Sauli was only 4 years before, the ageing of GEM detectors was covered by only three talks in the second workshop. Even if some papers about ageing in GEM detectors were published until now, the overall data about ageing in GEM structures is very limited. In addition it is important to know that the monitoring of the pulse-height spectrum resolution is only important for experiments which want to do particle identification via $\mathrm{d}E/\mathrm{d}x$ measurements. This is the reason why only some of the GEM ageing tests measured this quantity, like [21] and [22].

To study the radiation-induced degradation of the performance of a GEM detector, a test setup was built by the ALICE TPC Upgrade Collaboration. This detector was used to perform long-term ageing tests in the laboratory of the CERN Research and Development (R&D) project RD51 with settings tuned to the requirements of the upgraded TPC. This means the setup had to monitor the gain as well as the energy resolution of the detector, accumulate a large dose ($\gg 121\,\mathrm{mC/cm^2}$), operate with gas mixtures which will be used in the future TPC and run under controlled environmental conditions. The experimental setup will now be explained in detail, before the results of the long-term measurements will be presented.

[1] The Lawrence Berkeley Laboratory (LBL) is today named Lawrence Berkeley National Laboratory (LBNL).

2.1 Experimental setup

The detector was built into a chamber which was placed inside of a copper box to shield the laboratory from the radiation used in the setup. The box with the GEM chamber and some corresponding equipment like temperature and pressure sensor[2], ammeter and ^{55}Fe source can be seen in Figure 2.1 (a). On the right from the copper box the NIM[3] crates with high voltage power supplies and main amplifier as well as the gas control with flowmeter, outgassing box and oxygen sensor were placed. This is shown in Figure 2.1 (b). Further to the right a desk with the PC is located to control and monitor the setup.

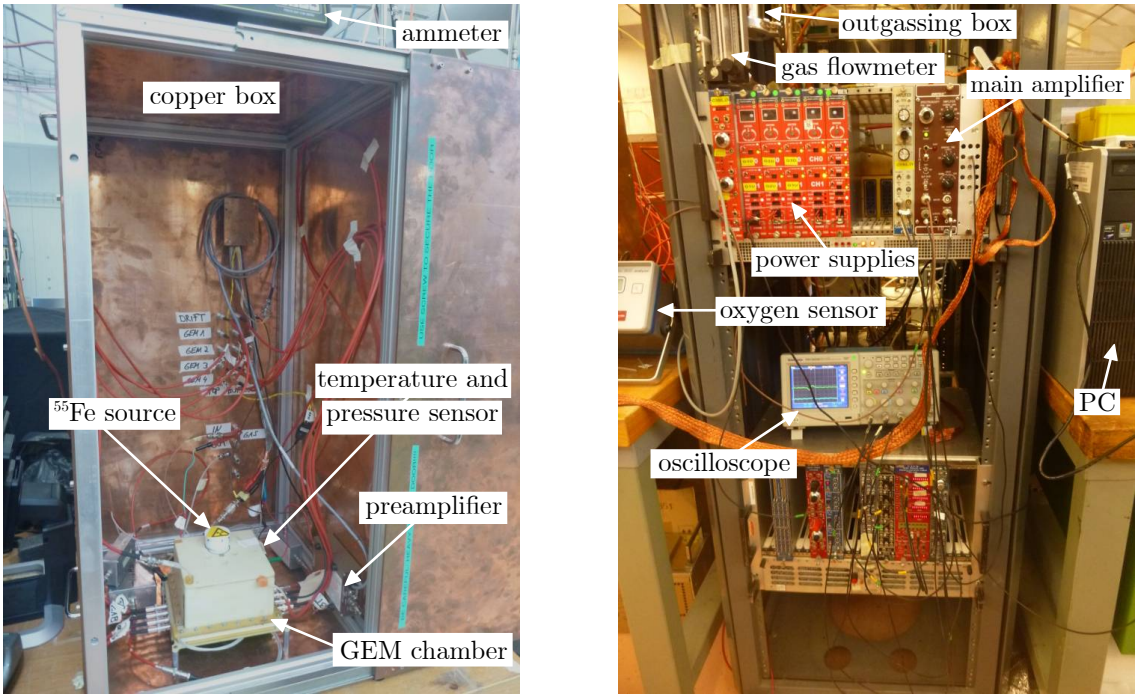

(a) GEM chamber in the copper box.

(b) Power supplies and electronics.

Figure 2.1: Experimental setup in the RD51 laboratory.

The different components of the experiment like gas system, GEM chamber, electronic read-out, calibration, LabVIEW software, the determination of the gain, as well as the normalization procedure for the measured data will now be explained in detail.

2.1.1 The gas system

During the experiment three different premixed gas mixtures were used: Ne-CO_2-N_2 (90-10-5), Ar-CO_2 (70-30) and Ar-CH_4 (95-5). Even if the upgraded TPC will be operated in a neon-based gas mixture, the long-term ageing measurements were performed above all in an argon-based mixture, because argon is much cheaper. Since noble gases do not undergo chemical reactions due to their inertness, they do not participate in the polymerization process in the plasma of

[2] The temperature and pressure sensor was taped to the right wall of the field cage (not visible in the picture).
[3] Nuclear Instrumentation Module.

the avalanche. For testing the outgassing of materials it is therefore possible to replace the neon component with argon, without adulterating the measurements.

A flow diagram of the gas system can be seen in Figure 2.2 starting with the gas bottle. The gas bottles were connected via a pressure reducer and a stainless steel pipe ($\sim 6\,\mathrm{m}$) to the gas panel on the backside of the laboratory. From there a 10 m long plastic pipe brought the gas towards the experimental setup. This plastic pipe was replaced by a stainless steel pipe after the first long-term measurement to reduce the amount of oxygen as well as the water content in the gas. In order to have some flexibility close to the setup, the 10 m stainless steel pipe was extended with a 1.5 m long copper pipe which was connected to the gas flowmeter[4]. With the

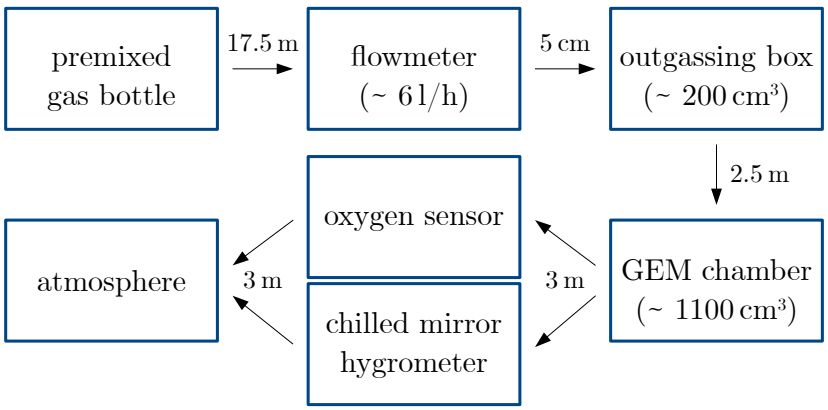

(a) Block diagram of the gas system.

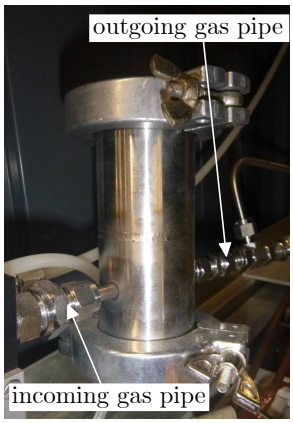

(b) Outgassing box.

Figure 2.2: Overview of the gas system.

flowmeter the amount of gas entering the detector was controlled and tuned to a constant flow of about 6 l/h. Very close to the flowmeter ($\sim 5\,\mathrm{cm}$) the outgassing box was installed, which can be seen in Figure 2.2 (b). This box is made of stainless steel, has a volume of about $200\,\mathrm{cm}^3$ and was used to test different materials of the assembly process concerning their outgassing behavior. Afterwards the gas was again flushed through a copper pipe ($\sim 2\,\mathrm{m}$) and entered the copper box from the backside. In there the GEM chamber was connected via a 50 cm long plastic pipe to the gas system. After the chamber was flushed, a second 50 cm long plastic pipe was connected to the backside of the copper box. Outside, another copper pipe ($\sim 2.5\,\mathrm{m}$) brought the gas to an oxygen sensor[5] or an hygrometer[6], depending on the available equipment. Afterwards the gas was vented into the atmosphere through a copper pig tail ($\sim 3\,\mathrm{m}$).

2.1.2 The GEM chamber

In Figure 2.3 (a) a cross section of the GEM chamber is shown. The radioactive source[7] was put on top of the chamber and its opening was aligned with the little hole in the field cage to avoid absorption of emitted X-rays in the Rohacell. If it was centered, the X-rays only had to pass a thin aluminized mylar inside the field cage, which functioned as the cathode and separated the

[4] "Variable area flowmeter" V-100 from Vögtlin Instruments AG.
[5] 3600 Analyzer for Oxygen from Orbisphere.
[6] DewMaster Chilled Mirror Hygrometer from EdgeTech.
[7] The ^{55}Fe source had 1.11 GBq measured on 1st September 2012 (RP 4540).

gas volume from the atmosphere. After the X-rays passed the cathode, they entered the 1000 cm^3 drift volume and produced electron-ion pairs due to photoelectric absorption. To separate the produced charges an electric drift field E_D was applied and transported the ions to the cathode and the electrons towards the GEM stack. This electric field was produced by field strips, which were connected to each other via a resistor chain as one can see in Figure 2.3 (b). The first strip as well as the cathode were powered by a programmable HV power supply[8] with a maximum output voltage of ± 5.5 kV. Because of the voltage drop after each resistor, the strips had a different electrical potential. The so called resistor to ground R_G was the last resistor in the chain and was placed outside of the detector to allow an exchange of the resistance without opening the chamber. With this resistance, the potential of the last strip could be tuned to a similar voltage as the electrode of GEM1 Top. Since its potential changed with the voltage settings e.g. for different gas mixtures, a certain flexibility was useful. Because the distance between last strip and GEM1 Top was quite low, one had to limit the potential difference to avoid discharges.

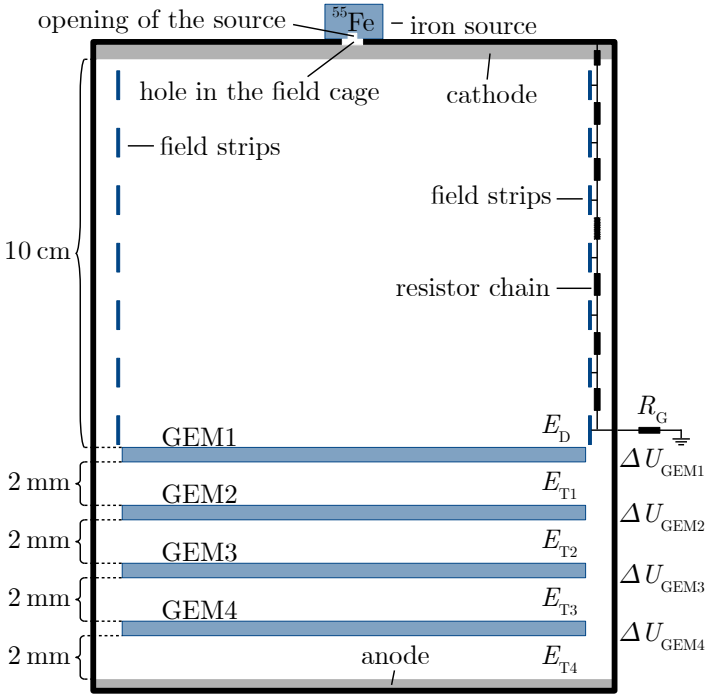

(a) Schematic drawing of the GEM detector.

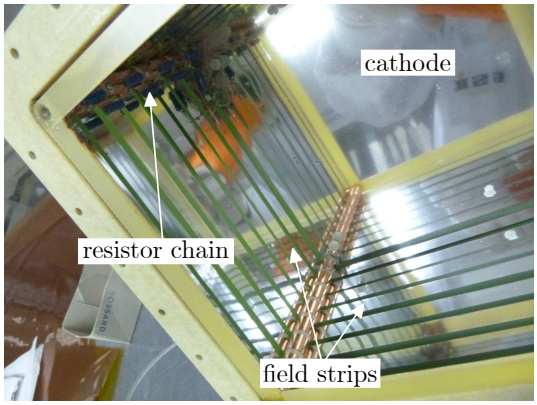

(b) Picture of the field cage.

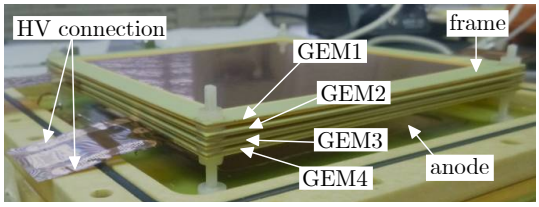

(c) Picture of the GEM stack.

Figure 2.3: The GEM detector used for the ageing tests.

After the produced electrons reached the first GEM, they were amplified in the quadruple GEM stack, which can be seen in Figure 2.3 (c). The GEMs and the transfer fields were labeled in the same way as explained in section 1.3. The GEMs used in the ageing setup were 10×10 cm^2 large test foils with double-conical holes, which were also produced with different pitches. As one can see in the picture, the GEM foils were framed to mount them together in a stack. With theses frames each GEM had a thickness of 1 mm, what makes a gap between each GEM foil of 1 mm (0.5 mm + 0.5 mm). To increase these gaps, 1 mm thick washers were installed between each GEM so that the distance between the foils was doubled[9]. To power the GEMs, each foil had

[8] 4 channel NIM programmable HV power supply N1471 from CAEN.
[9] The distance between GEM4 and anode in Figure 2.3 (c) was increased to make the picture.

an extension which functioned as high voltage connection. Little wires could be soldered onto these extensions. These wires were connected to Safe High Voltage (SHV) connectors outside of the detector, so that cables to the power supplies could be plugged there. To power the GEM stack, four programmable HV power supplies[10] with two channels each were used.

After multiplication, the incoming electrons reached the anode, where the current as well as the pulse-height-spectrum was measured and analyzed as explained in the next subsection.

During the two years of operation, several components of the equipment was exchanged due to shared usage with colleagues or because something broke. Because of this, two different field cages were used, one with 10 cm drift as explained above and another one with only 8 cm drift. Also a different anode was used, which had no pads, but x- and y-wires instead. That is the reason why the term "anode current" will be used instead of the ALICE internal nomenclature "pad plane current". The GEMs themselves were also replaced from time to time because they were broken, aged, sparked or a microscopic analysis was carried out, which destroyed them. As a consequence it was not always possible to operate the detector with S-LP-LP-S stacks.

2.1.3 The readout system

Due to the change of equipment, also the readout scheme changed quite often. In addition, several electronic filters, implemented in the HV supply lines, were tested to reduce the noise in the system. Therefore the readout will be explained exemplary based on the readout of the GEM4 Bottom electrode.

In Figure 2.4 (a) one can see a block diagram of the readout scheme. Close to the detector a so called "decoupling box" was installed, to extract the signal of the electrode. A sketch of this box is shown in Figure 2.4 (b). The signal coming from GEM4 Bottom was decoupled by the capacitor in the box with $C = 1\,\mathrm{nF}$.

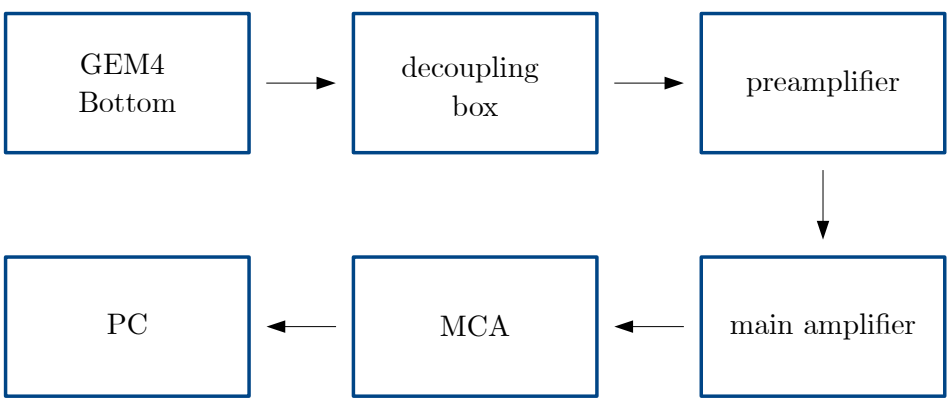

(a) Block diagram of the electronic readout.

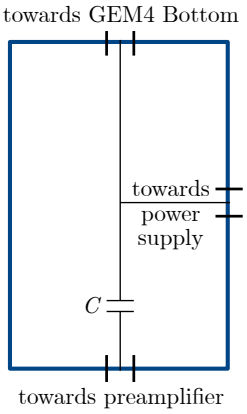

(b) Decoupling box.

Figure 2.4: Overview of the readout scheme.

Close to the decoupling box, the preamplifier[11] was placed. The short distance between detector and preamplifier was chosen to minimize the decrease of the signal-to-noise ratio, caused by the capacitances of the cables. Afterwards the signal was driven outside the copper box towards

[10] 2 channel NIM programmable HV power supply N1471A from CAEN.
[11] Preamplifier 142PC from Ortec.

the main amplifier[12], installed in a NIM crate. After the signal was amplified and shaped, it was digitized by the Analog-to-Digital Converter (ADC) in the Multichannel Analyzer[13] (MCA). Finally it was sent to the PC, where the spectrum could be displayed, analyzed and saved.

2.1.4 Calibration of the ADC using argon measurements

To calibrate the ADC, the measured spectrum in Ar-based gas mixtures could be used. A typical spectrum taken in Ar-CO_2 (70-30) is shown in Figure 2.5 (a). One can see that two peaks are visible, the photo (or main) peak at 5.89 keV and the so called escape peak at 2.69 keV.

If a X-ray emitted by the ^{55}Fe source undergoes photoelectric absorption in the outermost shell of an argon atom, it produces a single e^--Ar^+ pair. The kinetic energy of the produced photoelectron is equal to the energy of the X-ray minus the binding energy. With this energy, the electron is able to produce more electrons along its path through the detector. These primary electrons get amplified and the produced electron cloud gives one entry in the pulse-height spectrum shown in Figure 2.5 (a). In this process all the energy of the initial X-ray is deposited in the detector and produces the photo peak.

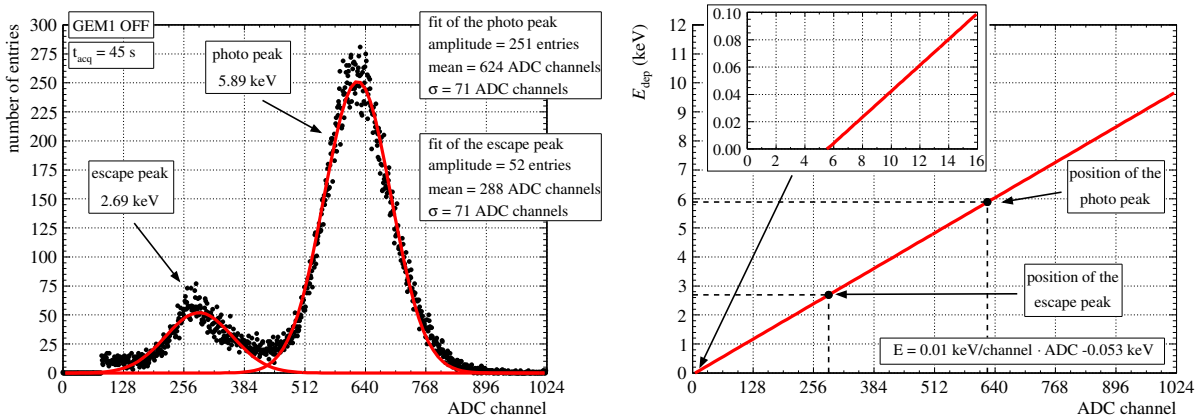

(a) Measured and fitted pulse-height spectrum, obtained in Ar-CO_2 (70-30).

(b) Correlation between deposited energy E_{dep} and ADC channel.

Figure 2.5: Energy calibration of the ADC using a pulse-height spectrum obtained in Ar-CO_2 (70-30).

A different process takes place, if the initial X-ray undergoes photoelectric absorption in the K shell of an argon atom. Since the excitation potential of the K shell of argon is 3.2 keV and therefore lower than the energy of the X-ray, it is possible for the X-ray to knock out an electron of the innermost shell. The emitted photoelectron of the K shell takes a kinetic energy of 5.89 keV - 3.2 keV = 2.69 keV, which is deposited in the detector. The vacancy of the innermost shell is filled by an electron from an outer shell and a new X-ray is produced. If this new X-ray escapes the sensitive volume of the detector, a part (3.2 keV) of the *initial* X-ray energy is missing. Therefore the escape peak at 2.69 keV is produced in the spectrum. [23, p. 169 ff.]

Since the energies of both peaks are known, one can do a correlation between the deposited energy in the detector E_{dep} and the ADC channel, which is shown in Figure 2.5 (b). In the

[12] Spectroscopy Amplifier 672 from Ortec.
[13] Multichannel Analyzer MCA8000D from Amptek.

example one can see that the fit hits the x-axis at channel 6, which means that the measured peak position has to be shifted by 6 channels to the left. In this way one can be sure, that channel 0 really corresponds to zero energy.

Since all the pulse-height spectra were saved, this calibration procedure could be applied to all measured pulse-height spectra taken in an Ar-based gas mixture. For the short Ne-CO_2-N_2 measurement, the same correction was used, as in the measurement in Ar-CO_2 before. Since the same electronic readout was used, one can assume, that the calibration factor did not change.

2.1.5 The LabVIEW software

To control and monitor the experiment as well as to analyze and save the measured data, several programs were set up with LabVIEW 2013 on the PC. A LabVIEW program to control the five power supplies via the RS-232 protocol[14] was already set up by C. Garabatos and could be taken over. It could be used to put easily different GEM voltages as well as transfer fields and to find a good working point for the different GEM stacks and gas mixtures. It also monitored the maximum currents for each channel of the power supplies and had an automatic ramp down implemented to turn off the complete detector in case of an exceeded current limit. Also parameters like ramp speed, maximum GEM voltages (400 V) and a plot with the currents of the channels were implemented. In this way it was a powerful tool also to debug the detector and to identify a broken GEM.

The main program to control the ageing setup had to be programmed first. This major program had to define the cycle of a measurement as it can be seen in Figure 2.6. With this program the individual measurements of the different equipment took place in the right order.

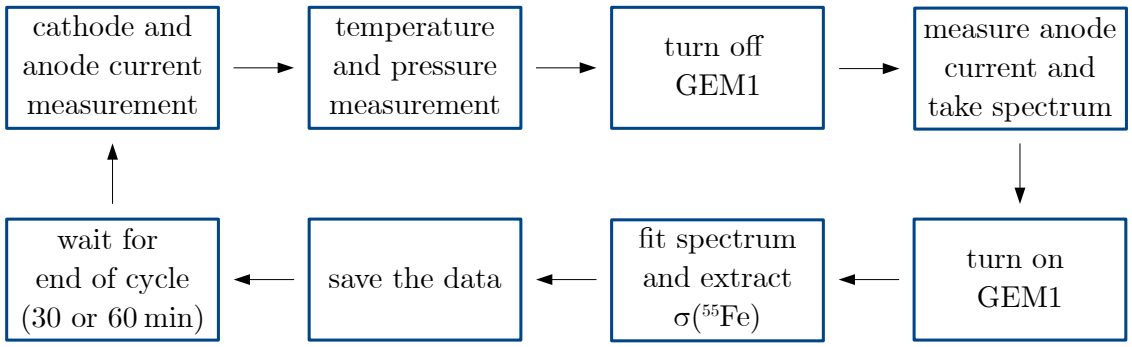

Figure 2.6: Flowchart of the LabVIEW program.

The order of the measurements can be seen in the block diagram. At the beginning all plots were cleared and all variables were set, like the time of the cycle or acquisition time t_{acq} of the spectrum. Afterwards the anode and cathode current were measured with all four GEMs on. Both for the anode measurement with pads and with wires all readout channels were connected so that the complete current on the electrode was measured. Shortly afterwards the ambient temperature, the ambient pressure and the relative humidity were measured. Now the first GEM was turned off to disable the amplification from the drift region and to reduce the rate. Immediately after ramping GEM1, the anode current was measured once more as well as the

[14] The Recommended Standard 232 (RS-232) is a serial communication standard used to interface external equipment with computers.

pulse height spectrum was taken. After the measurement, GEM1 was turned on again. Since the turning off and on of GEM1 changed the amount of accumulated charge on the anode, a correction had to be applied. This will be explained in subsection 2.1.7. When GEM1 was turned on again, the analysis of the spectrum took place. A Gaussian fit was used with the parameters measured from the last cycle. Since changes in the peak position and width of the peak were not suspected to occur quickly within half an hour, the parameters of the last cycle had been a good first guess for the fit function. After the analysis of the spectrum, the data was saved in a text file. Also every spectrum was saved in a separate text file so it could be re-analyzed afterwards. In the last step, the program just waited until the time of the cycle ended and the next measurement cycle could be started.

Screenshots of the LabVIEW program which controlled the measurement can be seen in Figure 2.7 (a) and (b). In Figure (a) the analysis of the pulse height spectrum is shown. In the upper right plot an example of a measured spectrum in Ar-CO_2 is shown. By plotting the spectrum in the program it was possible to identify possible problems like a high noise level. In the lower right plot, the fit of the main peak is shown. The fit was only drawn within the boundaries which were used to apply the fit. A cut at the left side was implemented to avoid fitting the noise or the escape peak in the case of an argon based gas mixture. On the other side of the peak, no fit boundaries were necessary.

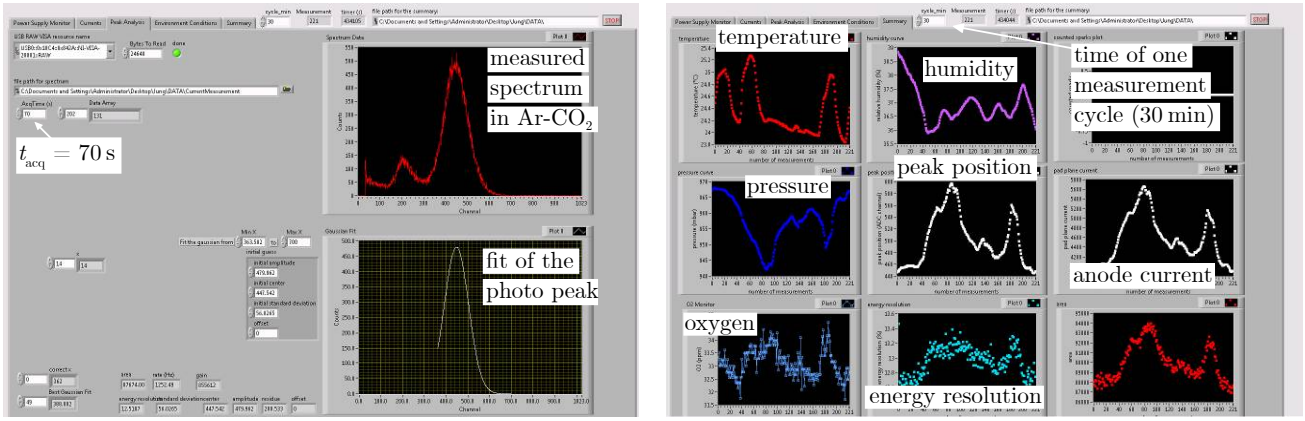

(a) Analysis of the measured pulse-height spectrum.

(b) Overview of the measured quantaties.

Figure 2.7: Screenshots of the LabVIEW program.

In here also the acquisition time could be tuned and results of the fit like standard deviation, peak position or calculated quantities like energy resolution or rate of the source could be monitored here. In Figure 2.7 (b) the overview of the measured quantities can be seen in several plots. One can easily see for example that peak position and anode current do strongly correlate. With these plots it was possible to identify an empty gas bottle and replace it before the measurement had to be stopped.

2.1.6 Determination of the gas gain

With the spectrum, the rate R of the source could be extracted by dividing the area beneath the photo peak[15] with the acquisition time t_{acq}. The rate gives the amount of X-rays absorbed

[15] In Ar-CO_2 and Ar-CH_4 also the area beneath the escape peak had to be taken into account.

in the drift volume per second. Together with the number of primary electrons N_e ejected by one X-ray and the elementary charge e, the primary current could be calculated. This current gives the amount of charge entering GEM1 per second. Together with the current on the anode, the gain could be calculated by dividing the anode current by the primary current.

$$G = \frac{I}{N_e \cdot e \cdot R} \tag{2.1}$$

Since the number of primary electrons depends on the ionization potential of the elements in the gas, this value had to be calculated for the different gas compositions, which can be seen in Appendix A. A list of N_e for the three gases used in the ageing tests is shown in Table 2.1.

Gas mixture	Ratio	N_e
Ar-CO_2	70-30	209
Ar-CH_4	95-5	225
Ne-CO_2-N_2	90-10-5	164

Table 2.1: Number of primary electrons N_e ejected per 5.89 keV X-ray.

Since the rate with GEM1 ON was much too high to acquire a spectrum, the gain of the quadruple stack had to be measured at a lower rate. Therefore the source was misaligned with the opening in the field cage, resulting in a reduction of the rate. Together with the current measured on the anode, the gain of the quadruple GEM stack was calculated. This procedure was repeated before each measurement was started.

2.1.7 Converting current into charge per area

To convert the measured current on the anode into accumulated charge, the current was integrated over time. Since one gets a single current value within a cycle, the calculated charge had to be corrected by the time with GEM1 OFF. This could be estimated using the ramping time of GEM1, the time to acquire a spectrum and the 30 s pause. This pause after turning GEM1 OFF was implemented precautionary, in order to give time for electromagnetic oscillations induced in the GEMs to get reduced. All together one can say that a 3 min correction had to be applied, including an acquisition time of 60 s. This gives a correction factor of 10 % (5 %) for a 30 min (60 min) cycle. Since the current with GEM1 OFF dropped from several hundred nA to a few hundred pA, the current accumulated within the 3 min GEM1 OFF was neglected.

After the correction was performed, the calculated charge was divided by the area, irradiated by the ^{55}Fe source. Since the area depends on the mean free path λ of the X-rays in the gas, it is different for the three gas mixtures. The areas are listed in Table 2.2.

Gas mixture	Mixing ratio	Area (cm^2)
Ar-CO_2	70-30	5.73 ± 0.11
Ar-CH_4	95-5	3.46 ± 0.07
Ne-CO_2-N_2	90-10-5	15.90 ± 0.32

Table 2.2: Irradiated areas for the different gas mixtures.

To calculate the irradiated area, the profile of the ^{55}Fe source was measured with a separate detector. Together with the different mean free paths, a Gaussian for every millimeter of the drift volume could be calculated and summed. This produced one final Gaussian for every gas mixture. The Full Width at Half Maximum (FWHM) was used as an estimation of the diameter of the irradiated area. A detailed description of the measurement and calculation is given in Appendix B.

2.1.8 Normalization procedure

To distinguish between alterations of the detector performance due to environmental variations and ageing effects, one had to normalize the measured gain to the same environment conditions. Since the amplification in gaseous detectors is inversely proportional to the density of the gas, changes of the ambient temperature and pressure conditions do have a strong impact on the gas gain. [24, p. 136]

Therefore the ambient temperature T and pressure p were continuously measured by the sensor[16], taped to the outside wall of the field cage. Their errors were estimated by the variances of the single measurements to $\Delta T = \pm 0.01\,^{\circ}\mathrm{C}$ and $\Delta p = \pm 0.4\,\mathrm{mbar}$. If one plots the ratio of temperature to pressure, one can easily compare it to the measured gain G due to the proportionality shown in Equation 2.2.

$$G \sim \frac{1}{\rho} = \frac{V}{m} = \frac{n \cdot R}{m} \cdot \frac{T}{p} \tag{2.2}$$

In Figure 2.8 (a), T/p is plotted in K/mbar as a function of the accumulated charge per area. The error of the ratio was calculated by error propagation to 0.5 ‰, which makes about $\pm\, 0.016 \cdot 10^{-2}\,\mathrm{K/mbar}$. Since a lot of data points are plotted in the figure, the individual error bars would overlap each other. Therefore a single data point was placed in the upper right corner and drawn with error bars. It can be used to assess the size of the error.

One can compare the plot of T/p to Figure 2.8 (b), where the calibrated peak position as a function of charge per area is shown. Already with the naked eye, one can see that these two quantities do strongly correlate. To quantify the correlation, the peak position is plotted versus temperature over pressure in Figure 2.8 (c). With a linear fit, the slope as well as the intercept were determined. A normalization to the arithmetic mean of T/p using Equation 2.3 is now possible:

$$P_{\mathrm{corr}} = P_{\mathrm{cal}} - \left[m \cdot \left(\frac{T}{p} - \left\langle \frac{T}{p} \right\rangle \right) \right] \tag{2.3}$$

The difference between every T/p value to the average value $\langle T/p \rangle$ was converted via the slope m of the fit into number of ADC channels. Every correction was then subtracted from its corresponding value of the calibrated peak position P_{cal}. The errors were calculated with error propagation from the errors of the input parameters. Through the correction formula, the error of the peak position increased from $\pm\, 3$ ADC channels ($\pm\, 0.5\,\%$) to $\pm\, 4$ ADC channels ($\pm\, 0.7\,\%$).

The peak position corrected to the T/p variations is shown in Figure 2.8 (d). By comparing it to the calibrated peak position in Figure 2.8 (b), one can see that almost all gain fluctuations were caused by temperature and/or pressure variations. An exception is the beginning of the

[16] Modular Signal Recorder 145 (MSR 145), universal data logger with temperature, humidity and pressure sensor from MSR Electronics GmbH.

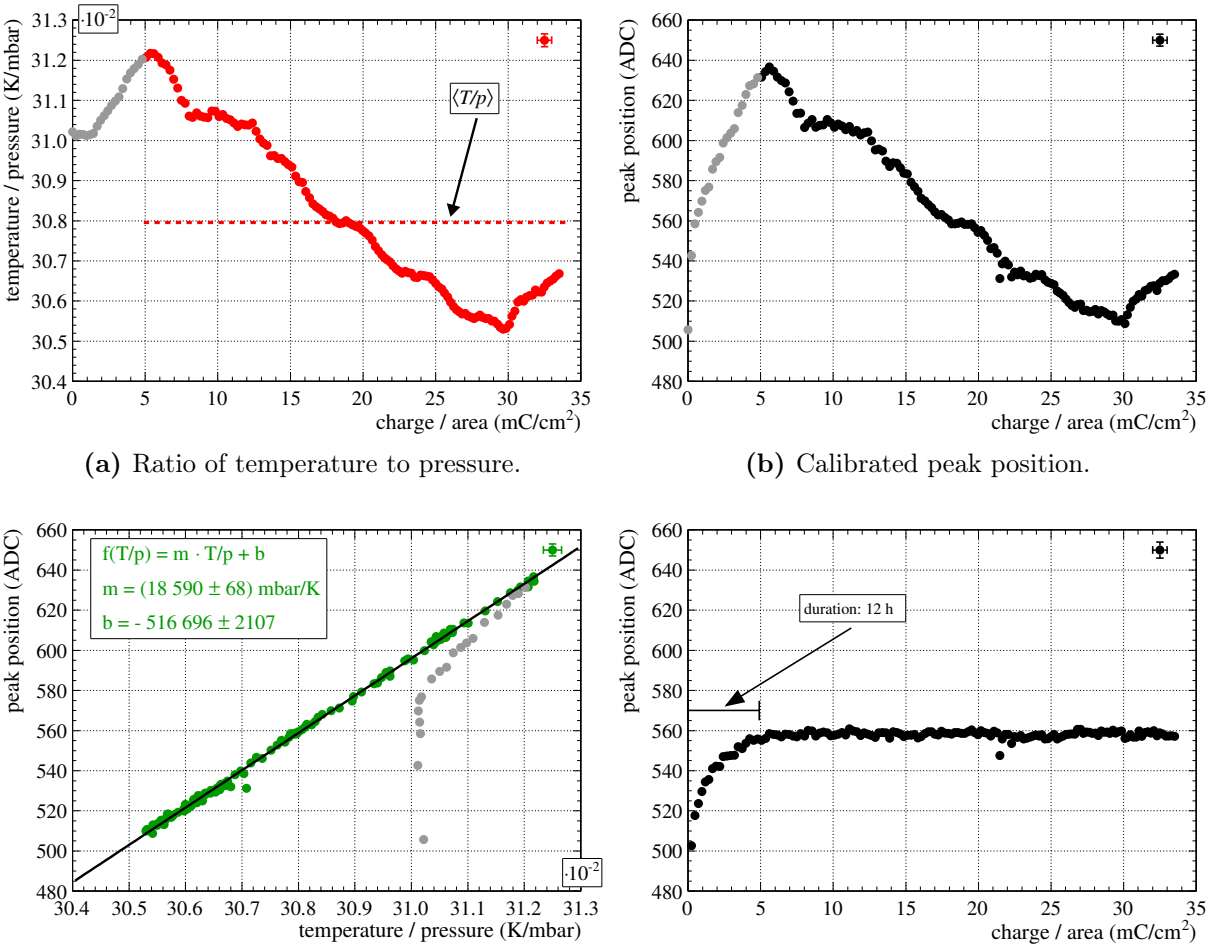

(a) Ratio of temperature to pressure.

(b) Calibrated peak position.

(c) Correlation between peak position and T/p. Grey data points were not used for the fit.

(d) Peak position corrected for T/p variations.

Figure 2.8: Example of the normalization procedure. The grey data points correspond to the charging-up effect and were excluded for the fit.

measurement. Within the first $5\,\mathrm{mC/cm^2}$, an increase of the gain is visible, followed by a saturation. As indicated in the figure, the peak position was stable after 12 hours. A possible explanation is the so called charging-up effect. This effect refers to a slow increase of the gain, due to charging-up of the insulating surfaces of the GEM at the beginning of the operation. However, experiences from quadruple GEM stacks tell, that such a long time for charging-up is rather unusual. Since this behavior was seen in many measurements of the ageing tests, it seems, that turning GEM1 ON and OFF and/or the high gains did somehow extend the charging-up process. Since the proportionality between gain and T/p is not true for this part of the measurement, is was excluded from the fit, as indicated in Figure 2.8 (c) by the gray data points.

The normalization procedure described above was performed for the gain of the triple as well as the quadruple GEM stack. For the gain of the complete stack, the anode current was used. Through the normalization, the error of the current increased from $\pm 1.0\,\%$ to about $\pm 1.1\,\%$.

2.2 Tested components

Gaseous detectors are always affected by contaminations in the gas used. Apart from impurities in gas bottles or not entirely gastight constructions, the contaminations can come from outgassing of construction materials. For that reason the components used should be tested concerning their impact on the detector performance due to outgassing. [24, p. 420]

Therefore components, which are used for the assembly process of the upgraded TPC and afterwards remain in the gas volume even during the operation of the detector, were put in the outgassing box. If no impact on the detector performance was monitored, the components in the gas stream could be considered as valid for use in the TPC.

An overview of the four components tested including their purposes is given in Table 2.3. A short statement about the utilization of the respective components, as well as the preparation of the tested samples will now be given.

Component	Material	Purpose of the components
Screws	Polyamide PA 6.6	Screws to mount the GEM frames together
Frames	Vetronite	Frames of the GEMs
Epoxy	Araldite 2011	Epoxy adhesive to glue the GEMs into their frames
Resistors	SMDs	Protection resistors for the GEM segments

Table 2.3: Tested components, materials and their purpose.

At the beginning a sample of screws[17] was tested in the outgassing box. These screws are made of polyamide, a special plastic, and will be used to mount the frames of the GEMs together to a stack. The sample used in the ageing test contained roughly 70 screws and can be seen in Figure 2.9 (a). The screws were cleaned with ethanol before putting them into the box.

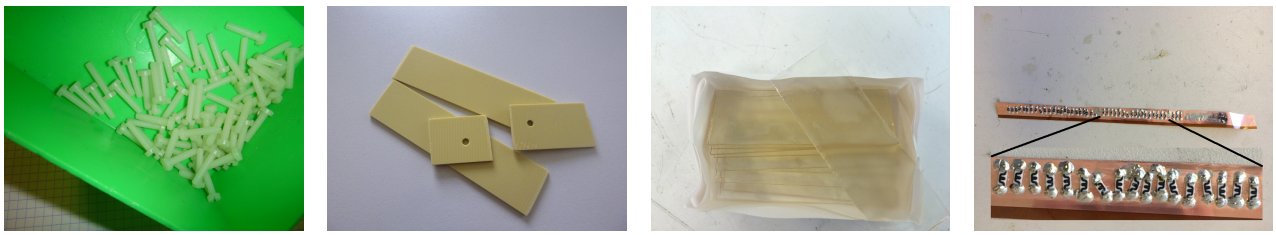

(a) Sample of screws. **(b)** Sample of frames. **(c)** Sample of epoxy. **(d)** Sample of resistors.

Figure 2.9: Pictures of the samples of the tested components.

Next the GEM frames were tested, which are made of an insulating fiberglass-epoxy compound called Vetronite[18]. In the upgraded TPC, this material will also be used for spacers between the GEMs to compensate the electrostatic attraction of the large TPC foils. Also an additional frame above the GEM1 Top electrode of the TPC will be installed. With its metallized surface it will serve as cover electrode, helping to adjust and homogenize the electric field

[17] "Slotted cheese head machine screws" (M4 × 18) made by "Bossard Deutschland GmbH" (BN 1061).

[18] Insulating laminate made of glass fabric bonded with epoxy resin made by "Von Roll Deutschland GmbH" (Vetronit EGS 103).

in the drift region. The tested sample of the frames can be seen in Figure 2.9 (b). The pieces were also cleaned with ethanol before starting the measurements.

The third component tested was the epoxy adhesive[19], which was used to glue the GEMs onto their frames. To test the epoxy adhesive itself, 10 pieces of glass ($76 \times 26\,\mathrm{mm}^2$) were painted on both sides with the epoxy, as one can see in Figure 2.9 (c).

The last components tested were resistors, which will be soldered on one side of every GEM foil of the TPC. This will make sure that voltage drops due to possible discharges will only occur on the foil side with resistor, whereas the other electrode remains at its nominal potential. Furthermore it will prevent the discharge to propagate to another GEM or to the anode and the electronics connected. [25, p. 224]

The sample of tested resistors is shown in Figure 2.9 (d). These resistors are Surface Mount Devices (SMDs). For the ageing setup, 22 resistors[20] were soldered on a left-over GEM. According to C. Garabatos, the resistors were soldered with the so called "no-clean" solder, which is a special alloy which needs *no* cleaning after soldering. Contrary to this, normal solder leaves traces that under HV could produce corrosion, which might destroy the contacts. The sample was for one run cleaned with acetone, for another measurement the SMDs were painted with polyurethane (PU). Therefore the ageing measurements of the resistors contained a test of the SMDs, the solder, acetone and PU.

2.3 Long-term measurements in Ar-CO_2 (70-30)

The first long-term measurements were performed with Ar-CO_2 (70-30). With this gas, all the materials were tested concerning their outgassing behavior.

2.3.1 Measurement testing the empty outgassing box, screws and frames

The first measurement in Ar-CO_2 was performed with a S-LP-LP-MP GEM stack, which was already in use before[21]. The system was tuned to a gas gain of the complete stack of about 31 000 in order to accelerate possible ageing effects. With a duration of the measurement of 64 days, the overall accumulated charge was in the end about $470\,\mathrm{mC/cm}^2$. With GEM1 off, an average rate of about 1230 Hz and a gain of 16 500 was measured. During the measurement the water content was monitored and stayed constant around 510 ppm during the complete measurement[22]. The only exception occurred shortly before the gas bottle was empty. The water content increased to about 1000 ppm and needed some days to get reduced. The measurement was stopped several times for various reasons, such as an empty gas bottle, an announced power cut in the laboratory, an upgrade of the operating system of the PC forced by the IT-department and a measurement of the activity of the radioactive source performed by the radiation protection crew. Afterwards the data of the different parts were merged together.

An overview of the measurements can be seen in Figure 2.10. The measurements are normalized to the same average value of T/p, even though they consist of five individual runs with sometimes several days delay between each other.

[19] Multi-purpose epoxy adhesive made by "Huntsman Corporation" (Araldite 2011-A/B).
[20] $10 \times 1\,\mathrm{M\Omega}$ and $22 \times 5\,\mathrm{M\Omega}$ made by "SRT Resistor Technology GmbH".
[21] The GEMs already saw an unknown amount of charge.
[22] The 17.5 m long pipe from the gas bottle to the flowmeter was at the beginning made of plastic and after this measurement replaced by stainless steel as described in subsection 2.1.1.

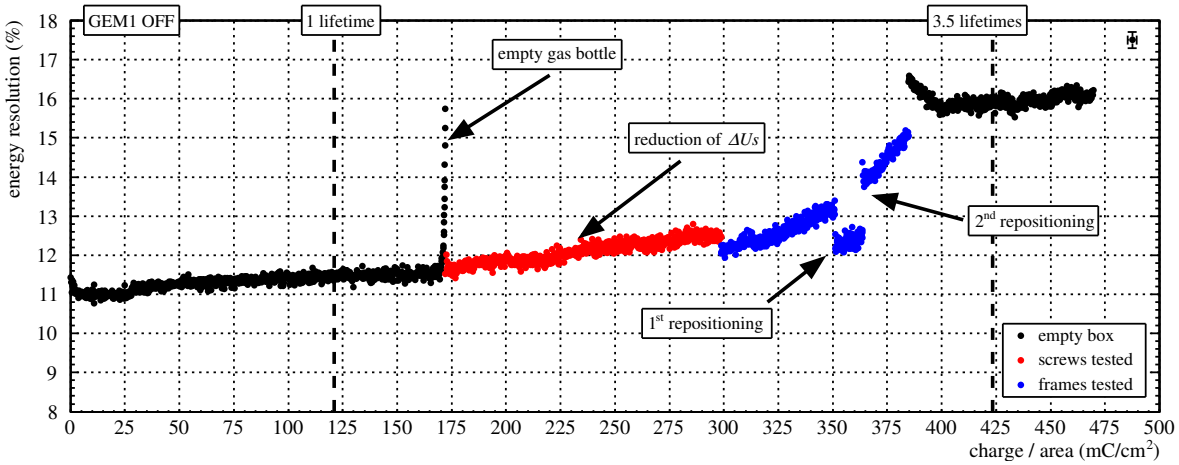

(a) Energy resolution extracted from the calibrated pulse-height spectra.

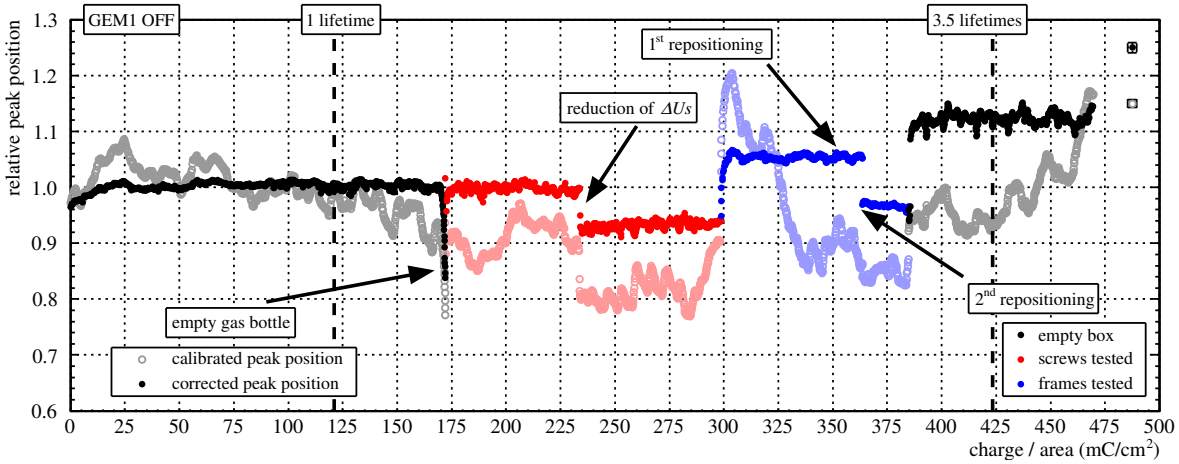

(b) Calibrated and corrected peak position.

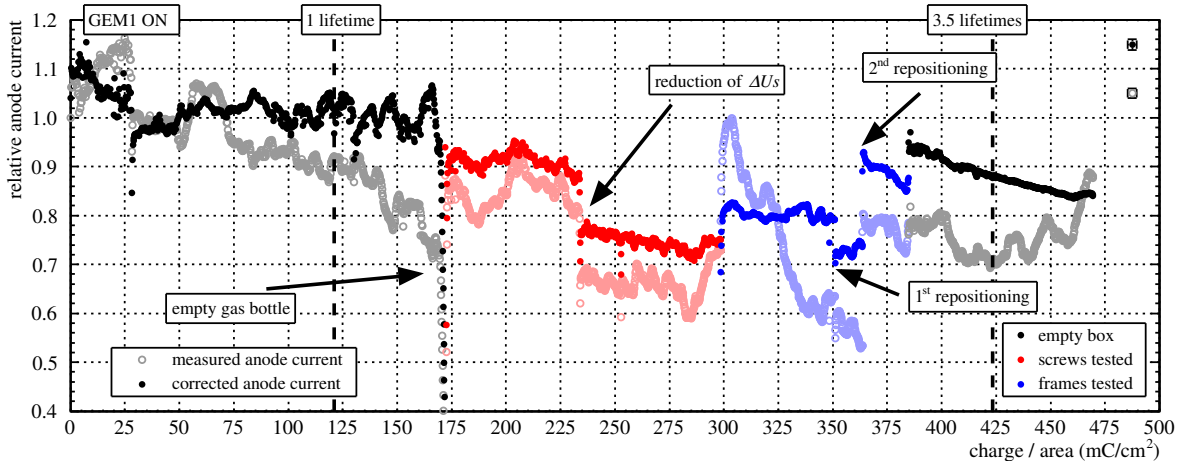

(c) Measured and corrected anode current.

Figure 2.10: Results of the first measurement using an empty outgassing box as well as testing the screws and frames, performed in Ar-CO_2 (70-30).

For the relative peak position in Figure 2.10 (b), the calibrated and corrected data is plotted. For the relative anode current in Figure 2.10 (c), the measured (raw) as well as the corrected current is plotted.

At the beginning of the measurement the GEM stack itself was tested with no additional material in the outgassing box (black points). After that, the screws were tested (red points) and than the frames of the GEMs (blue points). In the end a second run with an empty outgassing box was performed to compare it with the beginning of the measurement. In the plots of the peak position, anode current and energy resolution, two different amounts of charge per area were marked with a line. The first line indicates the projected lifetime of the upgraded TPC of 10 years of operation, the second line indicates 3.5 times the projected lifetime. For both values, a pulse-height spectrum of the ^{55}Fe source is shown in Figure 2.11 (a) and (b).

If one focuses first on the behavior of the gain and the energy resolution within the projected lifetime of the TPC, one can say, that there are no serious changes monitored. The peak position and therefore the gain stays stable within the complete lifetime. Even though the energy resolution, shown in Figure 2.10 (a) shows a small slope, the degradation up to 121 mC/cm^2 is negligible. The pulse-height spectrum in Figure 2.11 (a) shows a symmetrical photo peak with no expanded flank as well as a clear separation between escape and photo peak. With GEM1 ON the anode current shows a rather fluctuating behavior, but also here no systematic degradation is monitored.

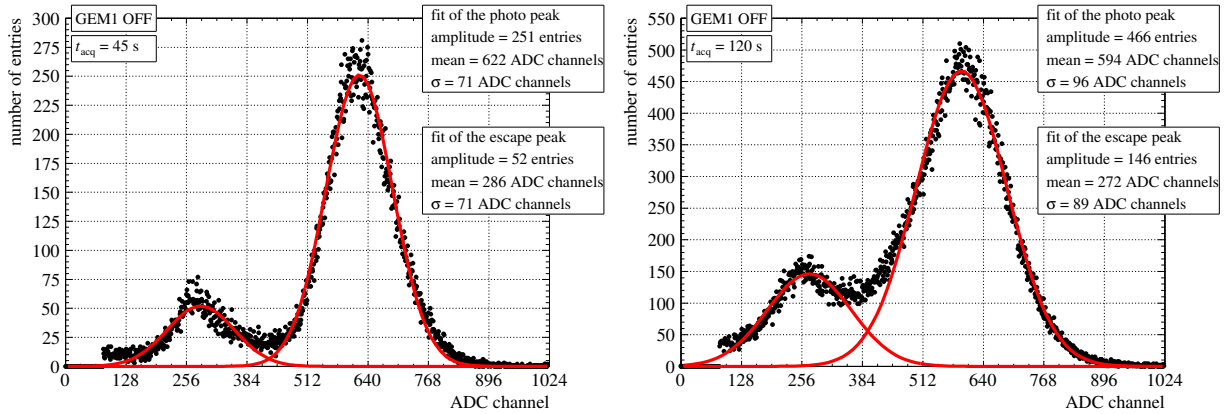

(a) Pulse-height spectrum obtained at 121 mC/cm^2 (1 lifetime).

(b) Pulse-height spectrum obtained at 423.5 mC/cm^2 (3.5 lifetimes).

Figure 2.11: Two calibrated and fitted pulse-height spectra of the first measurement using an empty outgassing box as well as testing the screws and frames, performed in Ar-CO_2 (70-30).

Also during the second measurement with the plastic screws in the box, no change in the behavior of the peak position or energy resolution was monitored. Although the energy resolution deteriorated to about 12.5 %, the slope of the resolution seems not to change. The peak position stays for the first part constant at its nominal value. In the second part of the run, the GEM voltages were decreased a little bit (reduction of ΔUs), which resulted in a jump of the peak position, as well as in the anode current. Leaving aside this jump of the peak position, one can say that no effect was monitored, which could be attributed to the presence of the screws in the box.

In the third measurement the frames were tested. Also during this measurement the peak position shows no continuous change, whereas the energy resolution continuous get worse. In addition to the increase one can see two abrupt changes in the energy resolution, which will be explained now. During this measurement the activity of the radioactive source was measured. After the measurement, the source was put back on top of the detector (1^{st} repositioning). After some iterations it was found, that the energy resolution was better than before. Also a jump in the anode current was monitored. It was found, that the exact position of the source had an effect on the pulse-height spectrum and therefore on the energy resolution. This phenomenon was not understood, since the position of the source should have absolutely no effect on the resolution of the detector. Only a microscopic analysis of the GEMs performed after the measurement was finished could provide an explanation, which is given later. The measurement was stopped and the source was put at the center of the window of the detector (2^{nd} repositioning), as it was before.

At the end, a second measurement with an empty outgassing box was performed. In here one can see that the energy resolution also continues to increase, but with a smaller slope than in the run with the frames. The peak position stays constant, although the jump to a higher gain already at the beginning of the measurement is not understood. Conspicuous is that the anode current decreases monotonously. The second pulse-height spectrum shown in Figure 2.11 (b) was taken during this last run. In here one can see that no clear separation between escape and photo peak is achieved anymore. The width of the main peak increased dramatically compared to the pulse-height spectrum to the left. Important to mention is that the widening of the main peak is symmetrical. This means that the fluctuation in the amplification process increased both to lower and to higher gains.

Due to the surprising results like the dramatic loss of energy resolution and a discoloration on GEM4 Top, a microscopic analysis of the last two GEMs of the stack was performed.

SEM analysis with SEs

GEM3 and GEM4 were analyzed under a Scanning Electron Microscope (SEM) by A. T. Pérez Fontenla of the Engineering Department of CERN. A report about this analysis, including *some* of the produced images, is provided in [10]. Since the analysis included far more images than reported in [10], some of the material presented in this work will be referred directly to A. T. Pérez Fontenla.

A SEM is an instrument which can create magnified images of a probe using an electron beam. This beam hits the probe, which is put under vacuum and penetrates the sample several hundred nanometers deep depending on the beam energy and the material properties. On the way through the material, the electron beam will eject weakly bound valence electrons or conduction band electrons through inelastic scattering. These ejected electrons are called secondary electrons (SEs) and are generated all along the trajectory of the initial electron beam. Due to their low kinetic energy, only SEs at or close to the surface of the sample can escape the probe and can be detected. That's why images made with SEs can only provide a topographic view of the sample. [26, p. 30]

A picture of GEM4 Top after the measurement can be seen in Figure 2.12 (a). On this foil two different areas were marked and later analyzed with the SEM: the reference area close to the frame of the GEM and the irradiated area in the center of the GEM. For the reference area it is assumed, that there was no amplification, since it is quite far away from the center of the foil. Contrary to this it is assumed that the center of the GEM saw the complete charge generated by the stack, because it is the last GEM in the stack.

Already with the naked eye one can see that the irradiated area has a colored (brownish, golden) dot. A magnification made with a digital USB microscope is also shown in the same Figure. Around the irradiated area a ring of discoloration is visible. Both effects are *not* relics of the camera such as reflections or bad brightness conditions.

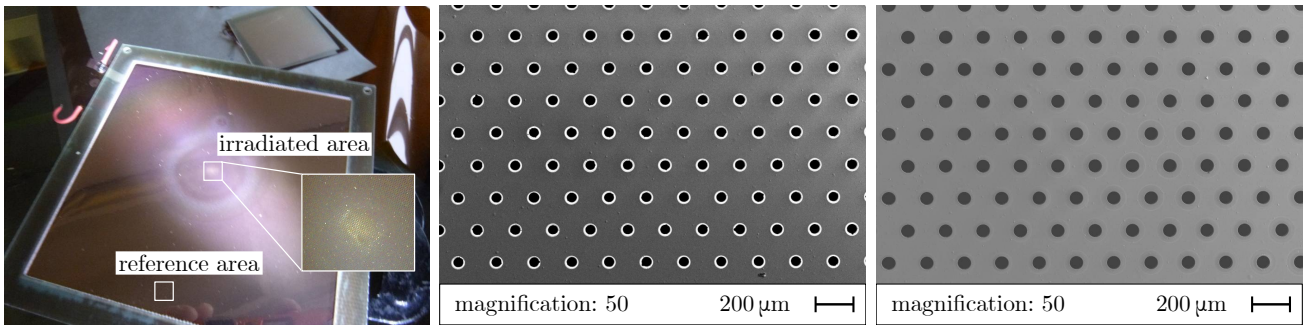

(a) Picture of GEM4 Top, including a magnification made with a digital USB microscope.

(b) Top view of the reference area, made with SEs.

(c) Top view of the irradiated area, made with SEs.

Figure 2.12: Top views of GEM4 Top, made with a camera and SEM. SEM images provided by A. T. Pérez Fontenla.

In Figure 2.12 (b) and (c) images made with SEs from the SEM are shown, which both have the same magnification factor. The image in Figure 2.12 (b) shows the reference area. One can clearly see the copper electrode, as well as the kapton ring in every hole, which protrudes between the top and bottom electrode. In Figure 2.12 (c) one can see the image of the irradiated area. In here one can see that the kapton layer between the two electrodes is no longer visible. The image also shows, that the removal of the kapton in the GEM hole is not an effect of a few holes, but valid for all holes of the irradiated area. This effect is also visible in the irradiated area of GEM3 as one can see in the appendix in section C.1.

To study this effect even better, more images were made with even larger magnification factors. In Figure 2.13 (a) - (f) one can see a comparison between holes of the reference area in the first row and of the irradiated area in the second row. In Figure 2.13 (a) and (d) one can see a top view of a reference hole and an irradiated hole, which were superimposed with colored rings. The diameters of these rings were defined using the scale of the images shown in the lower right corner. One can see that the diameters of the reference hole are close to the specifications of the GEM. By comparing Figure 2.13 (a) and (d) one can now see that the diameter of the copper electrode did not change. Only the diameter of the kapton layer between the electrodes was affected by the ageing test.

In Figure 2.13 (b) and (e) one can also see a single hole of the reference and irradiated area, but with the GEM tilted by 45°. From this perspective one can see now, that not only the part of the kapton which sticks out into the hole was removed, but also kapton which is located between the electrodes.

In addition one see some lines close to the edge of the top electrode in the image of the irradiated hole. The magnification in Figure 2.13 (f) shows that the lines are in fact cracks in the electrode, which do not only extend over the upper surface of the electrode, but also over the side surface in the GEM hole. By comparing this image with Figure 2.13 (c) one can see that this effect was produced by the operation of the GEM and is not a side effect from the production.

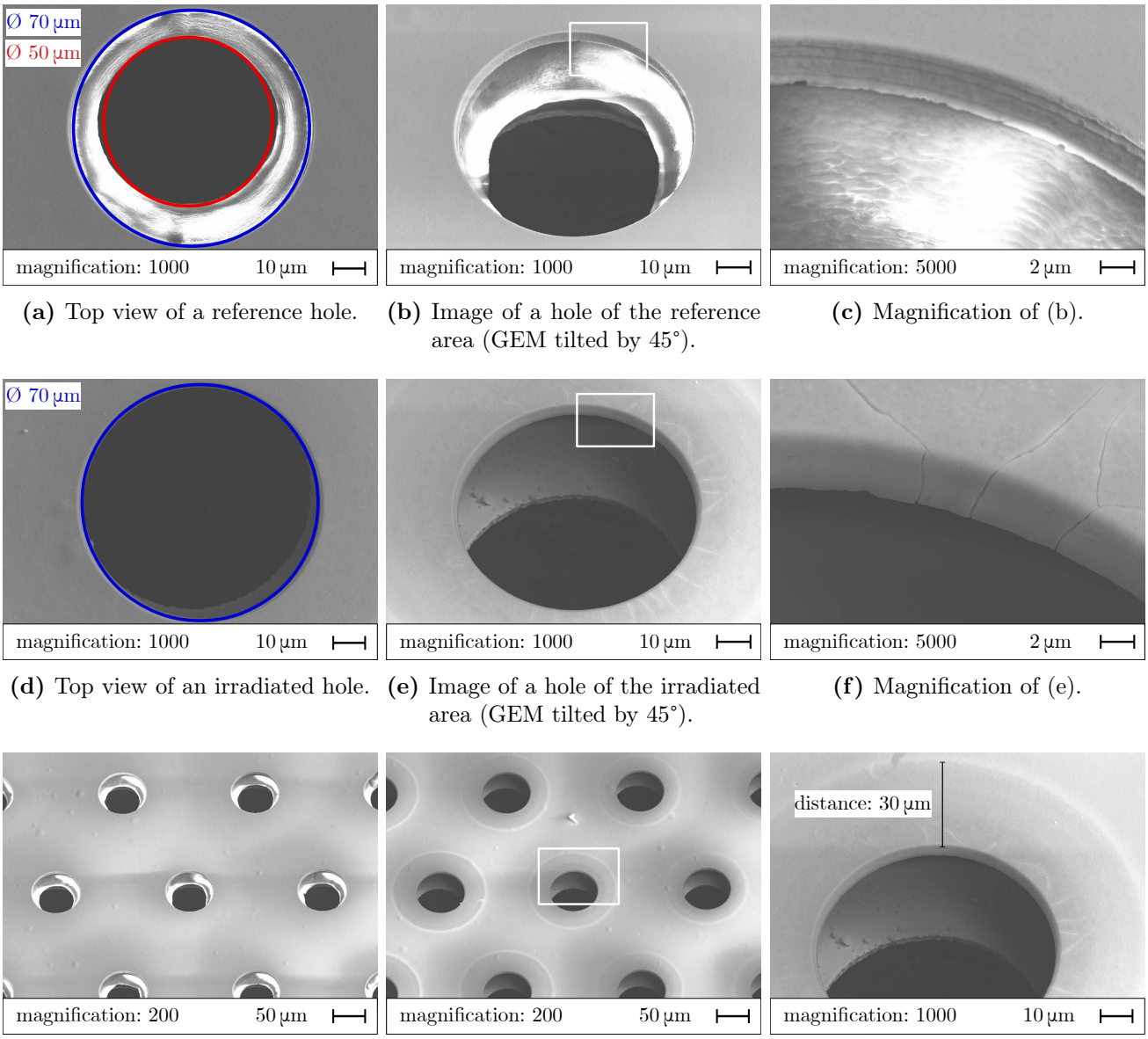

(a) Top view of a reference hole. **(b)** Image of a hole of the reference area (GEM tilted by 45°). **(c)** Magnification of (b).

(d) Top view of an irradiated hole. **(e)** Image of a hole of the irradiated area (GEM tilted by 45°). **(f)** Magnification of (e).

(g) Image of some reference holes (GEM tilted by 45°). **(h)** Image of some irradiated holes with rings (GEM tilted by 45°). **(i)** Magnification of (h).

Figure 2.13: Images of GEM4 Top made with SEs, showing the change of the hole geometry. SEM images (a) - (f) adapted from [10, p. 7 f.]. SEM images (g) - (i) provided by A. T. Pérez Fontenla. Labels inserted afterwards.

In Figure 2.13 (g) - (i) one can see another observation of the irradiated holes. Every hole in the center of the GEM had a ring at approximately 30 µm distance to the edge of the copper electrode. Here the magnification in Figure 2.13 (i) shows that the rings are not scratches in the electrode. Since images made with SEs produce a topographic view of the sample, one can assume that the rings are maybe thin depositions.

Additional measurement

The measurement was repeated with similar settings to figure out if the removal of the kapton layer can be reproduced and if the worsening of the energy resolution is triggered by outgassing effects of the GEM frames. Therefore a S-LP-LP-S stack with four new GEMs was installed and operated at a gain of about 40 000 and a duration of 79 days which resulted in an accumulated charge of about 780 mC/cm^2. The complete analysis, like the measured and corrected results can be seen in the appendix in section C.2.

Since a degradation of the energy resolution was also monitored in this measurement, GEM3 and GEM4 of this stack have also been studied under a SEM. The complete analysis of the SEM investigation can also be seen in the appendix in section C.2. Also here missing kapton in the irradiated holes was observed as one can see in the image in Figure 2.14 (d). Since the degradation of the energy resolution started close to the end of the measurement, one can assume that the deterioration was not triggered by the tested frames.

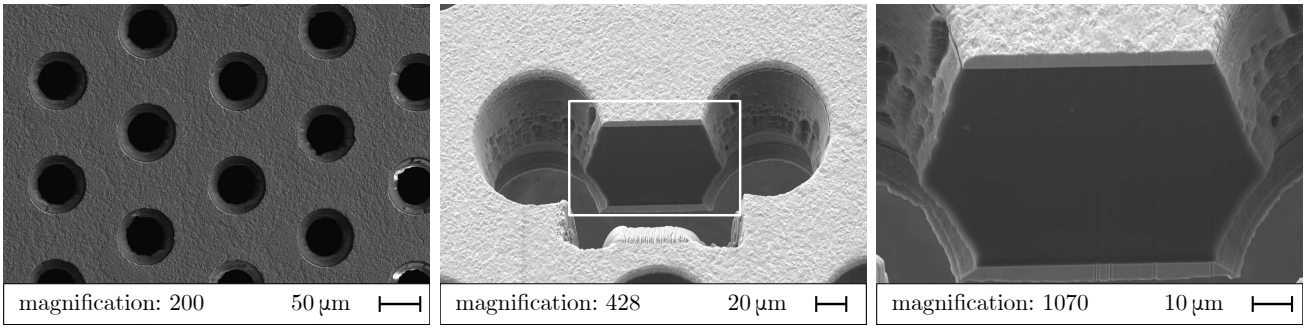

(a) Top view of the reference area. **(b)** Cross section of two holes in the reference area. **(c)** Magnification of (b).

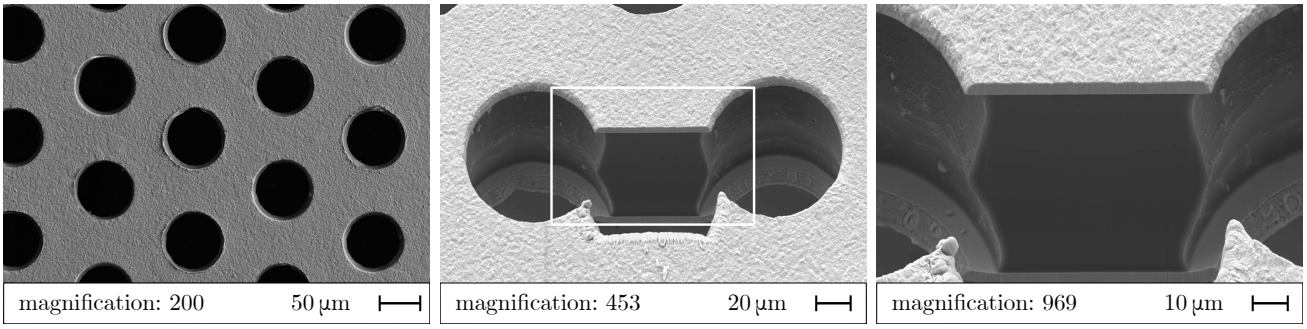

(d) Top view of the irradiated area. **(e)** Cross section of two holes in the irradiated area. **(f)** Magnification of (e).

Figure 2.14: Images showing a cross section of GEM4 of the second measurement. SEM images adapted from [10, p. 10 ff.].

In addition to the images made with SEs, a cross section of two holes of the reference and irradiated area was made using a Focused Ion Beam (FIB). This tool can be used to do sample preparation such as cross sections, but it also can be used for imaging, depending on the current density of the ion beam. With high densities, the beam cuts the material due to sputtering. At low current densities the beam can be used for fine cutting or even imaging. The ion beam produces not only secondary electrons, but also secondary ions, which both can be used for imaging. [26, p. 518 ff.]

In Figure 2.14 (b) and (c) the kapton layer of a hole in the reference area is shown. One can easily see the double-conical shape of the kapton. In the irradiated holes shown in Figure 2.14 (e) and (f), the width of the kapton layer changed. Material was removed equally over the complete height of the layer. This leads to the fact, that the double-conical shape of the kapton is preserved even after material was removed.

As distinct from the first run, one can see that here the removal of the kapton layer is not that advanced, although the second run lasted longer and was performed at an even higher gain. This can be explained by the fact, that the second run was performed with four completely new GEMs, whereas the GEMs of the first run were used before for studying charging-up effects.

Interpretation of the results

After these two measurements one can say that a quadruple GEM stack is able to run with a uniform gain and a negligible deterioration of the energy resolution within the projected lifetime of the TPC, even at much higher gains than foreseen for the upgraded TPC. Also the tested materials did not show a negative effect on the detector performance. That is the reason why the other materials were tested from now on.

To distinguish between classical ageing, which refers to depositions on electrodes, the removal of the kapton was named "etching". From simulations like [27] it is known that a change of the hole geometry can result in a change in gain. Even though these studies did not simulate a removal of the kapton layer, one can assume that etched GEM holes can produce a change in gain. This can explain the degradation of the energy resolution, as well as the dependence of the energy resolution on the position of the source. Since it is assumed that the etching of the kapton is a process which first removes the kapton continuously over time and second is proportional to the amount of charge, the etching of the holes is probably not uniform across the irradiated area. This could lead to an increase of the local gain variations and result in a degradation of the energy resolution. A dedicated simulation of the etching effect will be presented in chapter 3 and a comparison to this measurement in chapter 4.

2.3.2 Measurement testing the epoxy adhesive

The measurement was performed with a stack of S-LP-LP-S GEMs, which were in use before. The gain of the quadruple stack was tuned to about 10 000, the gain of the triple GEM stack to 8000. All in all, 78 $\mathrm{mC/cm^2}$ were accumulated in 31 days. The measurement had to be interrupted at around 15.5 $\mathrm{mC/cm^2}$ due to a software error. The two parts were merged together afterwards.

The results of the measurements are shown in Figure 2.15. One can see in Figure 2.15 (a) and (c), that the gain of the triple as well as of the quadruple GEM stack stayed constant. The only exception is visible at around 50 $\mathrm{mC/cm^2}$, where a new gas bottle was connected. Afterwards a loss of gain by about 10 % is visible in the relative peak position and the relative anode current. Since the gas bottle is the only thing that changed, one can assume that the ratio of Ar-CO_2 changed a little bit towards a higher CO_2 concentration. Nonetheless no slope in the gain curves are visible, so that one can concluded that the gain remained constant.

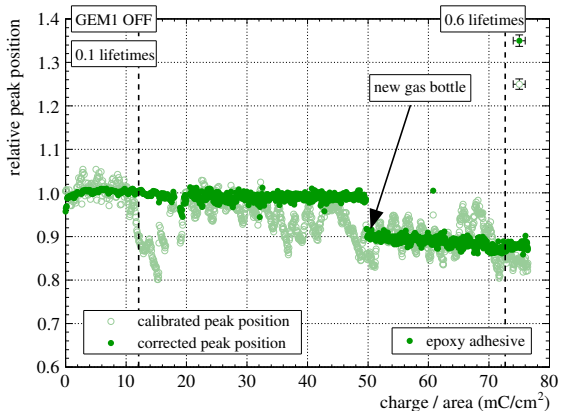

(a) Calibrated and corrected peak position.

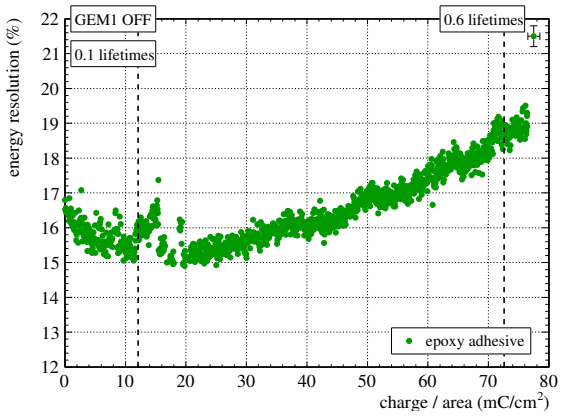

(b) Energy resolution extracted from the calibrated pulse-height spectra.

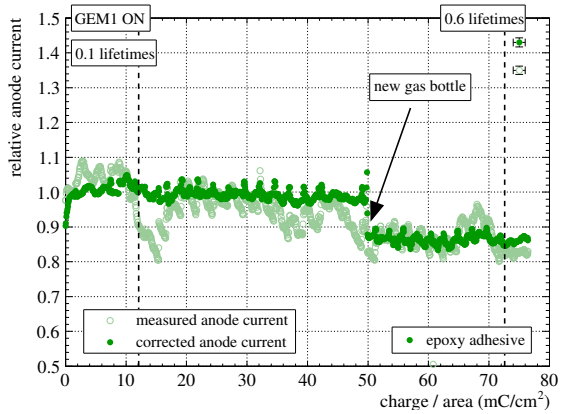

(c) Measured and corrected anode current.

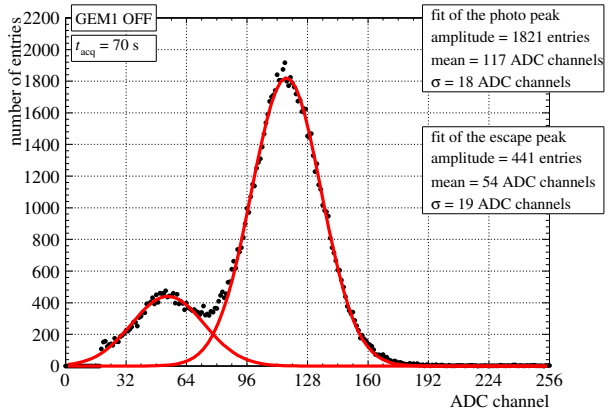

(d) Calibrated and fitted pulse-height spectrum obtained at 12.1 mC/cm^2 (0.1 lifetimes).

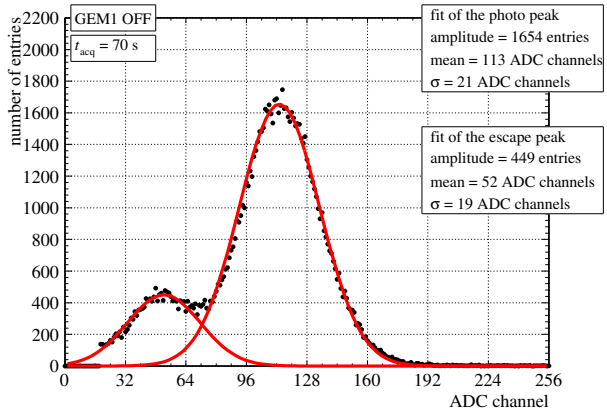

(e) Calibrated and fitted pulse-height spectrum obtained at 72.6 mC/cm^2 (0.6 lifetimes).

Figure 2.15: Results of the first measurement testing the epoxy adhesive, performed in Ar-CO_2 (70-30).

In Figure 2.15 (b) the energy resolution is shown. In here a continuous degradation is discernible, shortly after the first 20 mC/cm^2. The energy resolution decreased from 15 % by

30 % to about 19.5 %. This effect can also be seen in the pulse-height spectra in Figure 2.15 (d) and (e). In the first pulse-height spectrum a clear minimum between escape and main peak is visible. In the pulse-height spectrum obtained at 0.6 lifetimes, the minimum is not that clear anymore, because the two peaks widened.

Additional measurement

The measurement was repeated with slightly lower gain, for about 36 days. The complete analysis can be seen in section C.3. During the measurement about 60 mC/cm^2 could be accumulated with a S-LP-LP-S stack of used GEMs. Also here no continuous degradation of the gain was monitored, but a degradation of the energy resolution.

Interpretation of the results

One can say that both measurement showed the same effect, namely a degradation of the energy resolution at stable gain. The measurements suggest that this epoxy produces ageing in the GEMs. However both measurements were performed with GEMs which have been used in previous measurements. In addition, this type of epoxy is quite well known for not producing ageing, at least in MWPCs. According to the ageing study of the ALICE TPC Collaboration presented in [28, p. 34], a similar epoxy (Araldite 2012) does not produce ageing in MPWCs. Therefore no final conclusion can be drawn concerning the outgassing behavior of the epoxy.

2.3.3 Measurement testing the resistors and the solder cleaned with acetone

In this subsection the measurement with the soldered resistors are presented. At the beginning of the measurements a problem with the gas quality occurred which will be explained first.

Shortly after starting the first measurement a new gas bottle was connected to the gas line. During the next hours the anode current increased by a factor of about 11. Also currents on the electrodes of the GEMs, measured by the power supplies as well as the cathode current changed dramatically. Even though the new gas bottle was labeled Ar-CO_2 (70-30) like the old one, the new bottle had probably a much lower CO_2 concentration than indicated on the data sheet. Since the number of primary electrons changed with the mixing ratio of the gas, no reasonable gain can be given for these measurements. In addition the accumulated charge per area is very high.

The first measurement can be seen in Figure 2.16. With a stack of used S-S-S-S GEMs a charge per area of about 1050 mC/cm^2 could be accumulated in 24 days. The oxygen content was constant at about 40 ppm. The resistors in the box were cleaned with acetone before the measurement started. No continuous degradation of the energy resolution or gain was monitored. The jump in the peak position and the two jumps in the anode current are not understood, especially because the peak position at around 530 mC/cm^2 increases, whereas the anode current decreases.

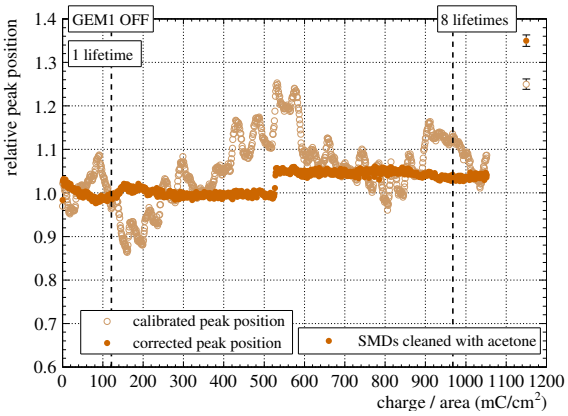

(a) Calibrated and corrected peak position.

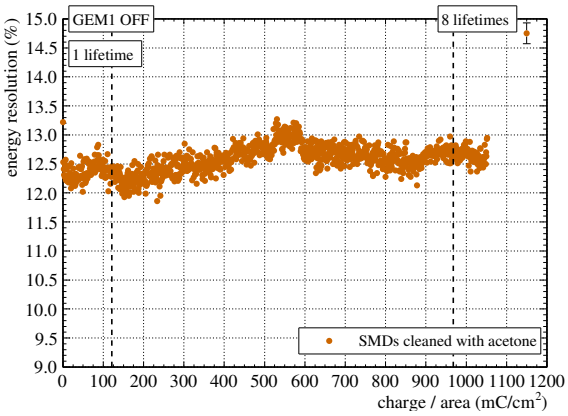

(b) Energy resolution extracted from the calibrated pulse-height spectra.

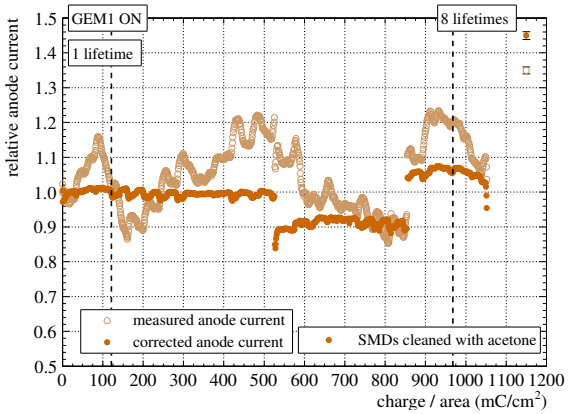

(c) Measured and corrected anode current.

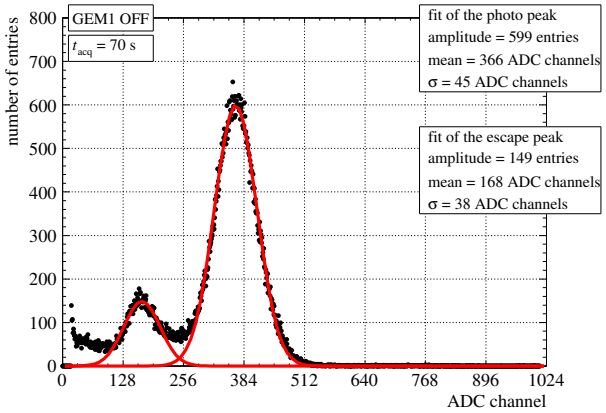

(d) Calibrated and fitted pulse-height spectrum obtained at 121 mC/cm^2 (1 lifetime).

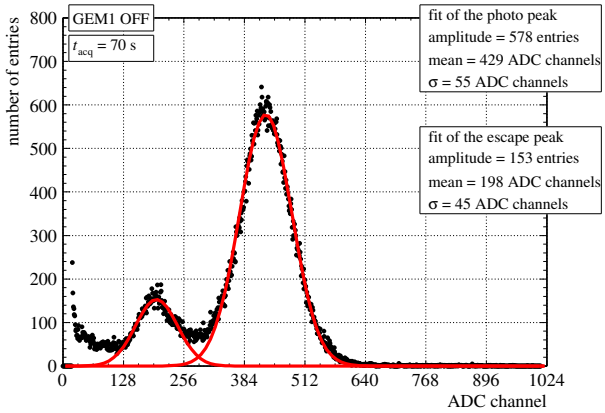

(e) Calibrated and fitted pulse-height spectrum obtained at 968 mC/cm^2 (8 lifetimes).

Figure 2.16: Results of the first measurement testing the SMDs cleaned with acetone, performed in Ar-CO_2 (70-30).

Additional measurement

A second run was performed, which can be seen in the appendix in section C.4. The resistors in the outgassing box were painted with polyurethane this time. About 1800 mC/cm^2 could be accumulated within 38 days. Also here no degradation of the energy resolution or the gain could was monitored within the projected lifetime of the GEM-based TPC.

Interpretation of the results

If one leaves aside the problem with the unknown CO_2 concentration one can say that the resistors, the soldering as well as acetone and polyurethane do not produce ageing within the projected lifetime of the upgraded TPC.

2.4 Long-term measurements in Ar-CH_4 (95-5)

Even though methane is not foreseen as quench gas in the upgraded TPC, it was also tested in the ageing setup, because it is quite common in large-scale TPCs. A big advantage of methane is that one can achieve high electron drift velocities, even at low electric fields. This allows a fast readout of the detector [29, p. 150]. In addition, at the maximum drift velocity, methane is more insensitive to temperature and pressure variations.

The first measurement in Ar-CH_4 (95-5) is divided into two parts. The first part was performed with a S-LP-LP-S stack and a relatively poor energy resolution. To improve the sensitivity, the voltage settings were optimized and the measurement was restarted with a new GEM1, 2 & 3, keeping the previously used GEM4. Due to a lack of LP foils, the new stack consisted of S-S-S-S GEMs. This second part of the measurement will now be presented. The first part is shown in the appendix in section D.1.

The gain of the quadruple GEM stack was tuned to 4200. With a duration of 25 days, an overall accumulated charge of about 75 mC/cm^2 was measured. The gain of the triple GEM stack was set to 3500 with an average rate in E_{T1} of about 280 Hz. The oxygen content of the gas was monitored continuously and was stable around 45 ppm during the complete measurement. The measurement was stopped because of an empty gas bottle. Afterwards the gas was changed to Ar-CO_2 (70-30) and the system was tuned to the same gain and operated for additional 15 days. In addition to the 75 mC/cm^2 accumulated in Ar-CH_4, 30 mC/cm^2 were measured in Ar-CO_2 (70-30).

The results of the run can be seen in Figure 2.17. Since the possible ageing is mostly given by GEM4, the accumulated charge of the first part is taken into account. This is the reason why the measurement does not start at 0 mC/cm^2 but at 84 mC/cm^2. If one focuses first in the methane part of the measurement, one can clearly see that the corrected peak position shown in Figure 2.17 (a) degrades continuously during the complete measurement. The overall loss of the peak position is about 5 %. At the same time one can see in Figure 2.17 (b) that also the energy resolution degrades continuously. In Figure 2.17 (c) the anode current with GEM1 on is shown. Here one can also see a continuous degradation during the complete measurement. Different to the peak position, a total loss of about 30 % in the corrected anode current is monitored.

In Figure 2.17 (e) and (f) two pulse-height spectra are shown, one at 0.7 lifetimes and another at 1.2 lifetimes of the upgraded TPC. One can see that there is a clear separation between escape and photo peak. The photo peak also appears symmetrically. Since the energy resolution of the aged GEM is still quite good, one cannot see any dramatic changes in the pulse-height spectra.

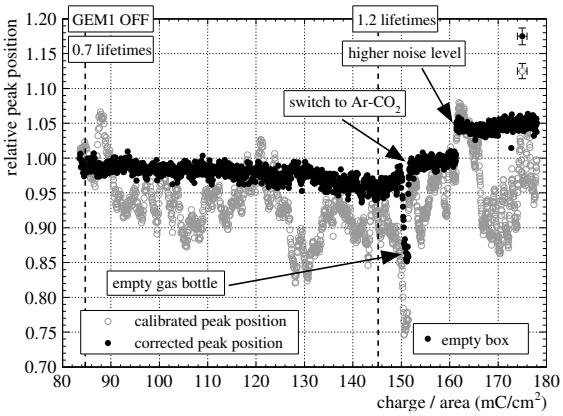

(a) Calibrated and corrected peak position.

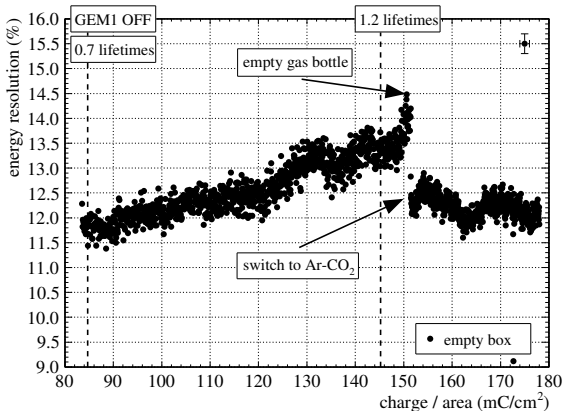

(b) Energy resolution extracted from the calibrated pulse-height spectra.

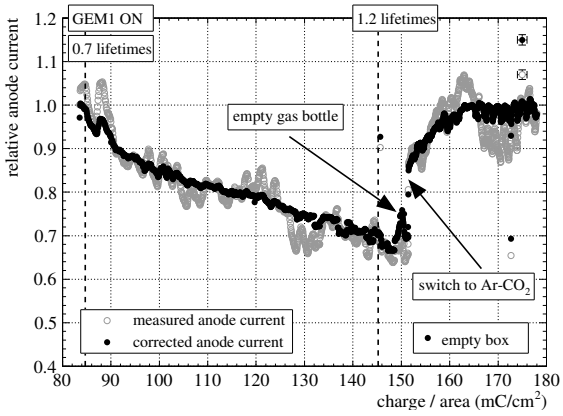

(c) Measured and corrected anode current.

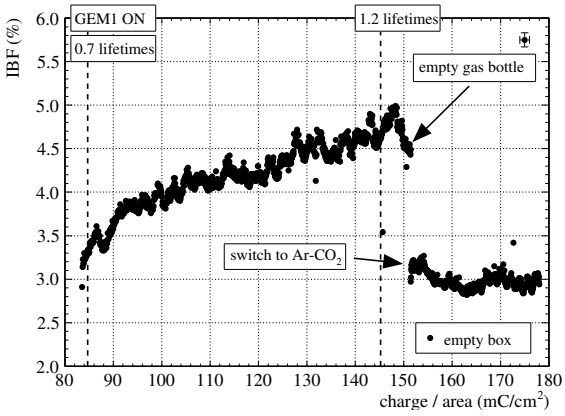

(d) Measured IBF.

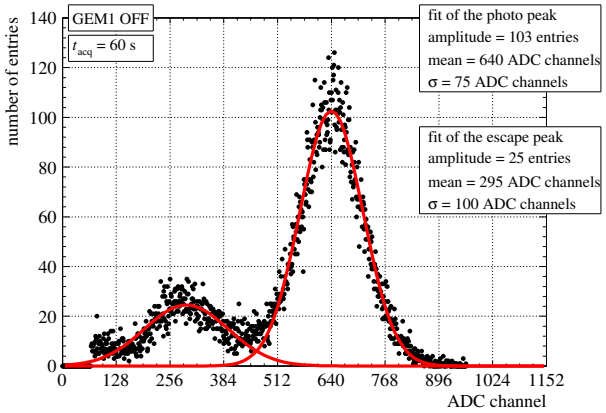

(e) Calibrated and fitted pulse-height spectrum obtained at 84.7 mC/cm^2 (0.7 lifetimes).

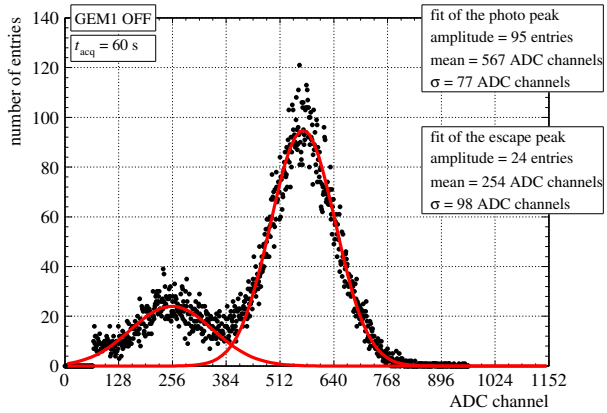

(f) Calibrated and fitted pulse-height spectrum obtained at 154.2 mC/cm^2 (1.2 lifetimes).

Figure 2.17: Results of the second part of the first measurement performed in Ar-CH_4 (95-5).

In Figure 2.17 (d) the measured IBF is shown. Since the anode current and the cathode current both depend in the same way on the temperature and pressure variations, no correc-

tions had to be done. The T and p dependencies were reduced in the calculation. Since the setup was not tuned to provide a good IBF, the measurement started at a bad value of about 3 %. Nevertheless one can see that the IBF degrades continuously during the entire methane measurement.

In the part using Ar-CO_2 one can see a complete different behavior. The energy resolution, the gain (peak position and anode current) and the IBF stay stable during this part of the measurement. Only a jump in the peak position due to noise (higher noise level), as well as a saturation in the anode current was monitored. The degradation of the detector performance monitored in Ar-CH_4 stopped immediately in Ar-CO_2.

SEM analysis with SEs

For a microscopic study of the irradiated GEMs, a SEM analysis has been carried out. The report, including *some* of the images and spectra, is documented in [30].

In Figure 2.18 (a) one can see a picture of GEM4 Top. Again a colored, approximately 1 cm^2 large dot in the irradiated area of the foil is visible. Magnifications of this area made with

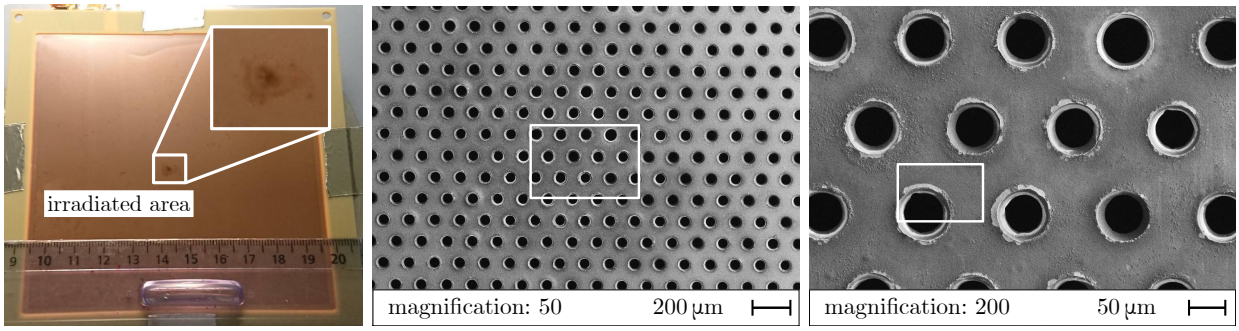

(a) Picture of GEM4 Top. **(b)** Top view of the irradiated area. **(c)** Magnification of (b).

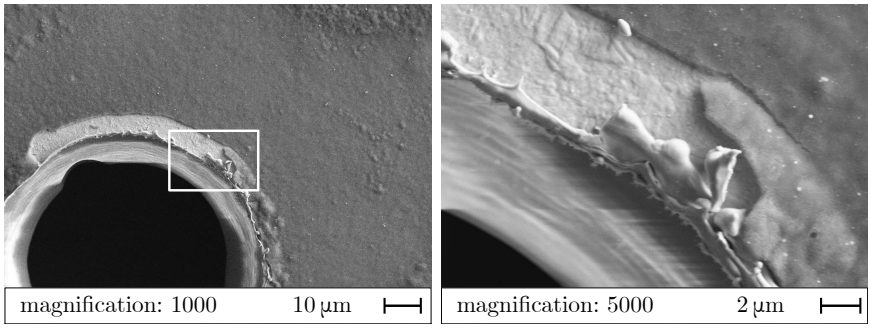

(d) Magnification of (c). **(e)** Magnification of (d).

Figure 2.18: Picture and images made with SEs of GEM4 Top, adapted from [30, p. 4, 6].

SEs are shown in Figure 2.18 (b) - (e). In the magnification in Figure 2.18 (c) one could mean that most of the holes have some depositions close the holes. In the largest magnification in Figure 2.18 (e) one can see that there are no depositions at the edge of the electrode, but a layer of depositions all over the copper surface itself. Only close to the holes some parts of this layer are fractured and removed. In one of these positions the thickness of the layer was measured to be about 450 nm. At these positions one can also see molten and re-solidified splashes of material, which come probably from discharges.

Since it is well known from CH_4-induced ageing in MWPCs that the plasma of the avalanches can produce hydrocarbons, an elemental analysis of the last GEM was carried out.

SEM analysis with EDXS

To identify the chemical composition of the layer, an Energy-Dispersive X-ray Spectroscopy (EDXS) was carried out on three different positions on GEM4 Top. For an EDXS the characteristic X-rays emitted by the excited atoms in the interaction volume are used to identify and quantify the elements present in the probe. Initially the electron beam raises the atoms in the interaction volume of the probe to an excited state. These excited atoms emit characteristic X-rays, meaning photons with sharply defined energies for the specific shell of the element. The energy and the amount of emitted X-rays can be measured and plotted in an emission spectrum. By checking a database where the energies of the photons for all elements are listed, the peaks in the X-ray emission spectrum can be identified to a specific shell of an element. Exceptions are hydrogen, helium and lithium. Since these elements do not emit characteristic X-rays, they cannot be identified via an EDXS. Another limitation of the X-ray analysis concerns the amount of atoms in the beam-excited volume. Elements with a proton number between 4 and 11 can only be detected if there is a large amount of atoms on the probe. For all the other elements the mass fraction in the beam-excited volume must be larger than 0.2 wt%. [26, p. 40]

The positions were the spectroscopy was carried out can be seen in Figure 2.19 (a) and (b). The first emission spectrum was taken far away from the irradiated area and serves as a

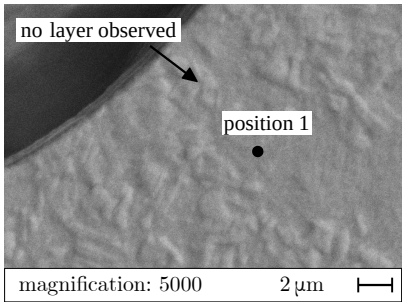

(a) Image of the reference area made with SEs.

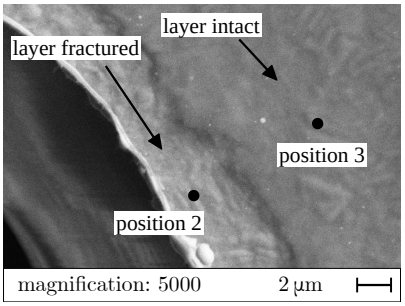

(b) Image of the irradiated area made with SEs.

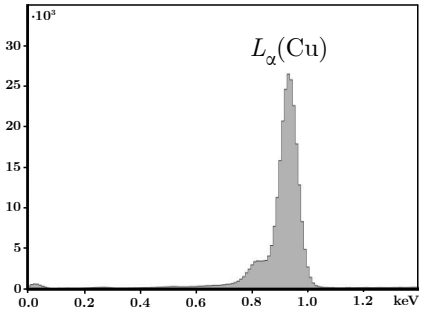

(c) Spectrum taken at position 1.

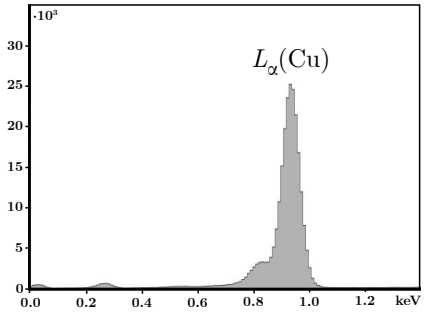

(d) Spectrum taken at position 2.

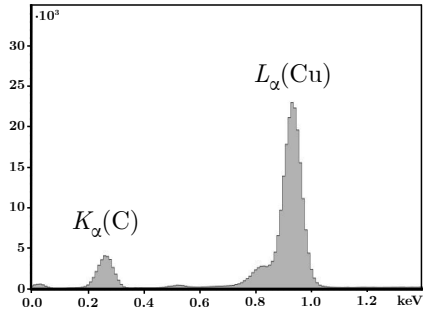

(e) Spectrum taken at position 3.

Figure 2.19: Images of GEM4 Top made with a SEM and X-ray emission spectra of three different positions on GEM4 Top, adapted from [30, p. 8].

reference. The X-ray emission spectra from position 2 & 3 were taken in the irradiated area.

In Figure 2.19 (b) one can see the two different positions. Position 2 is close to the edge of the electrode, where the observed layer was fractured and removed. Position 3 is located further away from the edge than position 2. In there the layer was completely intact.

In Figure 2.19 (c) - (e) one can see the three X-ray emission spectra made with the EDXS. To identify the peaks, the characteristic energies of the X-rays listed in [31, p. 86 f.] were used. In all the emission spectra one can see the L_α peak of copper at 0.93 keV. The emission spectra also showed the K_α peak of copper at 8.04 keV and the K_β peak at 8.91 keV. This part was cut out in order to magnify the lower energy range. The emission spectrum taken at position 3 shows an additional peak, which can be identified as the K_α peak of carbon, with an energy of 0.28 keV. As mentioned above, the thickness of the layer was measured to be about 450 nm. Since the electron beam of the EDXS penetrates the probe, not only the layer, but also the underlying electrode was hit by the beam. This is the reason, why also the copper peak was measured at position 3. One can conclude, that carbonic depositions were placed all over the electrode of the irradiated area. Only close to some edges the layer was partly removed.

Additional measurement

Another measurement in Ar-CH_4 (95-5) was performed with similar settings. The complete analysis as well as the measured and corrected results can be seen in the appendix in section D.2. Since the same degradation of the detector performance was observed, another analysis using a SEM was performed, which is also shown in section D.2.

Two images of the analysis with SEs from the second run can be seen in Figure 2.20 (b) and (c). In there two typical holes are shown, one of the reference area of GEM4 and another of the irradiated area. By comparing these two images one can see, that no change of the hole geometry occurred. The kapton as well as the copper diameter remained the same before and after the measurement. An uncertainty of the diameters within a few micrometers coming from the production process has to be granted. With this information one can be sure, that the deterioration of the detector performance was triggered by the depositions on the electrodes and not by a change of the hole geometry.

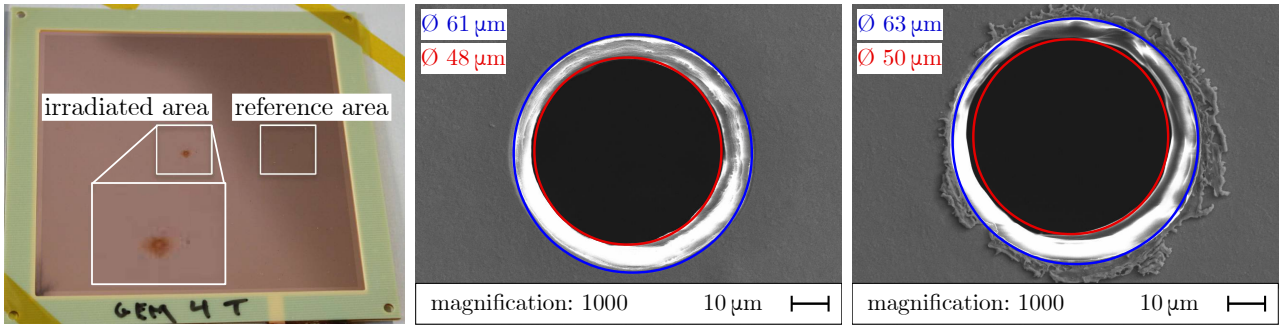

(a) Picture of GEM4 Top. **(b)** Hole in the reference area. **(c)** Hole in the irradiated area.

Figure 2.20: Picture and SEM images made with SEs of GEM4 Top, provided by A. T. Pérez Fontenla. Labels, magnification of the irradiated area and rings inserted afterwards.

Interpretation of the results

Together with the SEM analysis the monitored deterioration of the detector performance in the two measurements with methane can be explained. The polymers produced in the plasma of the electron avalanche follow the drift lines towards the electrodes. On there they will be deposited and form a thin layer, which covers the complete electrode in the irradiated area. These carbonic depositions shield the electrodes. Since they are non-conductive they charge up and produce a second electric field in the opposite direction of the field produced by the electrodes. Therefore the depositions lead to a reduction of the electric field in the GEM holes. This can also explain the different gain drops monitored in the peak position and the anode current. Since the only difference is the usage of GEM1, which leads to a largely increased rate, the charging-up of the depositions changes. If the system is exposed to a large rate, the charging-up of the depositions is increased and therefore the total field is reduced much more, than with GEM1 OFF. Also the degradation of the IBF can be explained. Since it can be assumed that the amount of depositions is proportional to the amount of charge, one can say that the first GEMs of the stack have much less depositions than GEM3 or GEM4. Therefore the reduction of the gain is much larger for the last GEMs than for the first two GEMs. A reduction of the gain in the lower part of the detector leads to a lower anode current, whereas the cathode current stays more or less constant. This leads to a worsening of the IBF. The degradation of the energy resolution can also be understood by the change of the gain. Since the production of deposits can be assumed to be proportional to the amount of charge, the covering of the electrodes is not equal over the complete irradiated area. This leads to an increase of the statistical gain fluctuations and therefore to a loss of energy resolution.

2.5 Long-term measurements in Ne-CO_2-N_2 (90-10-5)

As mentioned earlier, the baseline gas mixture of the upgraded TPC is Ne-CO_2-N_2 (90-10-5). An intensive R&D study has been carried out by the ALICE TPC Upgrade Collaboration to find satisfying voltage settings to operate the S-LP-LP-S GEM stack at a gain of 2000, with an IBF of less than 1 % as well as a $\sigma(^{55}\mathrm{Fe})$ of about 12 %. These voltage settings[23] are listed in Table 2.4. These baseline settings have been used for the ageing tests in Ne-CO_2-N_2. Only

	$E_\mathrm{D} = 400\,\mathrm{V/cm}$
$\Delta U_\mathrm{GEM1} = 270\,\mathrm{V}$	$E_\mathrm{T1} = 3500\,\mathrm{V/cm}$
$\Delta U_\mathrm{GEM2} = 230\,\mathrm{V}$	$E_\mathrm{T2} = 3500\,\mathrm{V/cm}$
$\Delta U_\mathrm{GEM3} = 320\,\mathrm{V}$	$E_\mathrm{T3} = 500\,\mathrm{V/cm}$
$\Delta U_\mathrm{GEM4} = 320\,\mathrm{V}$	$E_\mathrm{T4} = 3500\,\mathrm{V/cm}$

Table 2.4: Baseline voltage setting of the GEM-based TPC in Ne-CO_2-N_2 (90-10-5).

the drift field E_D was reduced to 200 V/cm, because the potential of the cathode would have exceeded the maximum output voltage of the power supply, due to the 10 cm drift height of the field cage. The lower drift field had no negative impact on the measurements, because it should still have been high enough to separate all created primary charge in the drift volume as well as to guarantee an electron collection efficiency of 100 %.

[23] In the ALICE TPC Upgrade Collaboration, the voltage settings are named “voltage settings B”.

GEM2, 3 & 4 of the S-LP-LP-S stack were new GEMs, whereas GEM1 was used in a previous Ar-CO_2 measurement as GEM4. Due to the baseline settings, the gain of the quadruple GEM stack was 2000. Because of this low gain, the amplification of the triple GEM stack had to be increased to acquire a pulse-height spectrum. With GEM1 OFF the gain was tuned to about 38 000. The measurement lasted all in all 18 days. It had to be stopped at 0.4 mC/cm^2 due to the announcement of a power cut in the laboratory. The two parts were later on merged together (interruption due to power cut). If one compares the run to the measurements in the argon-based gas mixtures, much less charge was accumulated, due to the lower gain as well as lower number of primary electrons and the much larger irradiated area. This is the reason why only a charge corresponding to less than 0.02 TPC lifetimes could be accumulated. The results of the measurements are shown in Figure 2.21. One can see that no systematic change in the gain nor energy resolution occurred. One jump in the relative peak position and two jumps in the relative anode current were most probably not caused by the gas mixture.

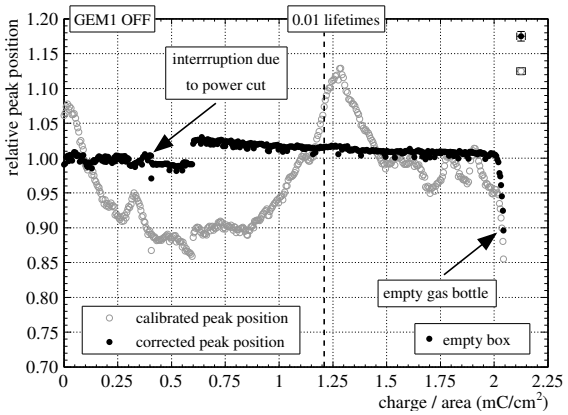

(a) Calibrated and corrected peak position.

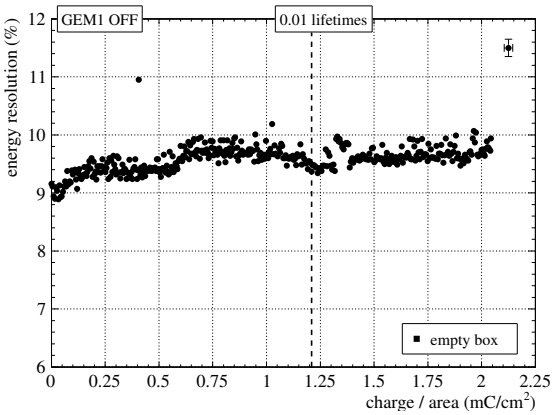

(b) Energy resolution extracted from the calibrated pulse-height spectra.

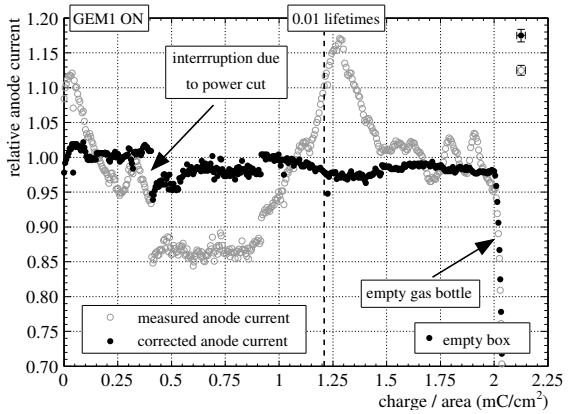

(c) Measured and corrected anode current.

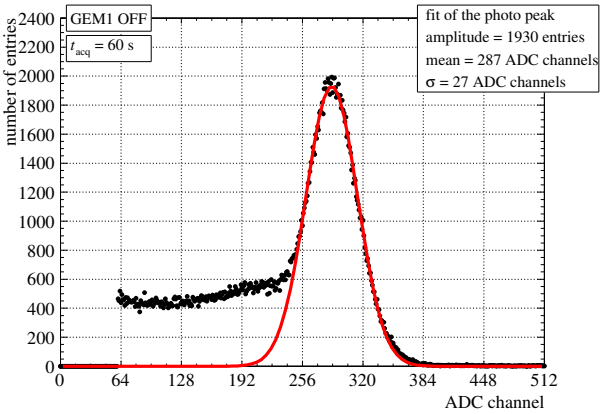

(d) Calibrated and fitted pulse-height spectrum obtained at 1.21 mC/cm^2 (0.01 lifetimes).

Figure 2.21: Results of the measurement performed in Ne-CO_2-N_2 (90-10-5).

Interpretation of the results

Because the dose is very limited, no reasonable prediction for the upgraded TPC can be given. Since neither Ne, nor CO_2 or N_2 polymerize, there should be no ageing from the gas itself.

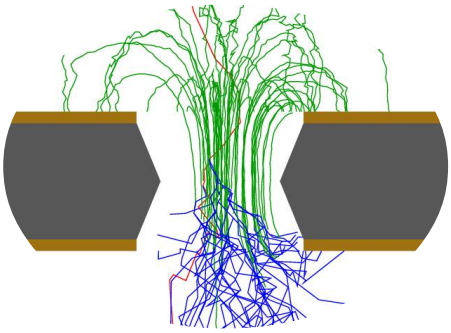

Chapter 3

Etching Simulations using Garfield^{++}

Many detailed studies about the impact of the hole geometry on the performance of a GEM detector do not exist so far. Like from simulations presented in [27] it is known that changes of the hole geometries can result in a change of gain. In there the focus was on misalignment studies, meaning small shifts between the holes in the top and bottom electrode of GEM. A change of gain of a few percent compared to the standard GEM (S-GEM) was observed.

To study the effect of *etched* GEM holes on gas gain and especially energy resolution, a simulation was carried out with the Garfield^{++} toolkit. This is a simulation tool especially for gaseous and semi-conductor detectors. To simplify the comparison with the measurements, the parameters used in the simulations should be as close to the experiment as possible. However a simulation of a complete quadruple GEM stack with reasonable statistics and some iterations with different hole geometries is quite complex and needs a lot of computing time. Therefore only a single GEM setup was simulated with the voltage settings of GEM4 of the measurement, presented in subsection 2.3.1.

3.1 Simulated setup and GEM hole geometries

The simulated setup with one GEM and the electrodes can be seen in Figure 3.1. The cathode

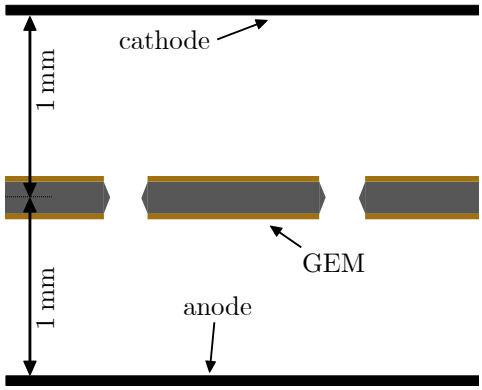

Figure 3.1: Schematic drawing of the simulated setup.

and anode were placed at 1 mm distance to the center of the GEM. The GEM was modeled with the standard parameters, explained in section 1.3. Although a MP-foil was installed as last

GEM in the experiment, a standard pitch GEM was used for the simulations, because MP-foils are rare and a custom ALICE design.

To model an etched GEM hole, the cross section shown in Figure 2.14 was used. It was assumed, that the shape of the kapton does not change during the etching process. Therefore simulations were carried out, where the difference between outer and inner diameter remains during each etching step. The inner (outer) diameter of the kapton was systematically increased from 50 µm (70 µm) to 90 µm (110 µm) in steps of 10 µm.

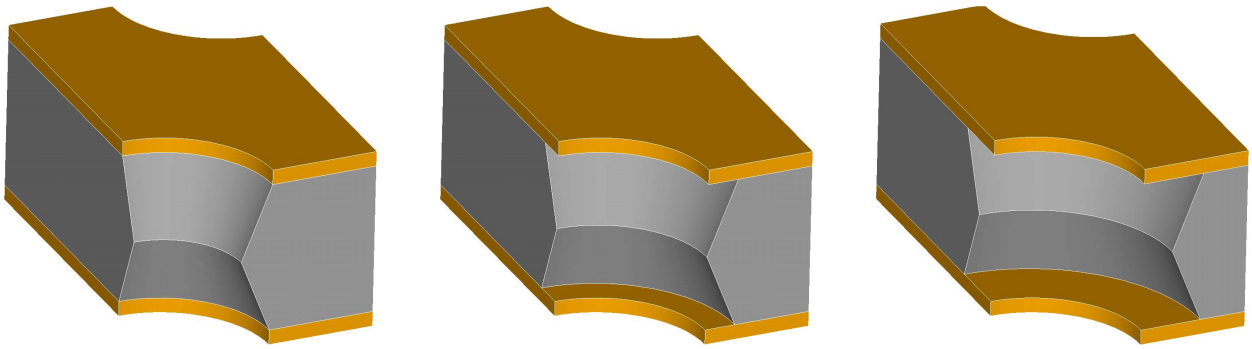

(a) Inner diameter: 50 µm. **(b)** Inner diameter: 70 µm. **(c)** Inner diameter: 90 µm.

Figure 3.2: Simulated elementary cells of a GEM.

Three of the five elementary cells representing the different etching levels can be seen in Figure 3.2. First the cell of the standard GEM hole in Figure 3.2 (a), an intermediate degree of etching in (b) where the inner diameter of the kapton is the same as the copper diameter and finally the maximum degree of etching in (c).

3.2 Calculation of the electric field

The calculations of the electric field for each of the five geometries were made with ANSYS 16.1, a tool to do finite element analysis. A sample script to simulate the electric field of a GEM at the Garfield^{++} homepage was used and modified. The results were afterwards imported into Garfield^{++}.

The voltage settings of the measurements had been: $E_{\mathrm{T3}} = 2000\,\mathrm{V/cm}$, $\Delta U_{\mathrm{GEM4}} = 370\,\mathrm{V}$ and $E_{\mathrm{T4}} = 4000\,\mathrm{V/cm}$. These settings were also used for the simulations. Beside easy comparison between simulations and measurements, these settings have another advantage. With an electric field of 2000 V/cm above a S-GEM with 370 V, an electron collection efficiency of about 95 % is achieved. Also the electron extraction efficiency is maximized to about 60 % [32, p. 18]. This benefits the statistics, since most of the charge gets amplified and detected on the anode.

A visualization of the electric field can be seen in Figure 3.3. In there the 2-dimensional projections of electric drift lines are plotted and superimposed with cross sections of the corresponding GEM holes. These drift lines show ions simulated in Garfield^{++}. To do so the ions were placed beneath the GEM and close to the bottom electrode. During the drift of these ions, the diffusion was disabled so that the ions follow the electric field lines. Every calculated point of the drift line was saved and later combined to a line. Even if the ions were placed in one line in the center of the GEM (y-position = 0), they move in all three dimensions during their drift. That is the reason why the visualization is just a 2-dimensional projection of the drift lines.

In the Figure 3.3 (a), (b) and (c) one can compare the electric field inside the GEM holes for the three different geometries. First one can see that the drift lines in the middle of the GEM hole are not as close together as at the side of the hole. Second one can see that the drift lines starting at the lower and inner side of the bottom electrode are squeezed together with increasing hole diameter. This leads to the conclusion that the electric field gets stronger the more advanced the etching process is.

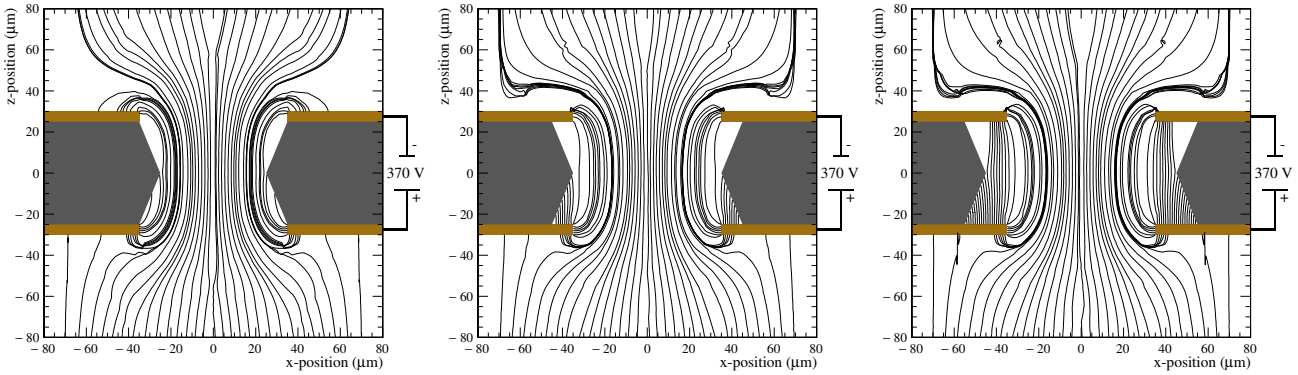

(a) Inner diameter: 50 µm. **(b)** Inner diameter: 70 µm. **(c)** Inner diameter: 90 µm.

Figure 3.3: 2-dimensional projection of ion drift lines inside simulated GEM holes.

3.3 Garfield^{++} simulations

For the simulations itself also a sample script for a single GEM provided on the Garfield^{++} homepage was used and modified. The simulations were performed for Ar-CO_2 (70-30) with the appropriate ion mobility files of Ar^+ drifting in pure argon[1]. The penning fraction was set to 57 % and the standard conditions for temperature and pressure of 20 °C and 1 atm, respectively, were selected.

To irradiate the GEM uniformly, the initial positions of the primary electrons were chosen randomly within the elementary cell shown in Figure 3.4. The electrons were placed 0.5 mm above the GEM. Then the calculation of the drift as well as the amplification process and the subsequent drift of the produced secondary electrons and ions was performed. During this all calculated drift line points of all particles were saved in ROOT files. In this way the complete trace of each particle could be analyzed afterwards.

This cycle was repeated several million times. To simulate a ^{55}Fe source, 209 primary electrons were simulated with an identical initial position. These primary electrons, the secondary electrons and ions were labeled with a number for the corresponding X-ray. In this way, the gain and multiplication of the primary electrons for each X-ray could be calculated. For the gain every electron reaching the anode was taken into account. For the multiplication the total amount of produced electrons was used, disregarding their final position.

[1] The ion mobility in Ar-CO_2 (70-30) was measured by A. Deisting for an electric drift field up to 950 V/cm. [33] To simulate the movement of ions inside the amplification volume, ion mobility values up to about 60 000 V/cm are necessary. Since these simulations do not deal with the arrival times of ions, the ion mobility of Ar^+ in pure argon should in the first approximation be accurate, even for the calculation of the ion diffusion.

This procedure was performed in the same way for all five hole geometries. To achieve good statistics, 20 000 X-rays were simulated for each geometry, which can be compared to a measured spectrum taken at the anode with an acquisition time of 40 s at a rate of 0.5 kHz.

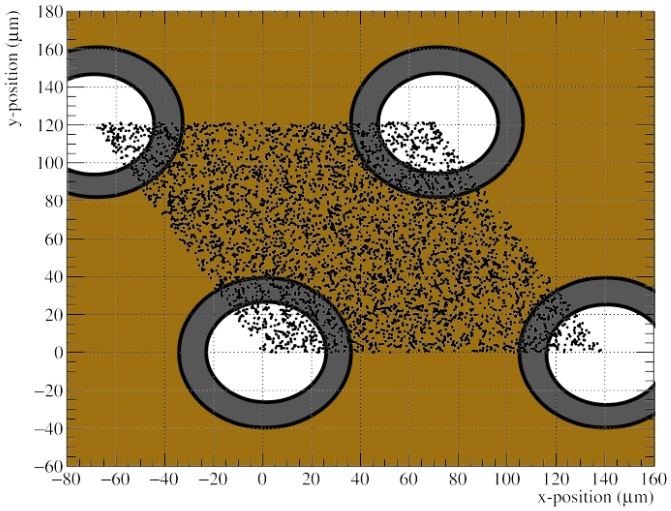

Figure 3.4: Elementary cell of primary electrons, 0.5 mm above the simulated GEM.

3.4 Results of the simulations

Now the results of the simulations will be discussed. First the amplification for the different geometries will be presented then the combination of different hole geometries in a single GEM and its effect on the gain and energy resolution will be analyzed. Afterwards the effect of etching on the amount and the behavior of the produced secondary electrons and ions will be shown.

3.4.1 Amplification of the different degrees of etching

In Figure 3.5 one can see the simulated distribution of gain in black and the distribution of the multiplication in red of the ^{55}Fe source for three different degrees of etching. For both distributions the mean values as well as the standard deviations are given. For the gain distributions the energy resolution is extracted as well.

By comparing the gain distributions of the three hole geometries one can see that the peak does not change much. Its mean value is shifted slightly towards higher gain, but the symmetry of the peak itself remains. That is the reason why the energy resolution becomes a little bit better with increasing kapton diameter.

In contrast to the gain, the multiplication shows a dramatic change with increasing hole diameter. In Figure 3.5 (a) one can see that the multiplication shows a symmetric distribution. With increasing diameter the distribution shows two different effects. First it is shifted towards higher amplification and second it becomes asymmetric with a tail towards higher multiplication. That is why the standard deviation increases quite a lot.

In Figure 3.6 the relative gain and amplification as a function of the inner diameter are shown. One can see that both parameters increase and saturate towards higher diameters. The

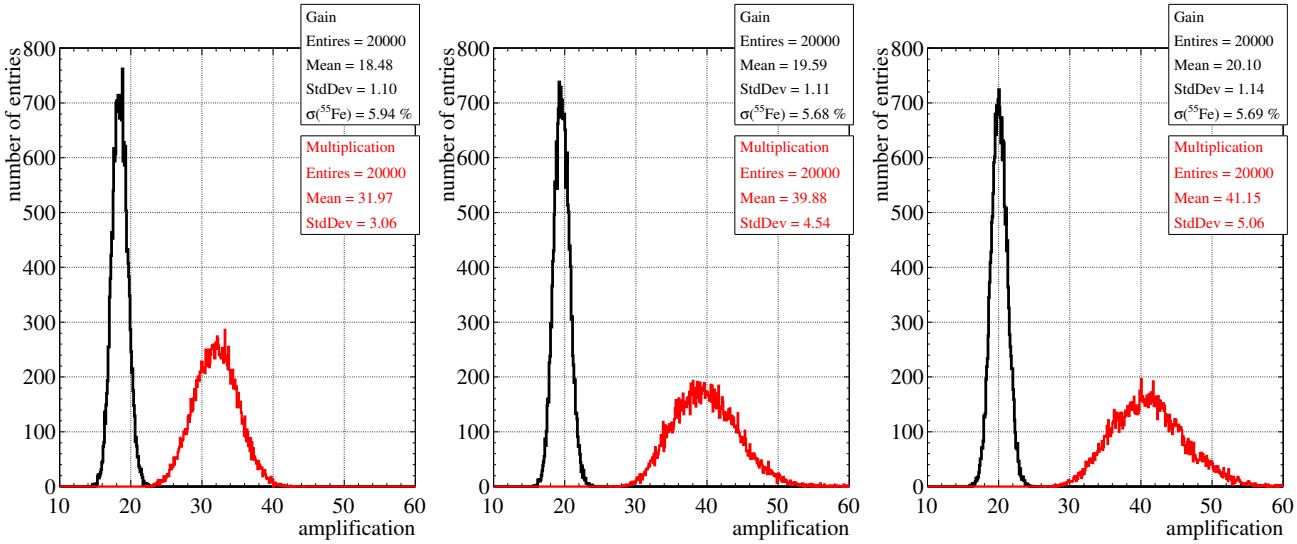

(a) Inner diameter: 50 µm. **(b)** Inner diameter: 70 µm. **(c)** Inner diameter: 90 µm.

Figure 3.5: Simulated distributions of gain and multiplication of a ^{55}Fe source for three different hole diameters.

overall change in gain is about 9 % and in multiplication about 28 %. One can see that the multiplication increases already by 18 % at 60 µm, which leads to the conclusion that the change of the detector performance is considerable within the first 20 µm.

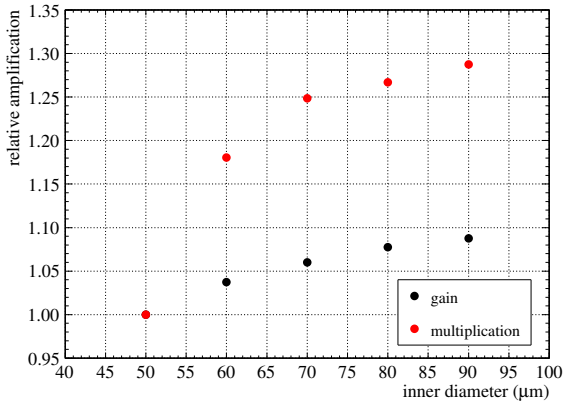

Figure 3.6: Relative change in gain and multiplication as a function of the inner hole diameter.

3.4.2 Distribution of the electron avalanche inside a GEM hole

In order to understand the change in gain and especially in multiplication, one can have a closer look to the distribution of the electron avalanche inside a GEM hole. In Figure 3.7 the spacial distribution of the production of secondary electrons depending on the radius inside GEM holes is shown. These distributions are superimposed with the 2-dimensional projection of the simulated ion drift lines for the appropriate degree of etching.

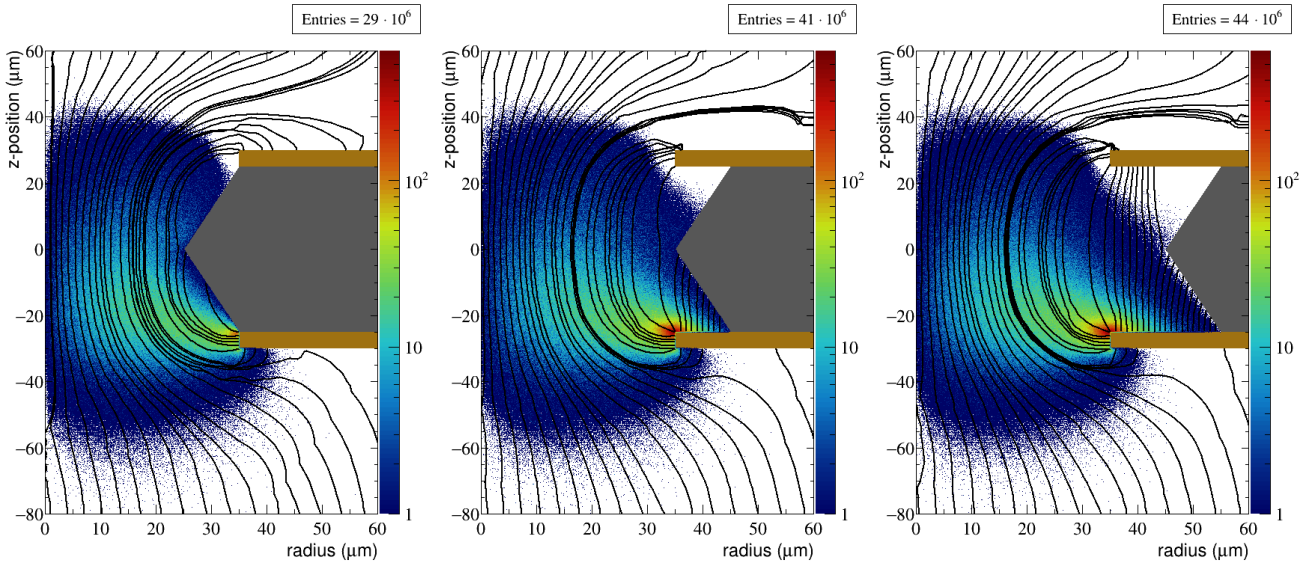

(a) Inner diameter: 50 µm. **(b)** Inner diameter: 70 µm. **(c)** Inner diameter: 90 µm.

Figure 3.7: Distribution of the production points of secondary electrons inside a GEM hole.

In Figure 3.7 (a) one can see the electron avalanches of a standard GEM. The majority of the secondary electrons are not produced in the center of the hole, but closer to the side. One can also see that the number of produced secondary electrons increases close to the bottom electrode. Most of these electrons will end up on the bottom electrode shortly after their production. As expected this can explain the difference between the gain of 18.48 and the multiplication of 31.97. It also shows that it is not possible in a GEM to achieve an electron extraction efficiency close to 100 %.

If the kapton layer is removed as shown in Figure 3.7 (b), one can see that the bottom electrode is exposed on the upper side. This is the reason why electrons which normally would end up on the kapton layer will now be accelerated and amplified. One can see that the red bulk of produced secondary electrons is located at the inner side as well as at the first 5 µm on the upper side of the bottom electrode. Electrons which are produced close to the upper side of the bottom electrode will of course not be extracted and therefore not change the gain of the system. That is why the gain changes from a diameter of 50 µm to 70 µm by only 6 % whereas the multiplication changes by about 25 %.

In Figure 3.7 (c) the last simulated etching diameter is shown. The electron avalanche is not stopped by the kapton layer anymore. Since the only change takes place at the upper side of the bottom electrode, almost no change in the amplification is visible anymore. The gain changes from Figure 3.7 (b) to (c) by only 3 % and the multiplication by only 4 %.

3.4.3 Combination of different degrees of etching

The changes of amplification shown in Figure 3.6 are only valid for a GEM where all holes are equally affected. If one assumes that the etching process depends on the amount of charge, the irradiated area of the GEM in the measurement should consist of holes with different diameters. Since the amount of charge has a Gaussian distribution, one can assume that the innermost

part of the irradiated area consists of maximally etched holes. At the side of the irradiated area the GEM holes should be hardly etched, if at all. In addition the etching of the complete irradiated area should become worse with accumulated charge. To study the effect of different hole diameters within the same GEM, one can use the parameters of the simulated photo peaks listed in Table 3.1.

$\varnothing$	μ	σ
50 µm	18.48	1.10
60 µm	19.17	1.09
70 µm	19.59	1.11
80 µm	19.91	1.14
90 µm	20.10	1.14

Table 3.1: Parameters of the simulated photo peaks.

Gaussian distributions can be calculated with different amplitudes. An example is shown in Equation 3.1. In there it was assumed that 4/5 of the holes of the GEM have the standard diameter of 50 µm and 1/5 an increased diameter of 60 µm. The two Gaussians as well as the summed Gaussian can be seen in Figure 3.8 (a).

$$A = \frac{4}{5} \cdot \exp\left(-\frac{(x-\mu_{50})^2}{2 \cdot \sigma_{50}^2}\right) + \frac{1}{5} \cdot \exp\left(-\frac{(x-\mu_{60})^2}{2 \cdot \sigma_{60}^2}\right) \tag{3.1}$$

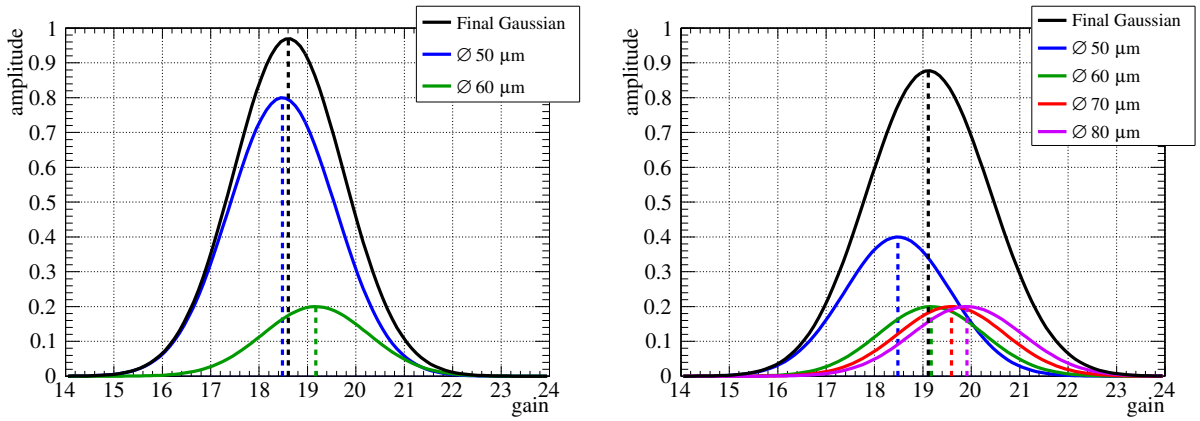

(a) Poorly etched GEM. **(b)** Heavly etched GEM.

Figure 3.8: Two examples of summing Gaussians.

In Figure 3.8 (b) another example is shown, where 2/5 of the holes have the standard diameter of 50 µm and 1/5 of the holes have an inner diameter of 60, 70 and 80 µm, respectively. This procedure was performed for 7 intermediate stages with different hole diameters, between a GEM with standard holes and a GEM with holes of 90 µm inner diameter. A complete list can be seen in Table 3.2.

The position and the energy resolution of the final Gaussian distributions were extracted and plotted in Figure 3.9. In there one can see how the detector performance changes from one

etching stage to another. The plot itself is aligned with Table 3.2 so that one can easily see the different amount of hole diameters of an etching stage.

⌀	I	II	III	IV	V	VI	VII	VIII	IX
50 µm	5/5	4/5	3/5	2/5	1/5	—	—	—	—
60 µm	—	1/5	1/5	1/5	1/5	1/5	—	—	—
70 µm	—	—	1/5	1/5	1/5	1/5	1/5	—	—
80 µm	—	—	—	1/5	1/5	1/5	1/5	1/5	—
90 µm	—	—	—	—	1/5	2/5	3/5	4/5	5/5

Table 3.2: Different stages of etching and their hole geometries.

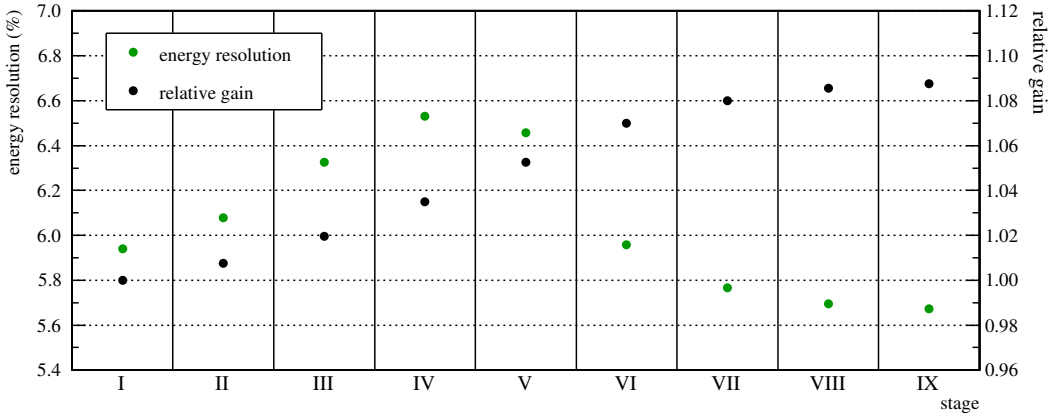

Figure 3.9: Change in energy resolution and gain for different etching stages.

One can see that the gain increases systematically and saturates towards 9 % as already seen in Figure 3.6. Also the energy resolution becomes worth within the first three etching stages. A degradation by 11 % can be seen until stage IV. Afterwards the energy resolution becomes better again and saturates towards 6.7 %, which is a better value than for the GEM with the standard hole parameters. Since the energy resolution represents the local gain variation within the irradiated area, it is clear, that the resolution becomes worse when geometries are superimposed, who produce quite different gains. This is not the case for the last four etching stages. That is the reason why, the energy resolution becomes already better from stage V on. A comparison to the measurements will be made in the next Chapter.

3.4.4 Ending of the drift of the produced ions on the top electrode

Another observation beside the etching were rings on the upper side of the top electrode. To investigate this effect the distributions of simulated ions on the top electrodes for the different hole diameters are plotted and shown in Figure 3.10.

In the three Figures (a), (b) and (c) one can see that most of the ions end up close to the edge of the copper electrode. If one compares this to the drift line plots in Figure 3.3, it becomes clear that a lot of field lines end at the upper edge of the electrode. Nevertheless some structures are visible, which can be better seen in the magnifications in (d), (e) and (f).

Clear and sharply defined rings around the GEM holes are not visible. However one can see some ring-like structures around the holes, especially in Figure 3.10 (a) and (b).

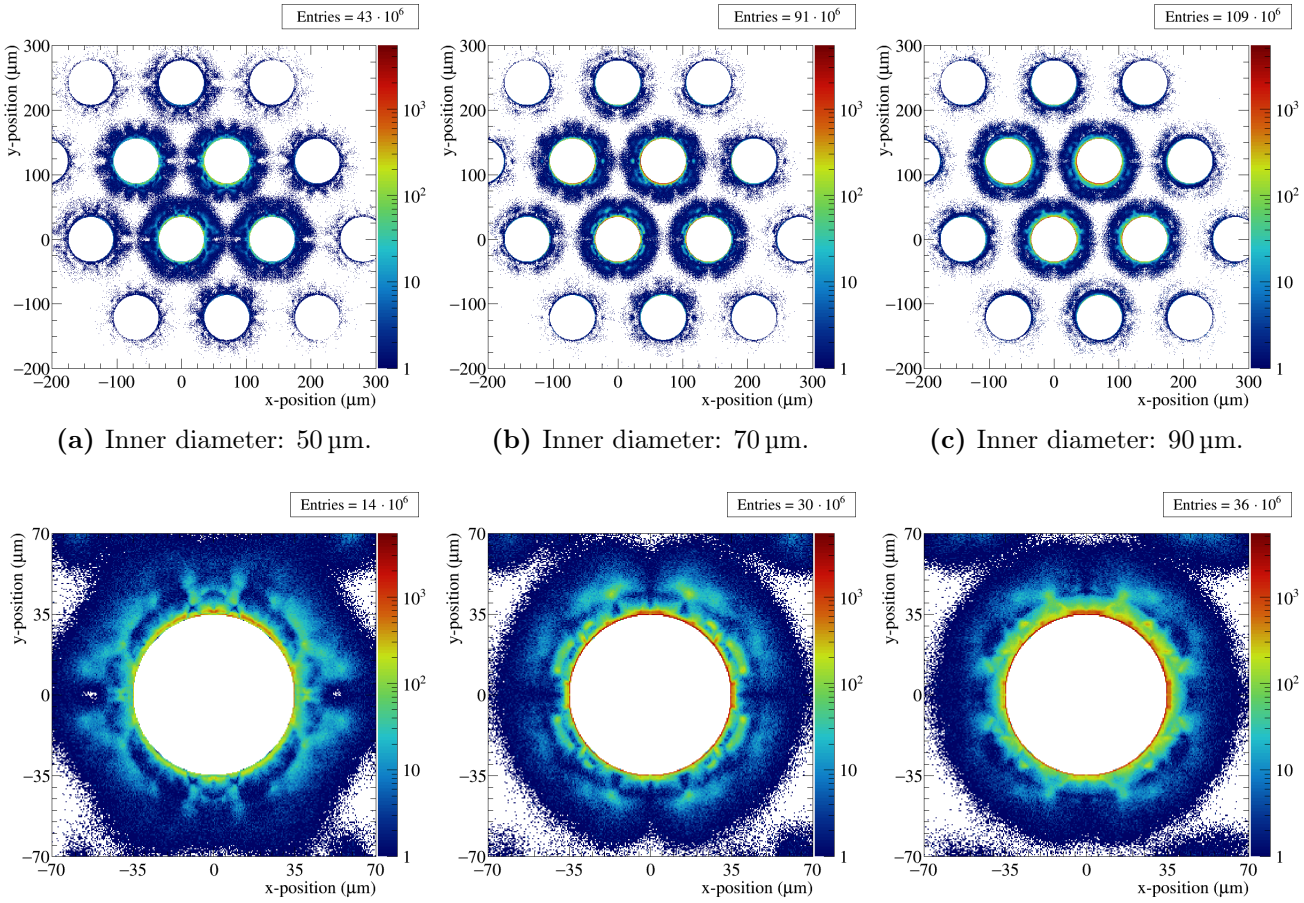

(a) Inner diameter: 50 µm. **(b)** Inner diameter: 70 µm. **(c)** Inner diameter: 90 µm.

(d) Magnification of (a). **(e)** Magnification of (b). **(f)** Magnification of (c).

Figure 3.10: Endpoints of the simulated ions on the top electrode.

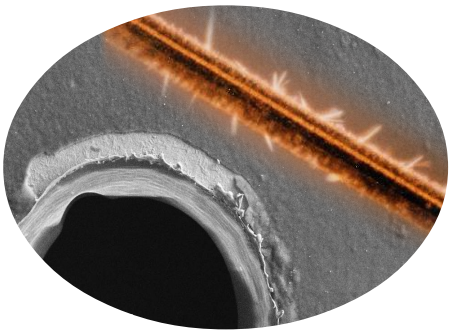

Chapter 4

Comparisons and Conclusions

In this chapter several comparisons, as well as conclusions will be drawn. At first the etching effect will be analyzed by providing a comparison between the performed measurements and simulations in section 4.1. Since the etching of GEMs could be reproduced by scientists of the RD51 Collaboration, a short comparison with their results will also be made. Afterwards the ageing of GEMs in CO_2- and CH_4-based gas mixtures will be compared in section 4.2. In addition a short comparison to another study of CO_2-induced GEM ageing, presented in [21], will be given. Finally a comparison between CH_4-induced ageing in GEMs, single-wire proportional counters and MWPCs will be drawn in section 4.3.

4.1 The etching process in GEMs

4.1.1 Comparison between measurements and simulations

A direct comparison between the simulation of a single GEM discussed in chapter 3 and the measurement of the quadruple GEM stack presented in subsection 2.3.1 will be made. First the focus will be on the degradation of the energy resolution and secondly on the gain performance of the GEMs. Differences such as pitch of the simulated GEM and GEM4 of the measurement etc. will be pointed out.

Degradation of the energy resolution

The measurement presented in subsection 2.3.1 showed a worsening of the energy resolution of the S-LP-LP-MP GEM stack by about 45 %. The simulation of the single S-GEM allowed the conclusion, that a degradation of the energy resolution by 14 % is possible if the local gain variation of a foil is increased by the presence of holes with different hole geometries. One can see that the variation of the hole diameter of the last GEM alone cannot explain the monitored degradation. As visible in the SEM images shown in the appendix in Figure C.1, also the third GEM of the stack showed a remarkable change of the hole geometry. If one assumes that a change of the hole diameter, even though in a smaller extent, was also present in GEM2 and maybe even in GEM1 one can qualitatively explain the degradation of 45 %. A quantitative extrapolation of the simulation to the measurement with the S-LP-LP-MP stack is not possible due to different pitches of the GEMs, different transfer fields and GEM voltages as well as a different or, for GEM1 and GEM2, unknown amount of etching.

Gain performance of the GEM detector

In the measurement presented in subsection 2.3.1 no systematic changes of the gain, neither of the quadruple nor of the triple GEM stack, was observed. However the simulation showed, that the presence of holes with different inner diameters within a S-GEM foil leads to an increase of the detector gain by 9 %. Since also GEM3 in the measurement was affected by a reduction of the hole diameters and probably also GEM2 and GEM1, one would expect an even higher increase than 9 %.

One explanation can be given by the observed rings on the electrodes of the GEM. A comparison between the SEM image of GEM4 and the simulation can be seen in Figure 4.1. The rings in the measurements were observed on a MP-GEM foil at a distance of 30 µm to the edge of the copper electrode. In the figure, these rings are highlighted in red. In Figure 4.1 (b) the distribution of ions on the top electrode of the simulated S-GEM with an inner hole diameter of 90 µm is shown. In there also rings at 30 µm distance to the electrode edge were drawn. One can see that the drawn red rings enclose the region around the holes, where the ions end up. Outside of these rings, the number of ions is close to zero.

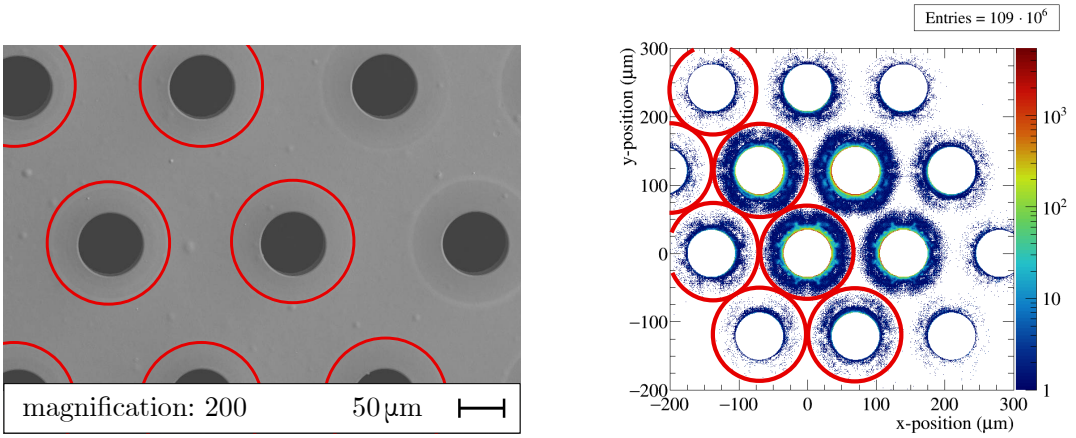

(a) Image of the irradiated area of GEM4 Top made with SEs (MP-GEM).

(b) Distribution of simulated ion endpoints on the top electrode (S-GEM). Inner hole diameter: 90 µm.

Figure 4.1: Comparison of the top electrode between measurement and simulation. Some rings at 30 µm distance to the electrode edge are highlighted in red.

If the kapton between the GEM electrodes is removed by the plasma of the avalanche it can also be taken away by the electric charges created in the amplification process. If parts of the kapton is taken away by the ions, these impurities will also end up on the electrodes. Therefore one can assume, that the rings shown in Figure 4.1 (a) are not rings, but a thin layer of depositions on the electrode. This layer extends from the edge of the electrode to a distance of 30 µm.

These depositions will of course also affect the electric field, which is produced by the electrodes. If (parts of) the electrodes are covered with insulating deposits, they will charge up and produce an opposite electric field. Therefore the electric field inside the GEM hole will be lowered. Since this effect was not taken into account in the simulations, it could give the missing link between the stable gain observed in the measurements and the increasing gain figured out

by the simulations. If the gain is lowered by the layer of deposits on the electrode and increased by the larger inner hole diameter, the resulting gain could be constant.

4.1.2 Measurements made by the RD51 Collaboration

After the problem of etching in GEMs came up, the RD51 Collaboration started a project for the "CERN Summer Student Programme". Within this project, the etching phenomenon in GEMs was studied by D. Zavazieva. The measurements and results are reported in her bachelor thesis in [34], which will be used for comparison.

The measurements were performed with a triple GEM detector and a X-ray generator, which allowed to produce a large primary ionization. With a gain of about 10 000, a dose up to 7000 mC/cm^2 could be accumulated in different Ar-CO_2 gas mixtures. Afterwards SEM images with SEs as well as cross sections of irradiated holes could be made using a FIB.

The measurement of the energy resolution was performed in Ar-CO_2 (70-30) and could reproduce the degradation of the energy resolution. In addition, the removal of the kapton in the affected area of the mostly irradiated GEM as well as the rings on the electrodes of this GEM were visible under the SEM.

The gain was measured in different CO_2 concentrations. With 10 % and 20 % of CO_2, no change of the gain was monitored up to 3000 mC/cm^2, followed by a systematic decrease. An increase of the gain from the beginning of the measurement was monitored with 30 % of CO_2, followed by a decrease, even below the start level. In addition, the dependence of the H_2O concentration of the gas on the detector gain was studied in Ar-CO_2 (70-30), but no clear conclusion could be drawn.

The comparison with the measurements presented in this work shows, that the etching effect of GEMs can be reproduced. In addition, the measurements presented in [34] also showed that no change of the detector performance of the triple GEM stack, operated at a gain of 10 000 in Ar-CO_2 (70-30), within the projected lifetime of the upgraded TPC occurred.

4.1.3 Conclusions concerning the etching phenomenon

The observed phenomenon of etching in GEMs affects mainly the energy resolution of the detector. In the last years, the ALICE TPC Upgrade Collaboration gained a lot of experiences in optimizing a quadruple GEM stack to a good IBF and a satisfying energy resolution. These studies showed, that the quality of the energy resolution is mainly driven by the ability of the detector to preserve as much of the statistics of primary electrons as possible. Therefore the drift field E_{D}, the first GEM and the first transfer field E_{T1} played a leading role in optimizing the energy resolution. The effect of etching however showed, that the quality of the energy resolution does also depend on the gain uniformity of the individual GEMs in the stack. Contrary to the first argument, the dependence the energy resolution on the etching should depend on the gain of the individual GEMs, and therefore be strong in GEM4.

However, the trigger of the etching effect remains not completely understood. The measurements presented in this work suggest an extremely high gain of the detector as crucial for etching. In addition to the high gain, the H_2O concentration of the gas was studied by scientists of the RD51 Collaboration. Furthermore the question can be asked, if there is a difference between a rate-dependent and a gain-dependent effect. At a high gain and low rate one gets a large multiplication in the GEM and therefore a large plasma. A low gain and high rate, however, transports more electrons through the GEM holes and results therefore in a lower multiplication

or rather smaller plasma.

Since the upgraded TPC will accumulate a dose of (only) about 121 mC/cm^2 and will be operated at a much lower gain, the occurrence of etching can be excluded for the GEM-based TPC.

4.2 CO_2- and CH_4-induced ageing in GEMs

A comparison of the relative anode current and energy resolution of the Ar-CO_2 (70-30) and Ar-CH_4 (95-5) measurements is shown in Figure 4.2 (a) and (b) respectively. For the Ar-CH_4 measurement only the part presented in section 2.4 is shown, because the energy resolution is comparable to the Ar-CO_2 measurement.

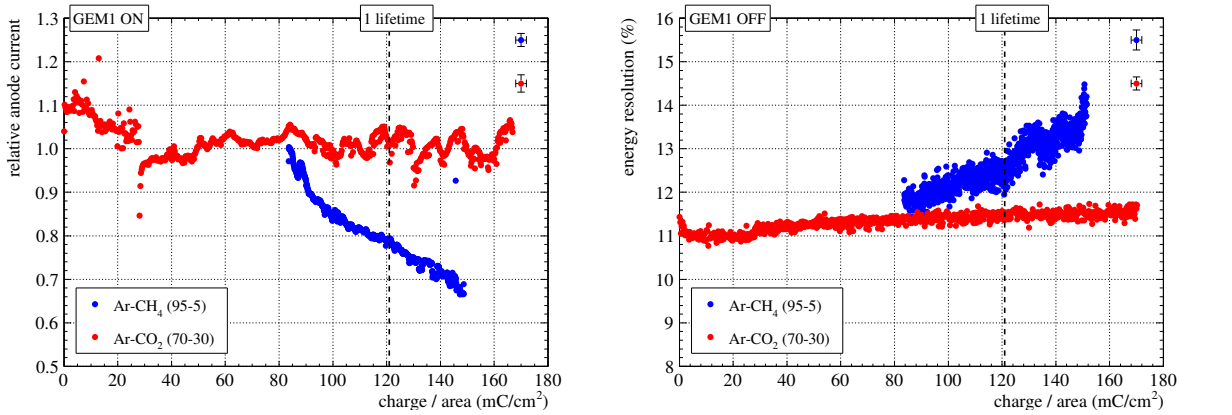

(a) Corrected anode current.

(b) Energy resolution extracted from the calibrated pulse-height spectra.

Figure 4.2: Comparison of the ageing measurements performed in Ar-CH_4 (95-5) and Ar-CO_2 (70-30).

One can see that the gain and the energy resolution in the Ar-CH_4 measurement changes dramatically compared to the Ar-CO_2 run. Even though the gain in the CO_2-based gas mixture shows some fluctuations, no systematic decrease is visible. The small variations are most probably not related to the quench gas used.

The observed degradation of the energy resolution by about 2 % would be higher in an experiment like ALICE. Trying to keep the same gain, one would compensate the gain loss by an increase of the GEM3 and GEM4 voltages. This would accelerate the ageing and lead to an even faster degradation of the energy resolution. Therefore methane as quench gas should be avoided in high rate experiments like ALICE.

The results of the CO_2-induced GEM ageing are comparable to the measurements presented in [21]. In there a triple GEM detector was operated at a gain of 8500 in Ar-CO_2 (70-30). After 700 mC/cm^2 no change of gain or energy resolution was monitored. Even though the energy resolution was at the beginning of the measurement only 19 %, which results in a low sensitivity, a CO_2-induced ageing can be excluded.

4.3 CH_4-induced ageing in proportional counters and GEMs

Due to the different geometries of wires and GEMs, there are some difficulties by trying to compare the ageing of these two technologies. As explained in section 1.2, the electron amplification in wire chambers is propagating towards the electrode, whereas the electron avalanche in GEMs is propagating through the holes of the foils. In addition, the amplification process in GEMs is split between several GEMs, whereas in MWPCs only one layer of wires is needed to achieve a satisfying operation. Nevertheless a comparison is reasonable since GEM stacks are often discussed as alternatives to MWPCs.

4.3.1 The ageing rate *R'*

To compare wire ageing and the possible impact on the detector using different wire materials, gas mixtures including variations of the water content of the gas, the so called "ageing rate" was introduced. This allowed to quantify the observed loss of gain in a single number and simplified a comparison. To determine the ageing rate R', a phenomenological parametrization for the relative gain G_r as a function of the accumulated charge per length Q/L was introduced in [35] and is shown in Equation 4.1.

$$G_\mathrm{r} = a \cdot \exp\left(-R' \cdot \sqrt{Q/L}\right) \quad \text{with} \quad a \approx 1 \tag{4.1}$$

The effect of different ageing rates can be seen in Figure 4.3. In there, gain drops were computed, assuming different values of R'. One can see that for the different gain drops, the value of the ageing rate varies over three orders of magnitude.

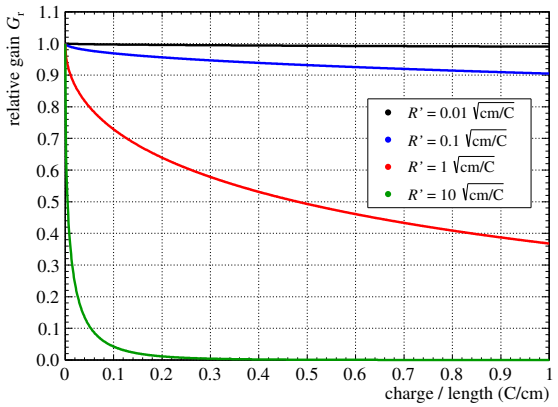

Figure 4.3: Computed gain drop for different R', adapted from [35, p. 116].

This parametrization will now also be used to quantify the observed ageing in GEMs in the Ar-CH_4 measurements. The extracted ageing rates can than be compared to ageing rates published in [35], which were measured using a single-wire proportional counter. Since the accumulated charge of the GEM measurements was normalized to the irradiated area, one had to convert it into accumulated charge per length.

4.3.2 Converting accumulated charge per area into charge per length

Since the ageing rates published in [35] were measured using a single-wire proportional counter, the comparison will first focus on GEMs and single wires. In Figure 4.4 (a) one can see a

schematic top view of the irradiated area on a GEM. In Figure 4.4 (d), the side view of a GEM, irradiated by X-rays, is shown. It is clear, that all the created charge in the gas volume will be transported towards the GEM, as indicated in the drawing by the electric field lines. To be more precise, the ageing in GEMs depends on the amount of charge which enters the holes and participates in the amplification process. Therefore the ageing depends on the electron collection efficiency and the multiplication of the GEM foil, but not on the gain. In the experimental setup, the current was read out by the anode beneath the last GEM. In this way only the charge which could be extracted out of the last GEM was taken into account. Since the parametrization if fitted to the relative gain, this problem should not play a leading role. Also the size of the irradiated area of the GEMs and the anode should be the same, since the diffusion of the electrons in the small gaps should be quite low.

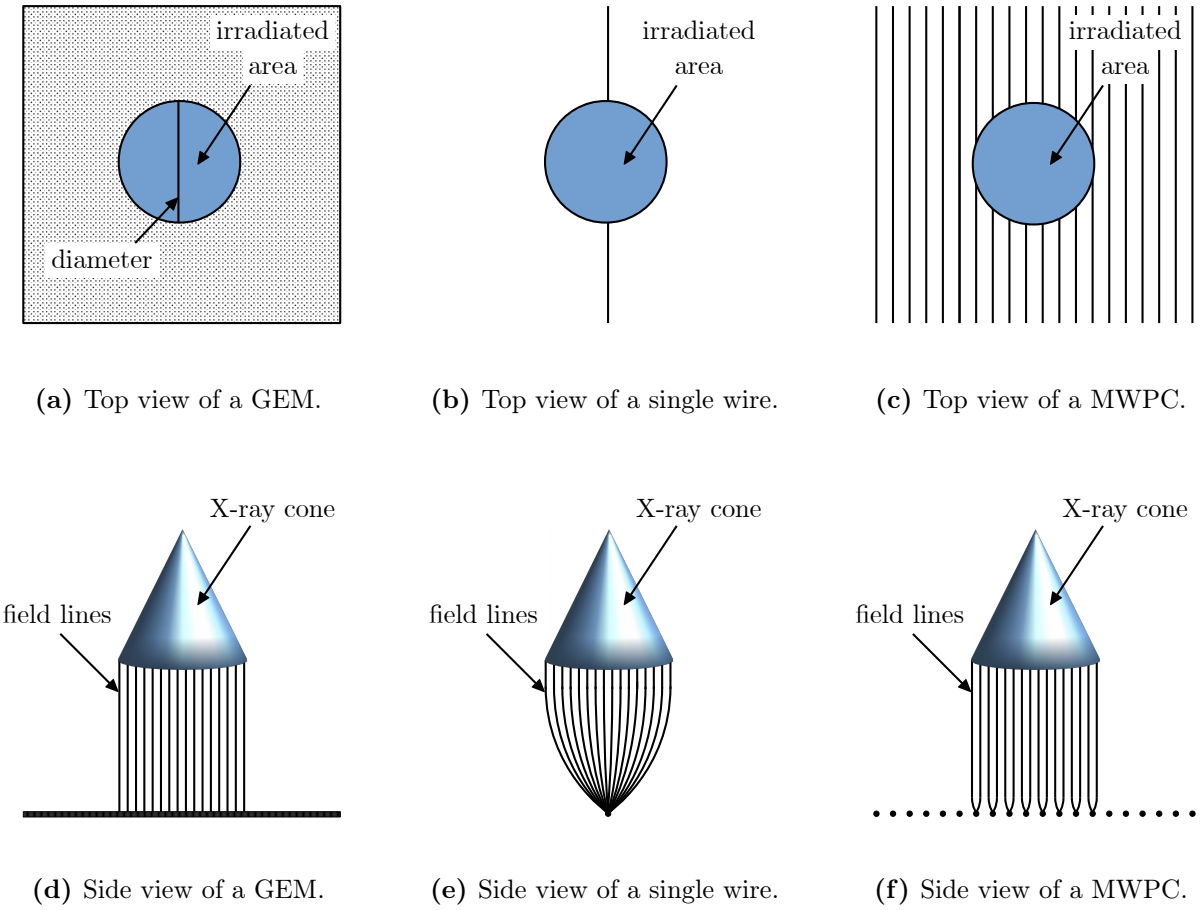

(a) Top view of a GEM. **(b)** Top view of a single wire. **(c)** Top view of a MWPC.

(d) Side view of a GEM. **(e)** Side view of a single wire. **(f)** Side view of a MWPC.

Figure 4.4: Schematic drawing of the irradiated areas in different detector technologies.

To compare it to the irradiation of a single wire, one has to understand its operation principle. The top view and side view of a single-wire proportional counter is drawn in Figure 4.4 (b) and (e) respectively. One can see that the irradiated area is much larger than the single wire. Nevertheless all the created charge is accumulated on the electrode, because the wire is the only anode in the system. The schematic in Figure 4.4 (e) shows that all the field lines or rather electrons end up on the electrode.

Since one can assume that in both cases, GEM detector and single-wire proportional counter,

all the created charge is accumulated, it is just a question of how to normalize the accumulated charge. To convert the measurements carried out with GEMs, one can normalize the accumulated charge to the diameter of the irradiated area instead of the area itself, as indicated in Figure 4.4 (a). In this way a comparison between the GEM measurements and single-wire proportional counters becomes possible.

A comparison between GEMs and MWPCs is somehow more difficult. As one can see in Figure 4.4 (c), the irradiated area extends over a range of wires in a MWPC. Therefore the individual wires accumulate much less charge as it is shown in Figure 4.4 (f). The exact dose depends on the pitch of the wires.

First a conversion of the gain drops measured using the GEM detector will be made. By fitting the parametrization to the relative gains, the ageing rates will be extracted. These rates can than be compared first with ageing rates of single-wire proportional counters presented in [35]. Afterwards a qualitative comparison will be carried out with the MWPCs of the ALICE TPC.

4.3.3 Gain drops of the GEM measurements performed in Ar-CH_4

The relative gain drop of the measurements in Ar-CH_4 can be seen in Figure 4.5, plotted as a function of accumulated charge per length. The measurement in Figure 4.5 (a) is a combination

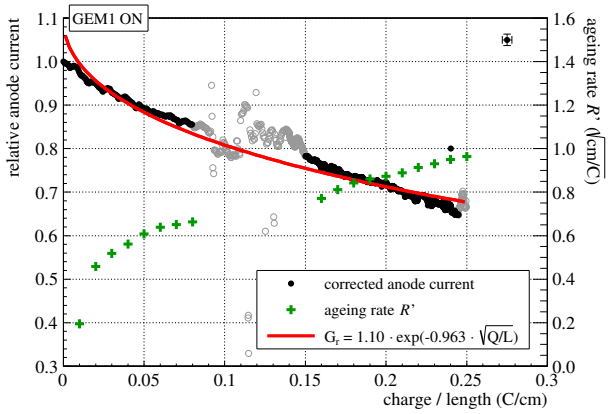

(a) Combination of the measurements presented in section D.1 and section 2.4.

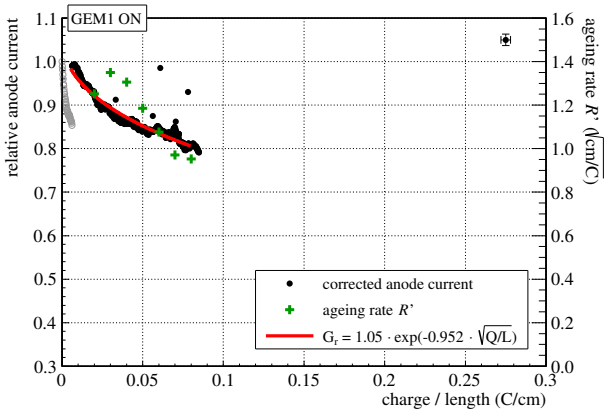

(b) Measurement presented in section D.2.

Figure 4.5: Fitted gain drop of the measurements in Ar-CH_4 (95-5).

of the measurement presented in section D.1 and section 2.4. For both measurements the same GEM4 was used. If one assumes, that the measured gain drop is mainly caused by the ageing of the last GEM, one can combine these two runs. The second part was shifted to the corresponding relative gain, so that it fits the first part of the measurement. In Figure 4.5 (b) the measurement presented in section D.2 is shown. Both measurements are fitted with the parametrization shown in Equation 4.1. For the fits, the gray data points were excluded. In Figure 4.5 (a) these points correspond to some not understood fluctuations during the measurements, as well as the increasing gain due to the empty gas bottle at the end of the run. In Figure 4.5 (b) the first part was excluded, because the stack of complete new GEMs showed a strange behavior within the first two days of operation. The rest of the measurement was shifted up by 16 % to start at a relative gain of 1.0.

In both plots the ageing rates are plotted using green markers. According to [35], R' should tend towards a constant value, what is only true for Figure 4.5 (a). The excluded data points in Figure 4.5 (b) at the beginning of the measurement did most probably influence the parametrization. Nevertheless one gets two final ageing rates from the fits of these two measurements, which are given in the legends of the plots. These values will now be compared to ageing rates of proportional counters in the following subsection.

4.3.4 Comparison of proportional counters and GEMs

Since the values for R' in [35] are plotted as a function of the initial intensity (nA/cm), the accumulated charge per length had to be divided by the time the detector was operated. In this way, the gain of the detector is also taken into account. Figure 4.6 shows ageing rates as a function of the initial intensity, measured in different single-wire proportional counters together with the two GEM rates calculated in the previous subsection. The red points in the figure were taken from [35] and were measured using a single-wire proportional counter operated in Ar-CH_4 (90-10). For these measurements different wire materials for the anode as well as for the cathode were used. In addition the impact of the H_2O concentration in the gas on the detector performance was studied. The blue points were calculated from the measurements presented in [36] using a single-wire proportional counter in Ar-CH_4 (80-20). In the paper another parametrization was used, but the authors provided refitted results of their measurements using Equation 4.1.

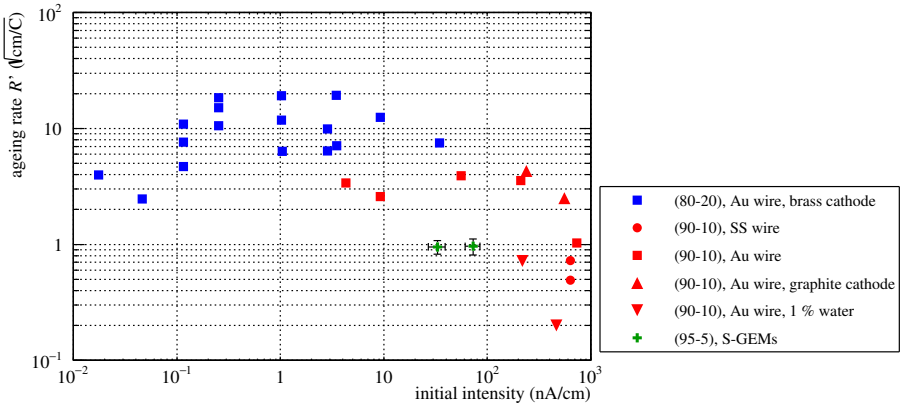

Figure 4.6: Comparison of R' in Ar-CH_4 mixtures, red points from [35], blue points from [36].

One can compare now the two ageing rates of the S-GEMs plotted with green markers with the rates of the single-wire proportional counters. As expected from the gain drops in the measurements, the ageing rates of GEMs are not negligible. Nevertheless the ageing rates of the single-wire proportional counters are higher. This could be produced by the higher content of CH_4 as well as by the different geometry of the wires. Since the amplification in wire chambers is propagating towards the wires, the hydrocarbons are produced close to the electrodes. In addition a much smaller surface is covered with deposits.

To compare ageing in GEMs and MWPCs one has to take into account the pitch of the wires, because the created charge will split on all wires within the irradiated area as shown in Figure 4.4 (f). The larger the pitch, the higher the charge on individual wires in the chamber. To compare the GEM ageing rate at 72.77 nA/cm with the ALICE MWPCs, one has to compare it to the

initial density of the wires which is 2.85 nA/cm. This can be calculated by dividing the initial intensity by the mean number of anode wires of the ALICE ROCs. The anode wire pitch of the ALICE ROCs is 2.5 mm [15, p. 45], resulting in 25.5 wires within an irradiated area (circle) of $1\,cm^2$. One can see that the ageing rates at 2.85 nA/cm are even higher than at 72.77 nA/cm.

CH_4-induced ageing in a GEM stack is significant even though it might be lower than in single-wire proportional counters and/or MWPCs. It should be avoided in detectors exposed to relatively high irradiation doses, such as detectors used in the LHC experiments.

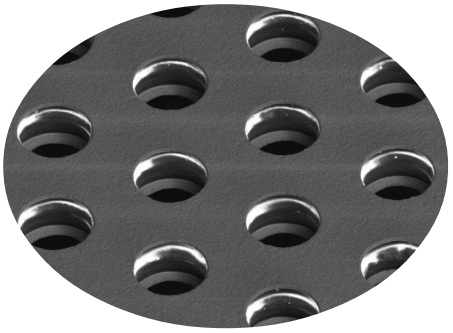

Chapter 5

Summary

In the context of the Upgrade of the ALICE TPC with quadruple stacks of GEMs for RUN 3 of the LHC, a test setup was built to do so called "ageing tests". These long-term measurements with quadruple stacks of GEMs were carried out in Ar-CO_2 and Ne-CO_2-N_2 gas mixtures to study the performance of GEM stacks under high irradiation. The detector was operated at high gains to accelerate possible ageing effects and to accumulate more than 121 mC/cm^2, which is the equivalent dose of 10 years upgraded TPC operation.

Outgassing tests with four different components used for the assembly process of the GEM-based TPC were performed. No negative impact on the detector performance with the frames, screws and resistor soldering was observed. From the tests with the epoxy adhesive no certain conclusions could be drawn.

A new phenomenon, the so called "etching effect" was observed in GEMs during the operation of the quadruple GEM stack. Together with simulations carried out with the Garfield^{++} toolkit, a basic explanation of this effect could be given. Due to the operation at extremely high gains, the kapton layer between the GEM electrodes is removed. This leads to a degradation of the energy resolution, because of an increase of the local gain variations. Since this effect was observed at doses far above the projected lifetime of the upgraded TPC, it is not expected to occur during the operation of the GEM-based TPC.

In addition, ageing tests in Ar-CH_4 (95-5) were performed and compared to CH_4-induced ageing processes in wire chambers. Just like in these types of detectors, insulating deposits on the electrodes were observed, as well as a resulting loss of gain and a degradation of the energy resolution. The extracted ageing rates of the GEM measurements were compared to ageing rates of single-wire proportional counters for the same dose. It was found that CH_4-induced ageing in GEMs is lower than in wire chambers, however *not* negligible.

Acknowledgments

First I want to thank my professor Harald Appelshäuser, because he gave me the opportunity to participate in this project as well as to live, work and study half a year at CERN. Special thanks I would like to express to the TPC group at CERN, especially to my supervisor Chilo Garabatos and to my colleague Renato Negrão. Without their expertise and support this project would not have been possible. Particularly debugging the detector whenever it was not possible for me to come to CERN due to university duties, was a great help. Danilo Vranić I want to mention and thank for his help at the beginning of the project.

I also highly appreciate the support of the RD51 Collaboration, especially Eraldo Oliveri, because he was always willing to help me out with a variety of problems. Ana Teresa Pérez Fontenla I want to thank for making an enormous amount of SEM images, which opened the possibility for a better understanding of the ageing and etching effects in GEMs.

In addition, I would like to thank the complete High Energy Group in Frankfurt for their support. Especially I want to mention Ernst Hellbär for his help with the Garfield^{++} simulations. Rainer Renfordt I want to thank for proofreading this thesis as well as Christoph Blume for offering himself as second referee. Fabian Liebske was always a great partner in discussing physical problems and the consequent insights in physics had been very enriching.

Last but not least I want to thank my parents Christine and Jürgen Jung for their support and patience during my complete studies of physics.

Appendices

Appendix A

Number of produced electrons per 5.89 keV X-ray

The number of primary electrons N_e, which are ejected per 5.89 keV X-ray, could be calculated using the effective ionization potential W_m of the gas mixtures. It is the mean energy for ion-electron pair production. The effective ionization potential is not equal to the ionization potential, since some energy is also lost to excitation. [29, p. 131]

To calculate W_m, the effective ionization potentials W of the individual constituents of the gas mixtures listed in Table A.1 were used. In the reference no errors for the values were given.

Gas	W (eV)
Ar	26
Ne	36
CO_2	33
CH_4	28
N_2	35

Table A.1: Effective ionization potential W for the individual gases of the mixtures [29, p. 131].

The effective ionization potential W_m of the gas mixtures could be calculated by adding up W of all constituents, weighted with their number fraction. This is the number of particles of a constituent, divided by the total number of particles in the mixture. The amount of different gases in gas mixtures is usually given in volume fraction ϕ, meaning that 70 % of the volume of the gas mixture Ar-CO_2 (70-30) is taken up by argon. For ideal gases however these two fractions are equal, because the gas is treated as a composition of point-like particles. Therefore ϕ could be used for weighting, as shown in Equation A.1.

$$W_m = \sum_i \phi_i \cdot W_i \tag{A.1}$$

Now the number of electrons per X-ray could be calculated by dividing the energy of the ^{55}Fe X-ray by the effective ionization potential of the gas mixture, as one can see in Equation A.2. Only the 5.89 keV X-rays of ^{55}Fe were taken into account, since it is the decay channel with the highest probability.

$$N_e = \frac{5890\,\text{eV}}{W_m} \tag{A.2}$$

The calculated numbers were rounded down to integers. The effective ionization potential and the number of electrons per X-ray for the three gas mixtures used in the ageing tests are listed in Table A.2.

Gas composition	Mixing ratio	W_{m} (eV)	N_{e}
Ar-CO_2	70-30	28.1	209
Ar-CH_4	95-5	26.1	225
Ne-CO_2-N_2	85.7-9.5-4.8	35.7	164

Table A.2: Effective ionization potential W_{m} and number of electrons N_{e} per 5.89 keV X-ray for the gas mixtures.

Appendix B

Determination of the irradiated areas

The size of the irradiated area is given by the charge distribution on the anode. The width of this distribution depends on the distance of the produced primary electrons in the drift volume to the ^{55}Fe source. Primary charge produced close to the source will generate a narrow charge distribution on the anode. A wide distribution is created by primary charge which is produced close to the first GEM. This distinction comes from the X-ray distribution in the drift volume, which widens with increasing distance to the source, depending on the cone of the X-rays. In addition the number of X-rays decreases exponentially, depending on the mean free path of 5.89 keV X-rays in the respective gas mixtures. Therefore primary electrons produced close to the cathode have a much stronger impact on the charge distribution on the anode, than electrons produced close to GEM1.

One possibility to calculate the distribution on the anode, is to add X-ray distributions for different distances between source and interaction point of the X-rays in the gas. Therefore one needs the profile of the ^{55}Fe source to know the cone of the X-rays as well as their mean free paths. The measurement of the profile will be explained in section B.1. Afterwards the calculation of the mean free paths of 5.89 keV X-rays in the individual gas mixtures will be shown in section B.2. Finally the calculation of the irradiated areas will be presented in section B.3.

B.1 Measurement of the profile of the ^{55}Fe source

To measure the profile of the radioactive source a small triple GEM detector was used. A schematic view of the experimental setup can be seen in Figure B.1. The detector had a small drift volume of about 3 mm height and an anode made of x- and y-wires. On the top side of the detector was a plastic window, which occupied the entire surface. The source was put outside the detector at different distances d between its bottom side and the active volume of the detector, taken into account the 1.8 cm gap between window and cathode. The uncertainties of the measured distances were estimated to be 0.2 cm.

Since the measured distributions on the anode do only depend on the geometrical profile of the source, the properties of the gas mixture in the 3 mm gap do not play any role for the measurements.

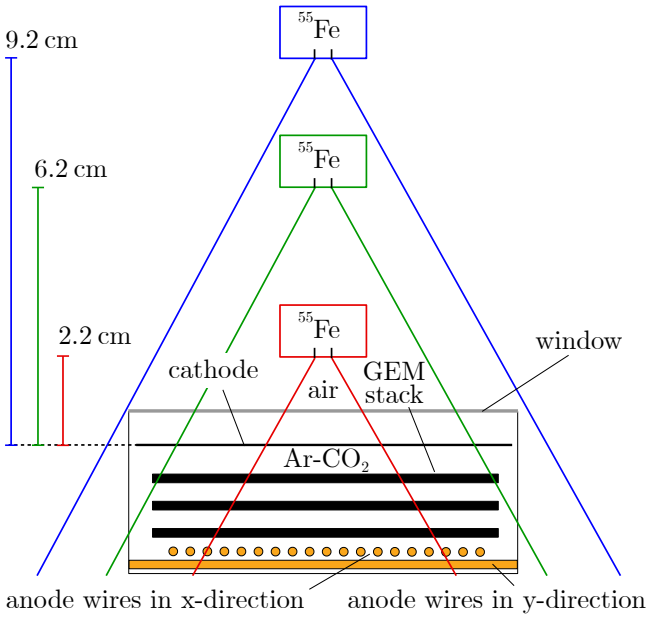

Figure B.1: Schematic drawing of the triple GEM detector used to measure the source profile.

Afterwards the X-ray distribution on the two wire planes was measured and plotted for the x- and y-wires independently as shown in Figure B.2. Since the x-wire plane was placed above the y-wires, the X-ray distributions on the x-wires have more entries. One can now easily see how the different distributions depend on the distance between the active volume of the detector and the source by comparing Figure B.1 and Figure B.2.

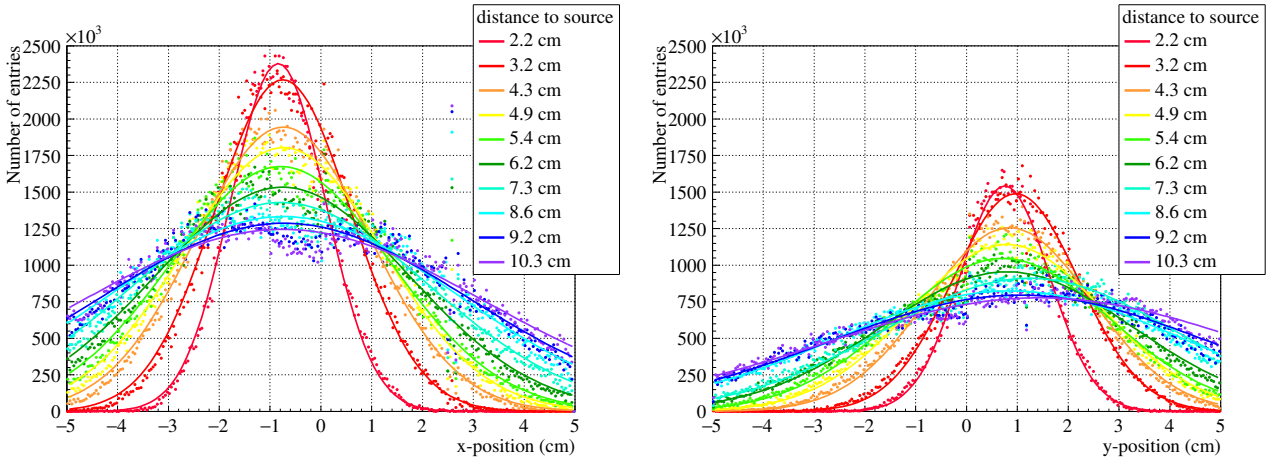

(a) X-projection.

(b) Y-projection.

Figure B.2: Projections of the measured X-ray distributions.

The X-ray distributions were fitted and the standard deviation σ of every distribution was extracted. For each distance, the arithmetic mean of the standard deviations was calculated and plotted versus the distance in Figure B.3. The errors of the mean values were calculated by error propagation from the errors of the individual X-ray distributions of the x- and y-wire plane.

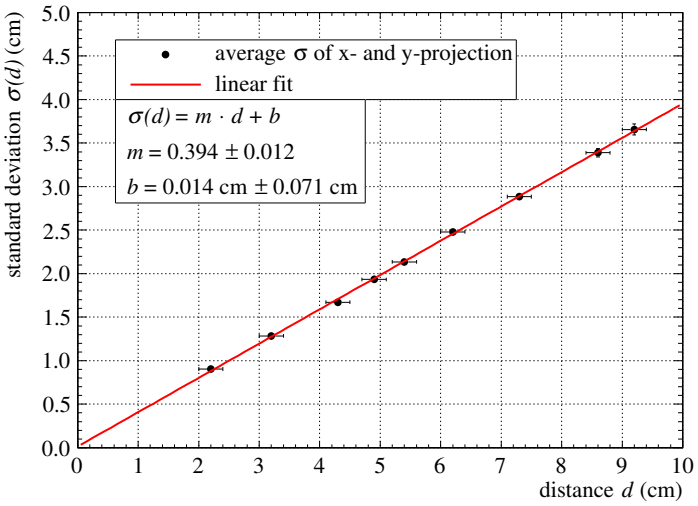

Figure B.3: Standard deviation of the X-ray distributions as a function of the distance.

With the slope of the fit in Figure B.3, one knows the cone of the X-rays for this specific radioactive source. It can later be used to calculate the widths of X-ray distributions for any distance between source and interaction point of the X-rays in the gas.

B.2 Mean free paths of 5.89 keV X-rays in gas mixtures

To calculate the mean free path λ of 5.89 keV X-rays in a gas mixture, one has to know its mass attenuation coefficient μ/ρ for the corresponding energy. Together with the density ρ of the gas mixture, the attenuation coefficient μ can be calculated. The reciprocal of μ gives the mean free path of the X-rays.

The calculation of the mass attenuation coefficients for the three gas mixtures was carried out by adding up the coefficients of the respective constituents. These were calculated for 5.89 keV X-rays using the database search form of the XCOM software provided by the National Institute of Standards and Technology. The values are listed in Table B.1. In the database, no errors were given for μ/ρ.

Constituent	$\mu/\rho\,(\mathrm{cm}^2/\mathrm{g})$	$M\,(\mathrm{g/mol})$	$\rho \cdot 10^{-3}\,(\mathrm{g/cm}^3)$
Ar	272.600	39.948	1.623
Ne	57.760	20.180	0.820
CO_2	24.450	44.010	1.788
CH_4	8.774	16.040	0.652
N_2	19.130	28.013	1.138

Table B.1: Mass attenuation coefficients μ/ρ for 5.89 keV X-rays [37], molar masses M [38] and densities ρ calculated at a temperature of 300 K and a pressure of 1 atm for the constituents of the gas mixtures.

For the summation, the mass attenuation coefficients of the individual gases had to be weighted with the fraction by weight w_i of the i^{th} constituent of the gas mixture. Since the

ratios of gas mixtures are given in volume fraction ϕ, the weights had to be converted. The conversion was done with Equation B.2, starting with the definition of the mass fraction and using the definition of the volume fraction in Equation B.1.

$$\phi_\mathrm{i} = \frac{V_\mathrm{i}}{\sum_\mathrm{z} V_\mathrm{z}} \qquad \Leftrightarrow \qquad V_\mathrm{i} = \phi_\mathrm{i} \cdot \sum_\mathrm{z} V_\mathrm{z} \tag{B.1}$$

$$w_\mathrm{i} = \frac{m_\mathrm{i}}{\sum_\mathrm{z} m_\mathrm{z}} = \frac{\rho_\mathrm{i} \cdot V_\mathrm{i}}{\sum_\mathrm{z} \rho_\mathrm{z} \cdot V_\mathrm{z}} \overset{\text{B.1}}{=} \frac{\rho_\mathrm{i} \cdot (\phi_\mathrm{i} \cdot \sum_\mathrm{a} V_\mathrm{a})}{\sum_\mathrm{z} \rho_\mathrm{z} \cdot (\phi_\mathrm{z} \cdot \sum_\mathrm{a} V_\mathrm{a})} = \frac{(\rho_\mathrm{i} \cdot \phi_\mathrm{i}) \cdot \cancel{(\sum_\mathrm{a} V_\mathrm{a})}}{(\sum_\mathrm{z} \rho_\mathrm{z} \cdot \phi_\mathrm{z}) \cdot \cancel{(\sum_\mathrm{a} V_\mathrm{a})}} = \frac{\rho_\mathrm{i} \cdot \phi_\mathrm{i}}{\sum_\mathrm{z} \rho_\mathrm{z} \cdot \phi_z} \tag{B.2}$$

Now the mass fractions of the constituents could be calculated, using their densities given in Table B.1 and their volume fractions. The densities listed in Table B.1 were calculated assuming an ideal gas at a temperature of 300 K and a pressure of 1 atm, using the molar masses M listed in the same table. The errors of the molar masses play no role within the three significant digits used for these calculations. The resulting mass fractions are listed in Table B.2, together with the volume fractions for comparison.

Gas mixture	Ratio weighted to ϕ (%)	Ratio weighted to w (%)
Ar-CO_2	70.00 - 30.00	67.93 - 32.07
Ar-CH_4	95.00 - 5.00	97.93 - 2.07
Ne-CO_2-N_2	85.70 - 9.50 - 4.80	75.79 - 18.32 - 5.89

Table B.2: Volume fraction ϕ and mass fraction w of the constituents.

Finally the mass attenuation coefficients of the gas mixtures were calculated using Equation B.3. [39]

$$(\mu/\rho) = \sum_\mathrm{i} w_\mathrm{i} \cdot (\mu/\rho)_\mathrm{i} \tag{B.3}$$

As mentioned above, the densities of the gas mixtures were also needed to calculate the attenuation coefficients. Therefore the densities of the individual constituents of the gas mixtures were added using Equation B.4.

$$\rho = \frac{m}{\sum_\mathrm{i} V_\mathrm{i}} = \frac{m}{\sum_\mathrm{i} \frac{m_\mathrm{i}}{\rho_\mathrm{i}}} = \frac{1}{\sum_\mathrm{i} \frac{m_\mathrm{i}}{m} \frac{1}{\rho_\mathrm{i}}} = \frac{1}{\sum_\mathrm{i} \frac{w_\mathrm{i}}{\rho_\mathrm{i}}} = \left(\sum_\mathrm{i} \frac{w_\mathrm{i}}{\rho_\mathrm{i}} \right)^{-1} \tag{B.4}$$

A list of all mass attenuation coefficients and densities for the gas mixtures is given in Table B.3. The listed attenuation coefficients were calculated by multiplying the mass attenuation coefficients with the corresponding gas density. In addition the mean free paths were calculated by the reciprocals of the attenuation coefficients.

Gas mixture	Mixing ratio	$\mu/\rho\,(\mathrm{cm}^2/\mathrm{g})$	$\rho \cdot 10^{-3}\,(\mathrm{g/cm}^3)$	$\mu\ (\mathrm{cm}^{-1})$	$\lambda\ (\mathrm{cm})$
Ar-CO_2	70 - 30	193.013	1.672	0.323	3.098
Ar-CH_4	95 - 5	267.140	1.574	0.421	2.378
Ne-CO_2-N_2	90 - 10 - 5	49.381	0.927	0.046	21.846

Table B.3: Mass attenuation coefficients μ/ρ, densities ρ, attenuation coefficients μ and mean free paths λ for the three gas mixtures used in the ageing tests.

The attenuation of 5.89 keV X-rays in the three different gas mixtures is shown in Figure B.4. One can see the difference between the argon- and neon-based gas mixtures. Due to the low mass attenuation coefficient of neon, the attenuation of X-rays in Ne-CO_2-N_2 is much lower than in the argon-based mixtures.

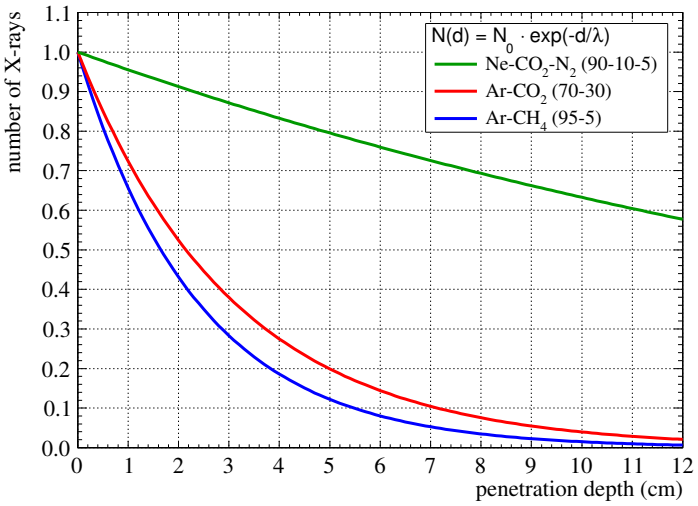

Figure B.4: Attenuation of 5.89 keV X-rays in the different gas mixtures.

B.3 Calculation of the irradiated areas

To calculate the irradiated area in the experimental setup, Gaussians were calculated in steps of 1 mm between cathode and GEM1. The distance between the bottom side of the source and the active volume of the detector was measured to be 1.3 cm. The widths and amplitudes of the Gaussians were calculated using the fit in Figure B.3 and the mean free paths listed in Table B.3 respectively. The distributions were added up to get a final Gaussian G_f as one can see in Equation B.5. This procedure was performed for all three gas mixtures.

$$G_\mathrm{f} = \sum_{d=1.3}^{11.3} \frac{1}{2 \cdot \pi \cdot \sigma(d)^2} \cdot \exp\left(-\frac{(x-\mu)^2}{2 \cdot \sigma(d)^2}\right) \cdot \exp(-d/\lambda) \tag{B.5}$$

Finally the Full Width at Half Maximum (FWHM) was extracted and used as the diameter of the irradiated area. The FWHMs and the calculated areas for the gas mixtures are listed in Table B.4. The error of the area was estimated to be 2 %.

Gas mixture	Ratio	FWHM (cm)	Area (cm^2)
Ar-CO_2	70-30	2.7	5.73 ± 0.11
Ar-CH_4	95-5	2.1	3.46 ± 0.07
Ne-CO_2-N_2	90-10-5	4.5	15.90 ± 0.32

Table B.4: Irradiated areas for the different gas mixtures for the field cage with 10 cm height.

Since the height of the field cage is included in the calculation of the irradiated areas, one had to distinguish between the two different field cages used in the setup. A calculation showed, that within the two significant figures, the irradiated areas in the argon-based gas mixtures are equal for the 8 cm and 10 cm field cages. This fact becomes clear if one sees in Figure B.4. The attenuation of X-rays in the argon-based gas mixtures is mainly happening within the first 8 cm. For Ne-CO_2-N_2 the different heights do play a role, but only the 10 cm field cage was used for these measurements.

Appendix C

Additional measurements in Ar-CO_2 (70-30)

C.1 First measurement with empty box, screws and frames

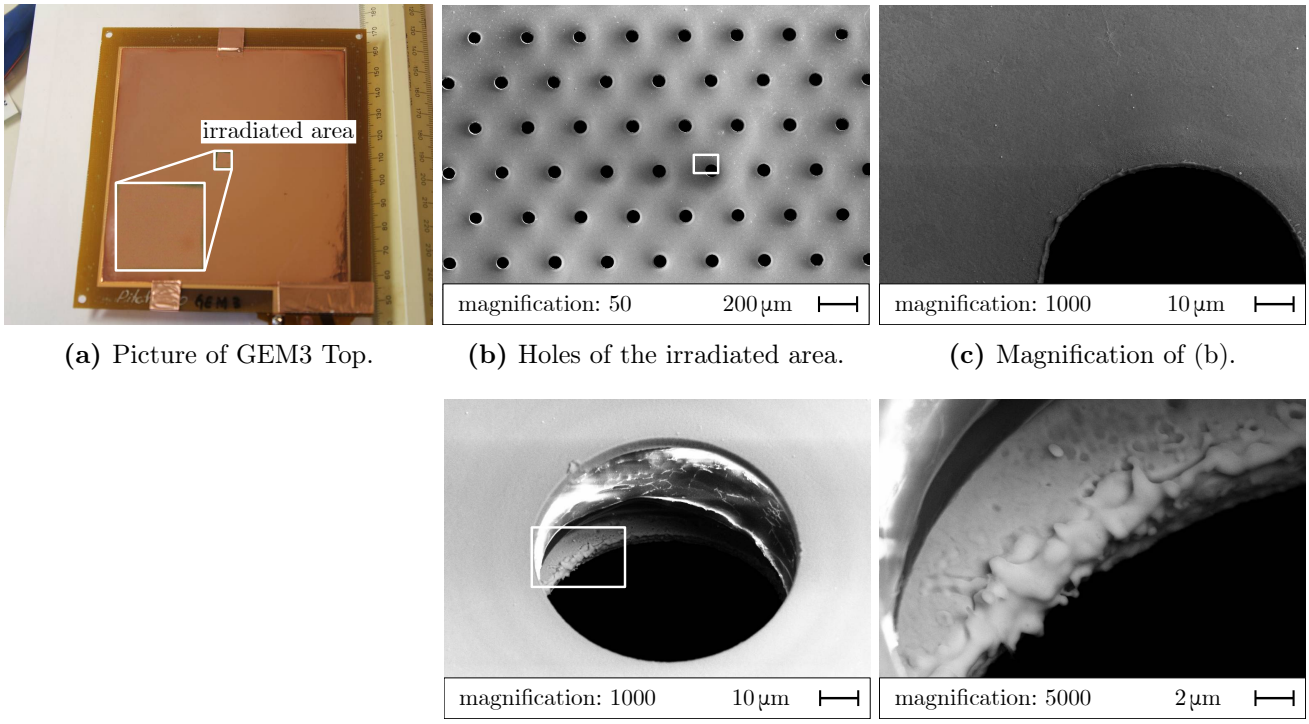

(a) Picture of GEM3 Top.

(b) Holes of the irradiated area.

(c) Magnification of (b).

(d) Single hole of the irradiated area (GEM tilted by 45°).

(e) Magnification of (d).

Figure C.1: Images of GEM3 Top made with a camera and SEM, showing the removal of the kapton layer between the electrodes. Microscopic analysis of GEM3 used in the first measurement testing an empty outgassing box, screws and frames, performed in Ar-CO_2 (70-30). Picture in (a) and SEM images in (c) - (e) adapted from [10, p. 5]. SEM image in (b) provided by A. T. Pérez Fontenla.

Also the irradiated area of GEM3 was analyzed under the SEM as one can see in Figure C.1.

On this GEM, no colorization of the center can be seen, even though the microscopic analysis shows missing kapton in the irradiated area.

In Figure C.3 (e) one can see some solidified splashes of material. If it would be copper that was molten and afterwards re-solidified, a lot of energy would be necessary. This may be an effect of discharges, which would release enough energy to reach temperatures, high enough to melt copper in a small area.

C.2 Second measurement with empty box and frames

The first measurement was repeated in order to see if the removal of the kapton can be reproduced and to confirm that the decrease of the energy resolution was only triggered by the etching and not by the frames in the outgassing box. Therefore a reference run with an empty outgassing box and a measurement testing the frames was performed.

For this run a S-LP-LP-S stack of four completely new GEMs was installed. The gain was tuned to about 40 000 and with a duration of 79 days, about 780 $\mathrm{mC/cm^2}$ were accumulated. With GEM1 OFF the gain was about 13 000 and the rate in E_{T1} about 932 Hz.

The results are shown in Figure C.2. During this measurement the noise level of the system changed very often and abrupt.

This can be seen in the jumps in the peak position as well as in the energy resolution. Leaving aside these noise problems, one can see that the peak position and therefore the gain of the triple GEM system and the energy resolution are quite stable. Only towards the end of the measurement, the energy resolution starts to get worse and also a little slope in the peak position is visible. The two spectra, one taken after 1 projected lifetime and a second taken after 6 projected lifetimes, also show a degradation. The left pulse-height spectrum shows not a good separation of escape and main peak, because the measurement started with an energy resolution of about 18.5 %. But still a deterioration in the second pulse-height spectrum is clearly visible. Only the behavior of the anode remains un-understood. It shows only sometimes a continuous degradation, but also a lot of jumps, otherwise a flat behavior.

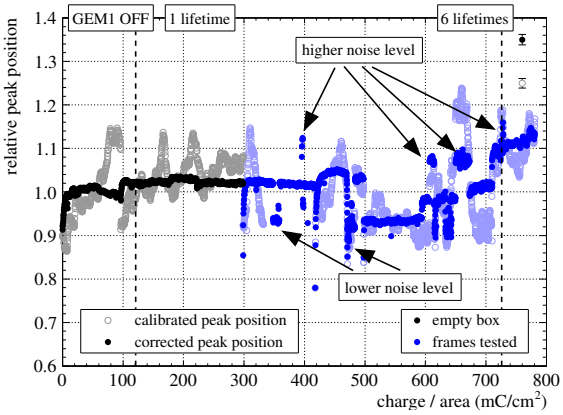

(a) Calibrated and corrected peak position.

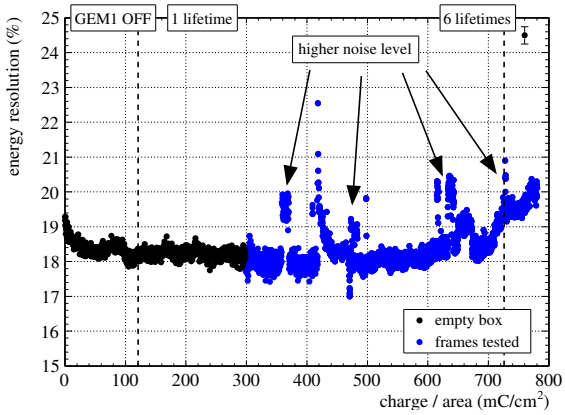

(b) Energy resolution extracted from the calibrated pulse-height spectra.

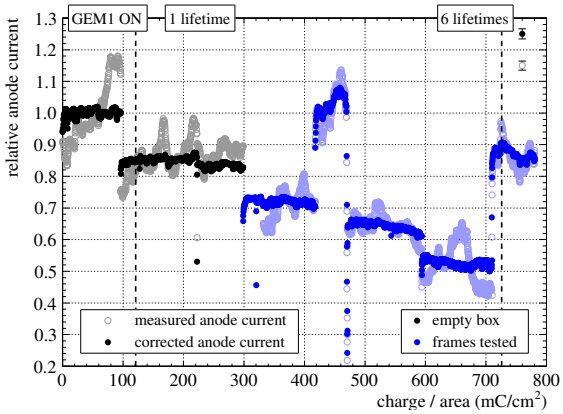

(c) Measured and corrected anode current.

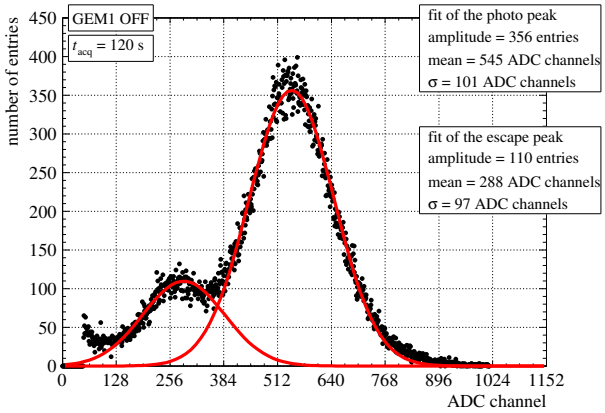

(d) Calibrated and fitted pulse-height spectrum obtained at 121 mC/cm^2 (1 lifetime).

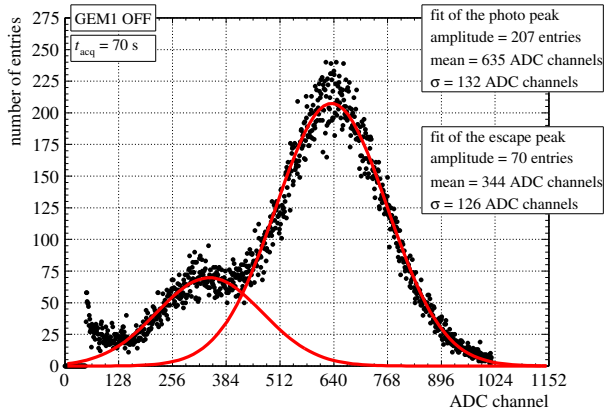

(e) Calibrated and fitted pulse-height spectrum obtained at 726 mC/cm^2 (6 lifetimes).

Figure C.2: Results of the second measurement testing an empty outgassing box and frames, performed in Ar-CO_2 (70-30).

SEM analysis with SEs

In Figure C.3 the microscopic analysis of GEM3 Top after the measurement is shown. In Figure C.3 (a) one can see that no visible effect on the irradiated area occurred. The comparison of the reference area in Figure C.3 (b) and (c) with the images of the irradiated area in Figure C.3 (d) and (e) shows that no change of the kapton diameter was produced.

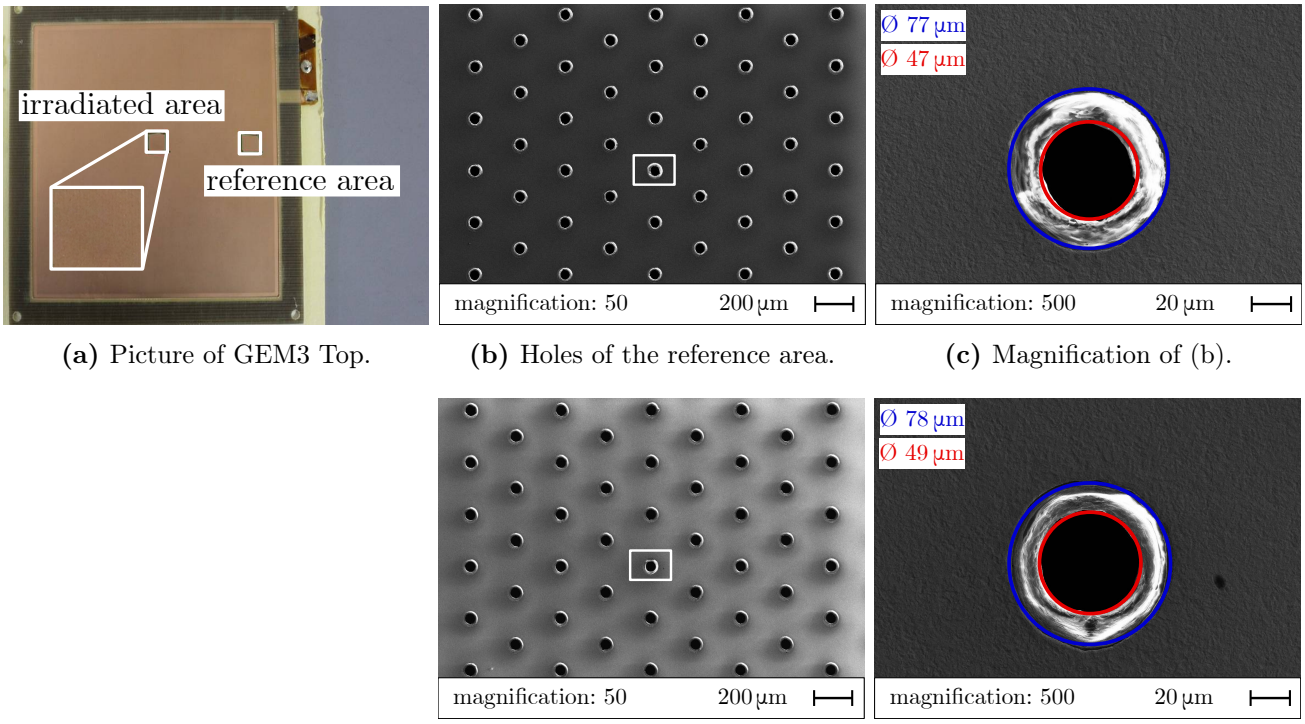

(a) Picture of GEM3 Top.

(b) Holes of the reference area.

(c) Magnification of (b).

(d) Holes of the irradiated area.

(e) Magnification of (d).

Figure C.3: Images of GEM3 Top made with a camera and SEM. Microscopic analysis of GEM3 used in the second measurement testing an empty outgassing box and frames, performed in Ar-CO_2 (70-30). Picture in (a) adapted from [10, p. 9]. SEM images provided by A. T. Pérez Fontenla.

In Figure C.4 the microscopic analysis of GEM4 Top is shown. In the picture in Figure C.4 one can see that also on the irradiated area of GEM4 Top no colorization occurred. The microscopic image in Figure C.4 (e) shows clearly that the kapton of the irradiated area was removed. The magnifications in Figure C.4 (d) and (e) also show another effect of the usage of the GEM. Also here some solidified splashes are visible, which are probably produced by discharges.

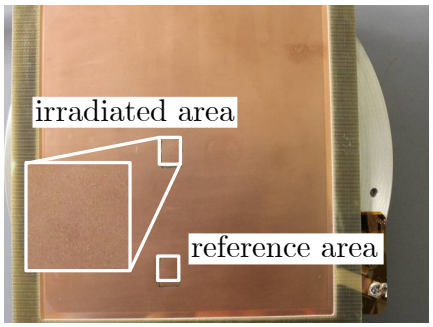

(a) Picture of GEM4 Top.

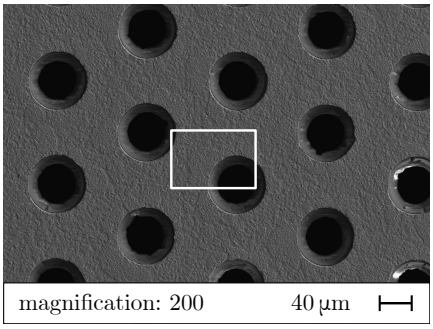

(b) Holes of the reference area.

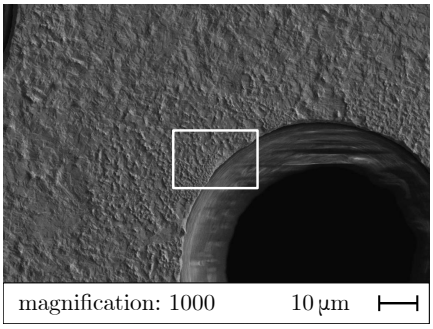

(c) Magnification of (b).

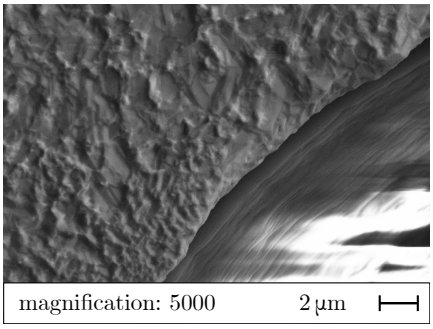

(d) Magnification of (c).

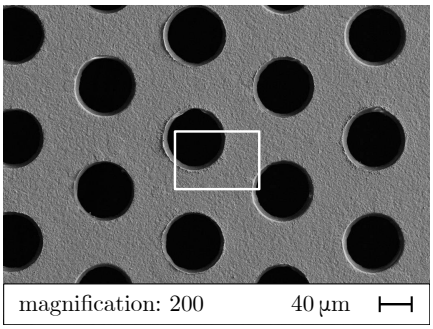

(e) Holes of the irradiated area.

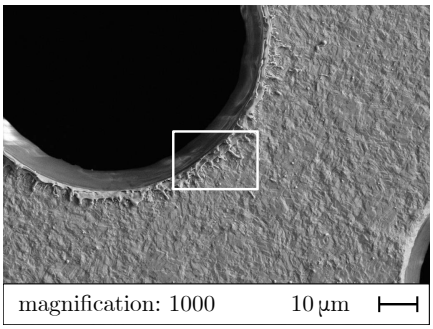

(f) Magnification of (e).

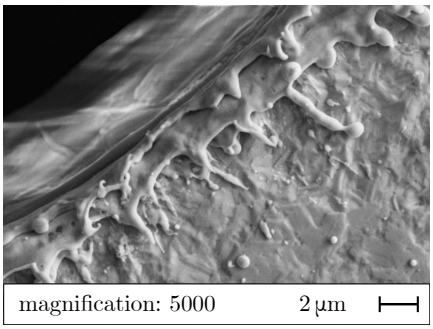

(g) Magnification of (f).

Figure C.4: Images of GEM4 Top made with a camera and SEM, showing the removal of the kapton layer between the electrodes. Microscopic analysis of GEM4 used in the second measurement testing an empty outgassing box and frames, performed in Ar-CO_2 (70-30). Picture in (a), SEM images in (b) and (c) as well as (e) and (f) adapted from [10, p. 10 f.]. SEM images in (d) and (g) provided by A. T. Pérez Fontenla.

C.3 Second measurement testing the epoxy adhesive

The second measurement was performed with a stack of used S-LP-LP-S GEMs. With a quadruple gain of about 6700 a charge of about 60 mC/cm^2 was accumulated in 36 days. The triple GEM stack was tuned to a gain of 4000. Due to the preparation in the laboratory for a beam time, a lot of noise etc. was measured in the setup (noise).

The relative peak position, the energy resolution and the relative anode current are shown in Figure C.5 (a), (b) and (c) respectively. One can see a systematic degradation of the energy resolution. The gain measurement does not show a systematic degradation although some not understood jumps are visible.

Figure C.6 shows two pulse-height spectra of the measurement. By comparing figure (a) and (b) one can see that the pulse-height spectrum became wider. As a result, the escape and photo peak merged together.

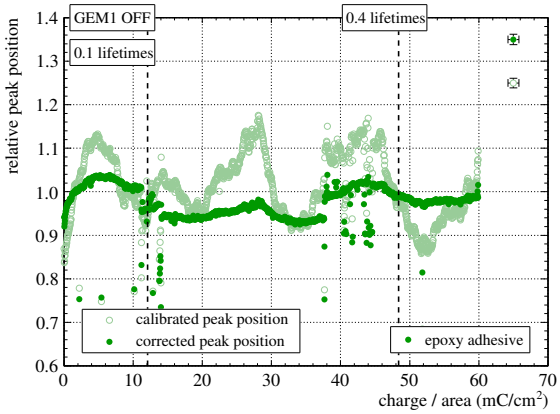

(a) Calibrated and corrected peak position.

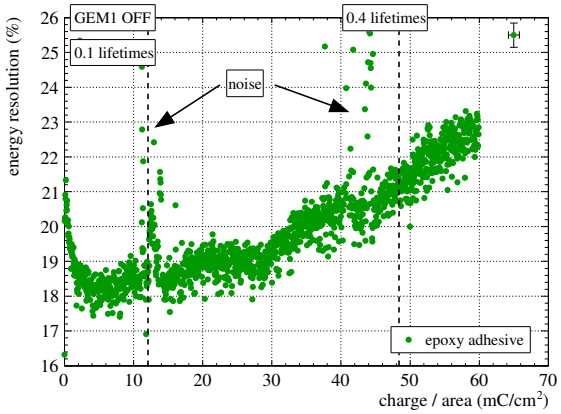

(b) Energy resolution extracted from the calibrated pulse-height spectra.

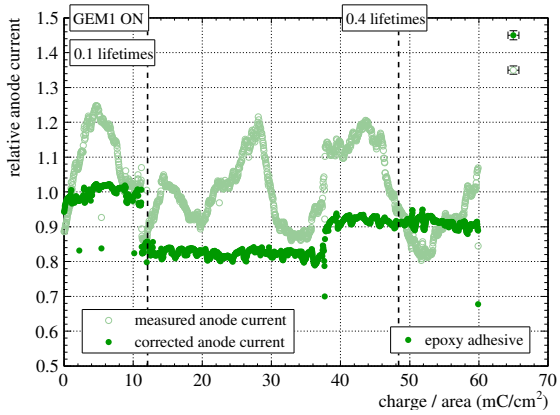

(c) Measured and corrected anode current.

Figure C.5: Results of the second measurement testing the epoxy adhesive, performed in Ar-CO_2 (70-30).

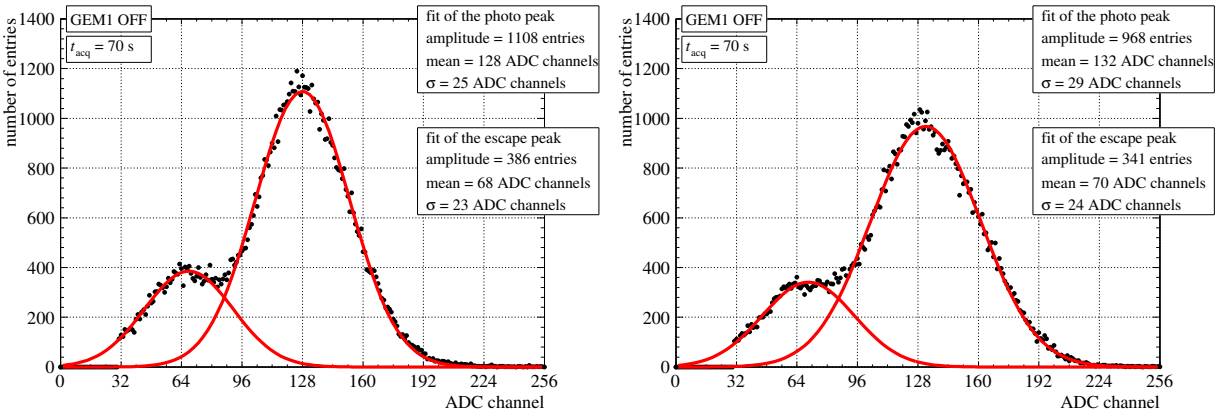

(a) Pulse-height spectrum obtained at 12.1 mC/cm^2 (0.1 lifetimes).

(b) Pulse-height spectrum obtained at 48.4 mC/cm^2 (0.4 lifetimes).

Figure C.6: Two calibrated and fitted pulse-height spectra of the second measurement testing the epoxy adhesive, performed in Ar-CO_2 (70-30).

C.4 Measurement testing the SMDs painted with PU

A second measurement with the SMDs in the outgassing box was performed. This time the resistors were painted with polyurethane (PU). The GEM stack was built with four used S-GEMs. Within 38 days a charge of about 1800 mC/cm^2 could be accumulated.

The results of the measurements is shown in Figure C.8. One can see that within the projected lifetime of the upgraded TPC no change of the gain as well as no degradation of the energy resolution was monitored.

Figure C.7 shows two pulse-height spectra of the measurements. Figure (a) shows that a clear pulse-height spectrum is obtained after 1 lifetime of the TPC.

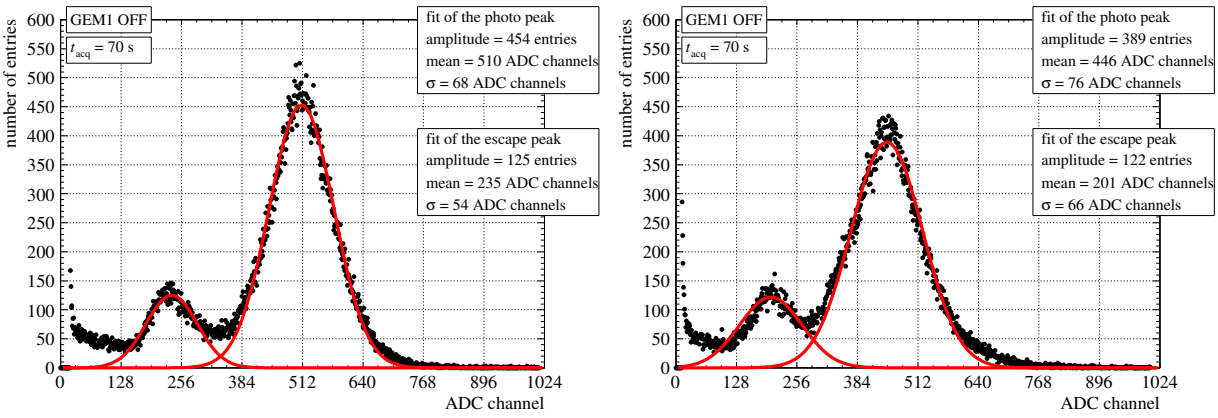

(a) Pulse-height spectrum obtained at 121 mC/cm^2 (1 lifetime).

(b) Pulse-height spectrum obtained at 1815 mC/cm^2 (15 lifetimes).

Figure C.7: Two calibrated and fitted pulse-height spectra of the measurements, performed in Ar-CO_2 (70-30).

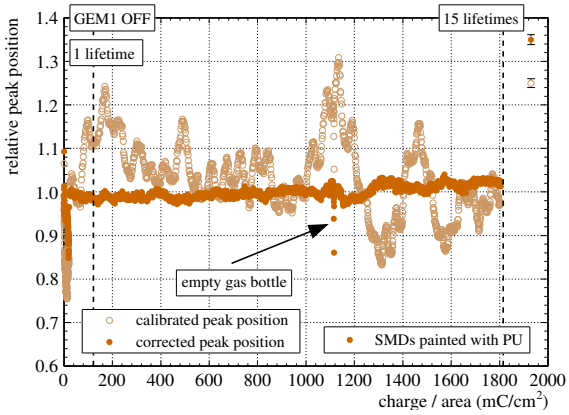

(a) Calibrated and corrected peak position.

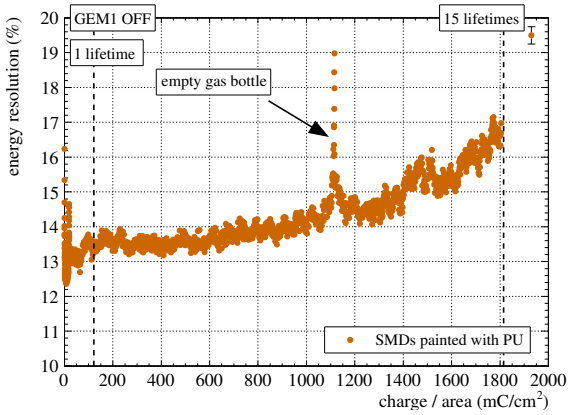

(b) Energy resolution extracted from the calibrated pulse-height spectra.

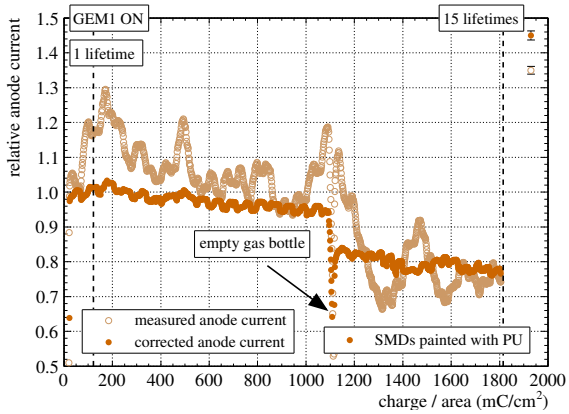

(c) Measured and corrected anode current.

Figure C.8: Results of the second measurement testing the SMDs painted with polyurethane, performed in Ar-CO_2 (70-30).

Appendix D

Additional measurements in Ar-CH_4 (95-5)

D.1 First part of the measurement presented in section 2.4

The third measurement in Ar-CH_4 was performed with a stack of four new GEMs in the S-LP-LP-S configuration. The gain of the quadruple stack was tuned to be 7200. Within 10 days, about 60 mC/cm^2 was accumulated. The triple GEM stack had a gain of about 6000 and a rate of 365 Hz. The oxygen content was increasing during the measurement continuously from 20 ppm to 25 ppm.

The measured and corrected results can be seen in Figure D.2. Also here a drop of the gain was monitored. The energy resolution is fluctuating a lot, because the photo peak was close to the noise. After this measurement no SEM analysis was performed.

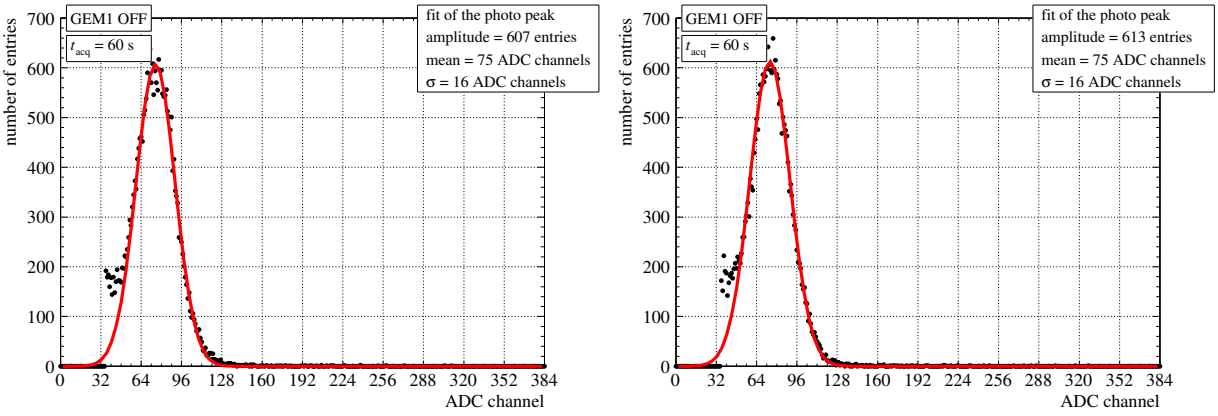

(a) Pulse-height spectrum obtained at 12.1 mC/cm^2 (0.1 lifetimes).

(b) Pulse-height spectrum obtained at 48.4 mC/cm^2 (0.4 lifetimes).

Figure D.1: Two examples of calibrated and fitted pulse-height spectra of the first part of the first measurement, performed in Ar-CH_4 (95-5).

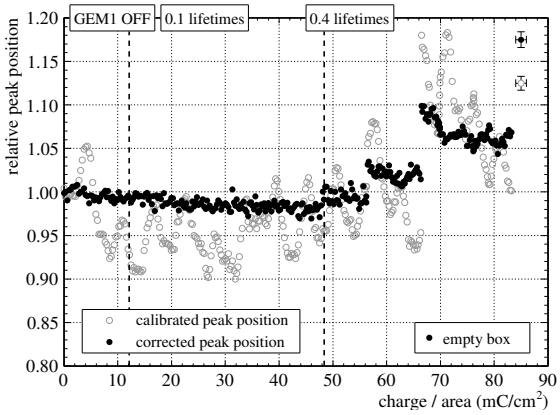

(a) Calibrated and corrected peak position.

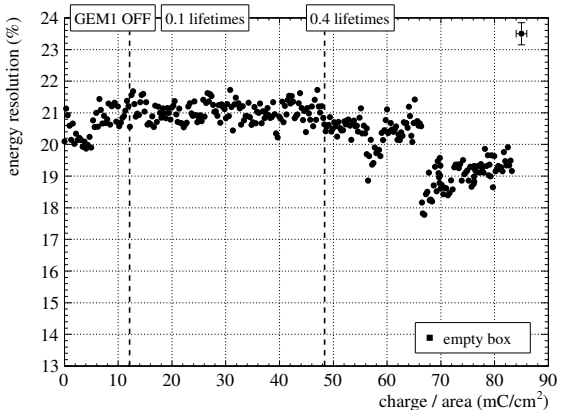

(b) Energy resolution extracted from the calibrated pulse-height spectra.

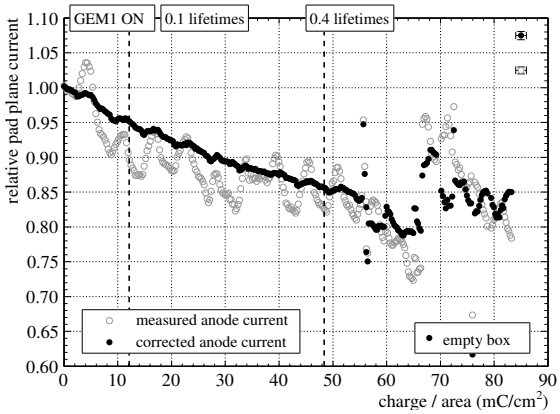

(c) Measured and corrected anode current.

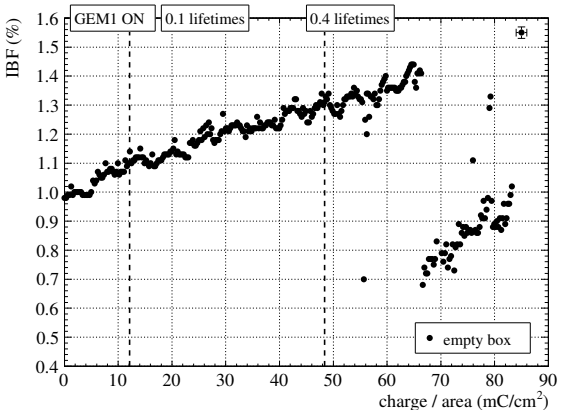

(d) Measured IBF.

Figure D.2: Results of the first part of the first measurement, performed in Ar-CH_4 (95-5).

D.2 Second measurement with empty outgassing box

In the second measurement with Ar-CH_4 was also operated with gas gain of 4200. With a duration of 30 days, an overall accumulated charge of about 55 mC/cm^2 was measured. The gain of the triple GEM stack was set to 3500 with an average rate in E_{T1} of about 254 Hz. The oxygen content of the gas was monitored continuously and was stable around 25 ppm during the complete measurement. In the S-LP-LP-S stack used in this measurement, GEM1 and GEM2 were used in a previous run and GEM3 as well as GEM4 were new GEMs. Due to the announcement of a power cut in the laboratory, the measurement was paused at around 46 mC/cm^2 and the two parts were merged together afterwards. The complete measurement stopped because of a shortcut in GEM1.

The measured and corrected results are shown in Figure D.3. In principle the same behavior was monitored as in the run presented in section 2.4. The peak position dropped by about 7 % and the anode current by 30 %. The IBF decreased continuously and the energy resolution showed also a degradation.

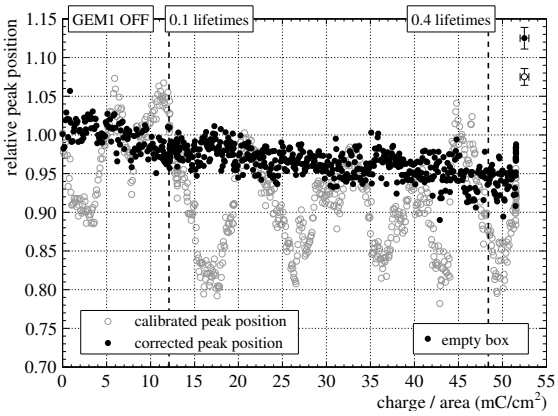

(a) Calibrated and corrected peak position.

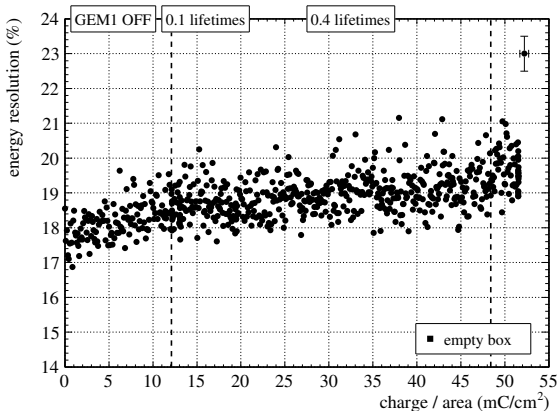

(b) Energy resolution extracted from the calibrated pulse-height spectra.

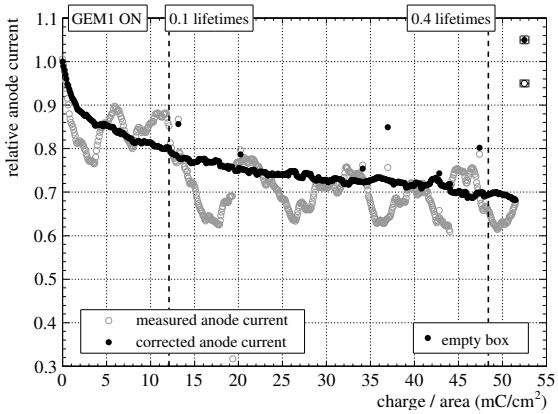

(c) Measured and corrected anode current.

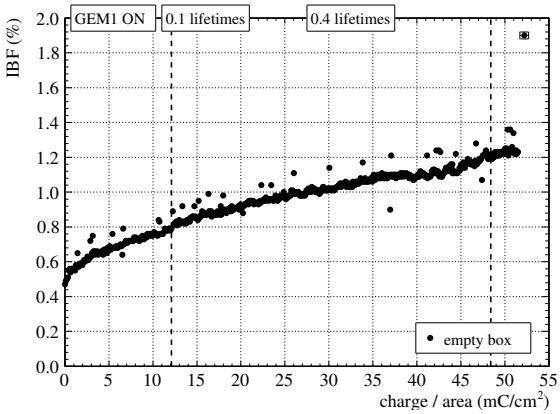

(d) Measured IBF.

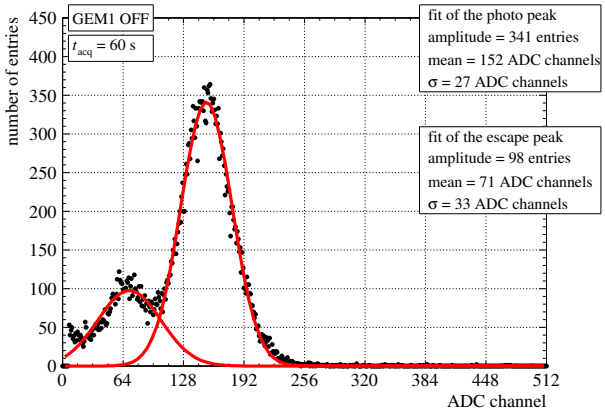

(e) Calibrated and fitted pulse-height spectrum obtained at 12.1 mC/cm^2 (0.1 lifetimes).

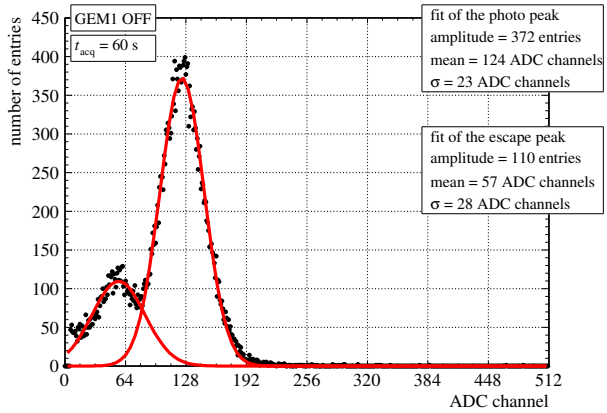

(f) Calibrated and fitted pulse-height spectrum obtained at 48.4 mC/cm^2 (0.4 lifetimes).

Figure D.3: Results of the second measurement, performed in Ar-CH_4 (95-5).

SEM analysis

After the measurement a SEM analysis on GEM3 and GEM4 was carried out. In Figure D.4 (a) one can see a picture of GEM4 Top as well as a magnification of the irradiated area. Again a

colorization of about 1 cm^2 is visible. In Figure D.4 (b) and (c) a magnification of the irradiated and reference area is shown. The corresponding magnifications in (d) and (e) show a single hole. In there one can see that around the hole of the irradiated area, impurities were deposited.

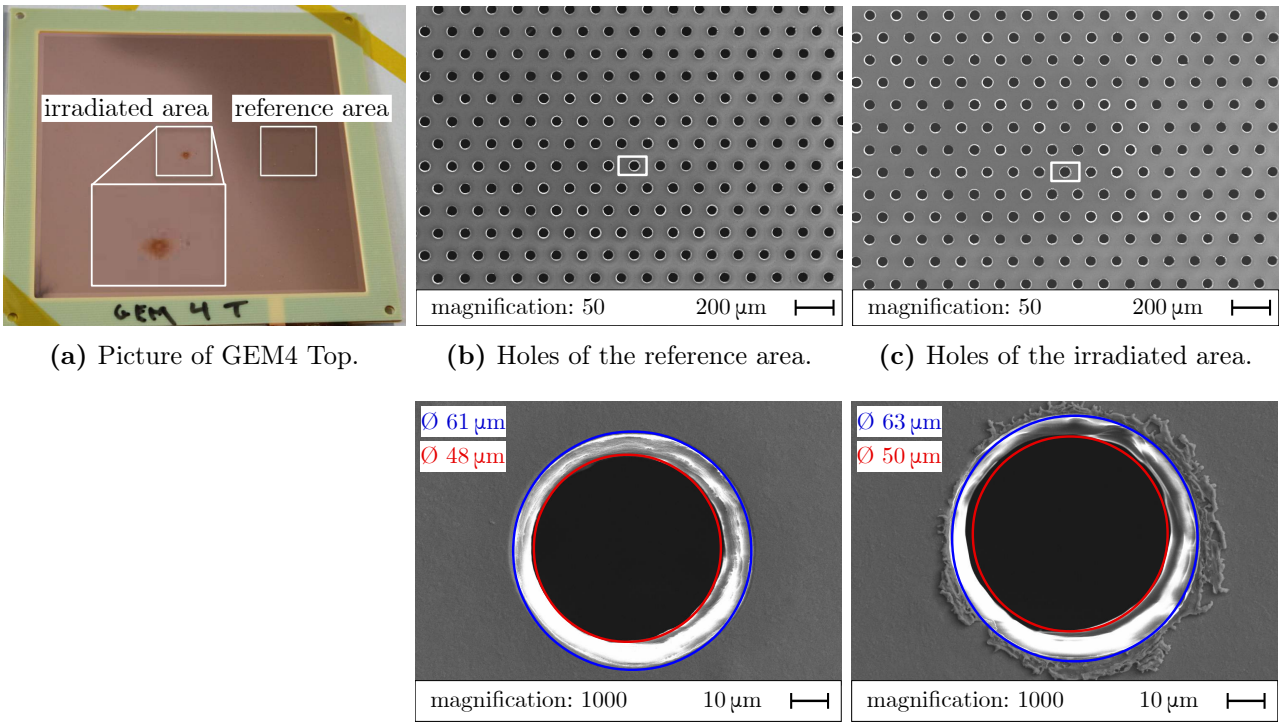

(a) Picture of GEM4 Top. **(b)** Holes of the reference area. **(c)** Holes of the irradiated area.

(d) Magnification of (b). **(e)** Magnification of (c).

Figure D.4: Images of GEM4 Top made with a camera and SEM. Microscopic analysis of GEM4 used in the second measurement, performed in Ar-CH_4 (95-5). Picture and SEM images provided by A. T. Pérez Fontenla.

In addition to the images made with SEs, an analysis with back-scattered electrons (BSEs) was carried out, which can provide information about the chemical composition of the sample. BSEs are beam electrons, which were back-scattered and deflected by the atoms of the probe. Like SEs they are produced in the complete interaction volume of the beam, but in contrast to SEs, BSEs have a much larger kinetic energy and can therefore escape the sample regardless of their distance to the surface. Therefore images made with BSEs do always give information about a few 100 nm depth. The amount of BSEs depends especially on the proton number of the elements in the sample. That is why heavy elements will back-scatter the beam electrons more likely than light elements, which results in a different statistics of BSEs for heavy and light elements. Since images made with BSEs are plotted in a gray-scale, where bright areas correspond to high amount of BSEs and dark areas to low statistics of BSEs, one can distinguish between light and heavy elements. Generally speaking will heavy elements appear brighter and lighter elements will appear darker in the images. [26, p. 16 ff.]

A comparison of the same spot of GEM4 Bottom between images made with SEs and BSEs can be seen in Figure D.5. The comparison of Figure D.5 (a) and (b) shows that the structure at the edge is purly made of copper. Since lighter elements backscatter electrons less likely than heavy elements, one can conclude that these structures are covered with lighter elements than copper. The magnifications in Figure D.5 (c) and (d) shows that there are depositions not

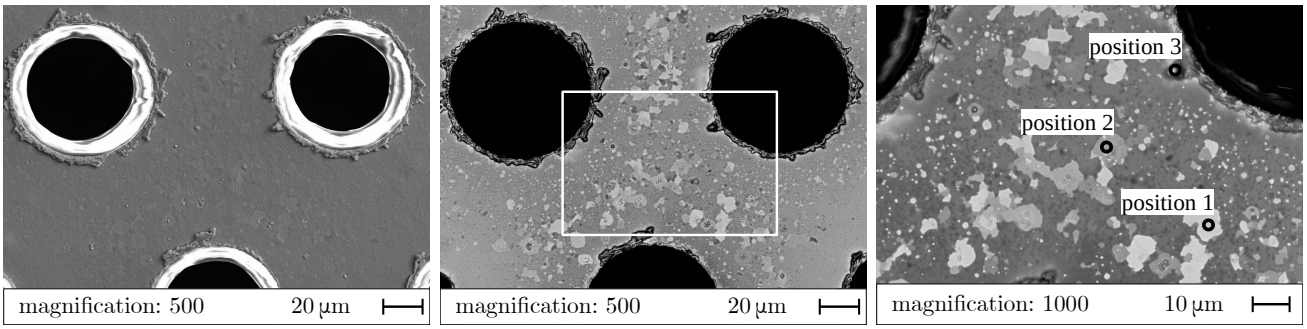

(a) Image made with SEs. **(b)** Image made with BSEs. **(c)** Magnification of (b).

Figure D.5: Images of GEM4 Bottom made with a SEM. Microscopic analysis of GEM4 used in the second measurement, performed in Ar-CH_4 (95-5). SEM and BSE images provided by A. T. Pérez Fontenla.

only close to the edge of the copper electrodes, but also on the surface between the holes. In Figure D.5 (c) one can see that there are elevations on the surface of the electrode. By comparing this spot with the BSE scan in Figure D.5 (d) one can see that the area is irregular covered with elements lighter than copper.

In the three positions of GEM4 Bottom marked in Figure D.5 (c), an energy-dispersive X-ray spectroscopy (EDXS) was carried out. The results can be seen in Figure D.6. It was found that also during this measurement, traces of carbonic impurities were deposited on the electrodes, even on the bottom electrode of GEM4.

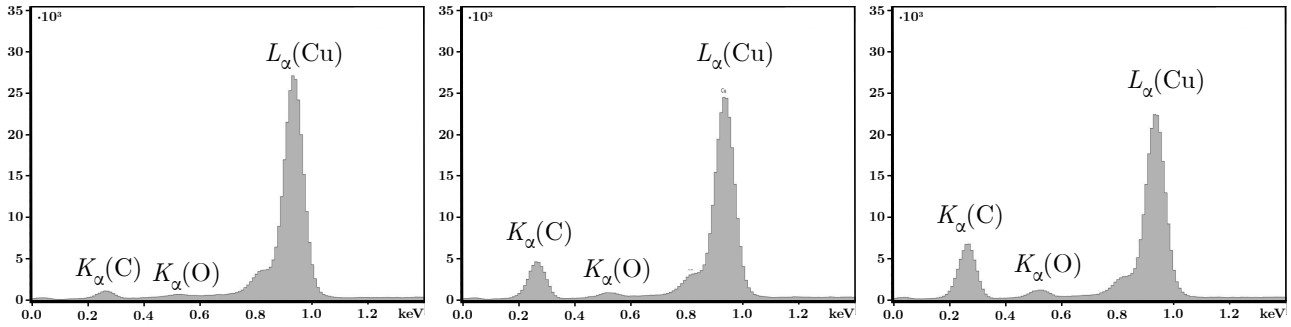

(a) Spectrum taken at position 1. **(b)** Spectrum taken at position 2. **(c)** Spectrum taken at position 3.

Figure D.6: EDXS emission spectra of three different positions on GEM4 Bottom. Elemental analysis of GEM4 used in the second measurement, performed in Ar-CH_4 (95-5). Spectra provided by A. T. Pérez Fontenla.

Bibliography

[1] ALICE Collaboration. Letter of Intent for A Large Ion Collider Experiment. Technical Report CERN-LHCC-93-16, CERN, 1993.
https://cds.cern.ch/record/290825.

[2] D. H. Perkins. *Introduction to High Energy Physics*. Cambridge University Press, fourth edition, 2000.
https://doi.org/10.1017/CBO9780511809040.

[3] ALICE Collaboration. Centrality Dependence of the Charged-Particle Multiplicity Density at Midrapidity in Pb-Pb Collisions at $\sqrt{s_{\mathrm{NN}}} = 5.02\,\mathrm{TeV}$. *Physical Review Letters*, 116:1–12, 2016.
https://doi.org/10.1103/PhysRevLett.116.222302.

[4] ALICE Collaboration. The ALICE experiment at the CERN LHC. *Journal of Instrumentation*, 3:1–245, 2008.
https://doi.org/10.1088/1748-0221/3/08/S08002.

[5] ALICE Collaboration. Upgrade of the ALICE Experiment: Letter Of Intent. Technical Report CERN-LHCC-2012-012, CERN, 2012.
https://doi.org/10.1088/0954-3899/41/8/087001.

[6] C. Fabjan and J. Schukraft. The story of ALICE: Building the dedicated heavy ion detector at LHC. arXiv:1101.1257 [physics.ins-det], 2011.
https://arxiv.org/abs/1101.1257.

[7] M. Brice. CERN-PHOTO-201904-082-6, 5$^{\mathrm{th}}$ April 2019.
https://cds.cern.ch/record/2670210.

[8] ALICE TPC Collaboration. The ALICE TPC, a large 3-dimensional tracking device with fast readout for ultra-high multiplicty events. *Nuclear Instruments and Methods in Physics Research Section A: Accelerators, Spectrometers, Detectors and Associated Equipment*, 622:316–367, 2010.
https://doi.org/10.1016/j.nima.2010.04.042.

[9] ALICE Collaboration. Technical Design Report for the Upgrade of the ALICE Time Projection Chamber. Technical Report CERN-LHCC-2013-020, CERN, 2014.
https://cds.cern.ch/record/1622286.

[10] A. T. Pérez Fontenla. Scanning Electron Microscopy (SEM) and Focus Ion Beam (FIB) analysis of heavily irradiated Gas Electron Multipliers (GEMs). Technical Report EDMS NO: 1719614 v. 1, Engineering Departement of CERN, 2016.
https://edms.cern.ch/document/1719614/1.

[11] F. Sauli. GEM: A new concept for electron amplification in gas detectors. *Nuclear Instruments and Methods in Physics Research Section A: Accelerators, Spectrometers, Detectors and Associated Equipment*, 386:531 – 534, 1997.
https://doi.org/10.1016/S0168-9002(96)01172-2.

[12] F. Sauli. The gas electron multiplier (GEM): Operating principles and applications. *Nuclear Instruments and Methods in Physics Research Section A: Accelerators, Spectrometers, Detectors and Associated Equipment*, 805:2 – 24, 2015.
https://doi.org/10.1016/j.nima.2015.07.060.

[13] ALICE Collaboration. Addendum to the Technical Design Report for the Upgrade of the ALICE Time Projection Chamber. Technical Report CERN-LHCC-2015-002, CERN, 2015.
https://cds.cern.ch/record/1984329.

[14] C. Lippmann. A continuous-readout TPC for the ALICE upgrade. Presentation at the EPS Conference on High Energy Physics in Venice, 8$^{\text{th}}$ July 2017.
https://alice-conferences.web.cern.ch/node/28808.

[15] ALICE Collaboration. Technical Design Report of the Time Projection Chamber. Technical Report CERN-LHCC-2000-001, CERN, 2000.
https://cds.cern.ch/record/451098.

[16] ALICE Collaboration. Pseudorapidity and transverse-momentum distributions of charged particles in proton-proton collisions at $\sqrt{s} = 13\,\text{TeV}$. *Physics Letters B*, 753:319 – 329, 2015.
https://doi.org/10.1016/j.physletb.2015.12.030.

[17] M. Capeáns. Aging and materials: lessons for detectors and gas systems. *Nuclear Instruments and Methods in Physics Research Section A: Accelerators, Spectrometers, Detectors and Associated Equipment*, 515:73 – 88, 2003.
https://doi.org/10.1016/j.nima.2003.08.134.

[18] G. Charpak, R. Bouclier, T. Bressani, J. Favier, and Č. Zupančič. The use of multiwire proportional counters to select and localize charged particles. *Nuclear Instruments and Methods*, 86:262 – 268, 1968.
https://doi.org/10.1016/0029-554X(68)90371-6.

[19] Lawrence Berkeley Laboratory (LBL). *Proceedings of the Workshop on Radiation Damage to Wire Chambers*, Berkeley, 1986.
https://cds.cern.ch/record/110508.

[20] Deutsches Elektronen-Synchrotron (DESY). *Aging phenomena in gaseous detectors*, Hamburg, 2001.
www.desy.de/agingworkshop/abstracts_v2.ps.

[21] M. C. Altunbas, K. Dehmelt, S. Kappler, B. Ketzer, L. Ropelewski, F. Sauli, and F. Simon. Aging measurements with the Gas Electron Multiplier (GEM). *Nuclear Instruments and Methods in Physics Research Section A: Accelerators, Spectrometers, Detectors and Associated Equipment*, 515:249 – 254, 2003.
https://doi.org/10.1016/j.nima.2003.09.006.

[22] S. Biswas, D. J. Schmidt, A. Abuhoza, U. Frankenfeld, C. Garabatos, J. Hehner, V. Kleipa, T. Morhardt, C.J. Schmidt, H. R. Schmidt, and J. Wiechula. Development of a GEM based detector for the CBM Muon Chamber (MUCH). *Journal of Instrumentation*, 8:1 – 17, 2013.
https://doi.org/10.1088/1748-0221/8/12/C12002.

[23] E. P. Bertin. *Introduction to X-Ray Spectrometric Analysis*. Springer Science + Business Media New York, 1978.
https://doi.org/10.1007/978-1-4899-2204-5.

[24] W. Blum, W. Riegler, and L. Rolandi. *Particle Detection with Drift Chambers*. Springer-Verlag Berlin Heidelberg, second edition, 2008.
https://doi.org/10.1007/978-3-540-76684-1.

[25] P. Gasik. Building a large-area GEM-based readout chamber for the upgrade of the ALICE TPC. *Nuclear Instruments and Methods in Physics Research Section A: Accelerators, Spectrometers, Detectors and Associated Equipment*, 845:222 – 225, 2016.
https://doi.org/10.1016/j.nima.2016.06.070.

[26] J. I. Goldstein, D. E. Newbury, J. R. Michael, N. W. M. Ritchie, J. H. J. Scott, and D. C. Joy. *Scanning Electron Microscopy and X-Ray Microanalysis*. Springer Verlag New York, fourth edition, 2018.
https://doi.org/10.1007/978-1-4939-6676-9.

[27] A. Karadzhinova, A. Nolvi, R. Veenhof, E. Tuominen, E. Hæggström, and I. Kassamakov. Impact of GEM foil hole geometry on GEM detector gain. *Journal of Instrumentation*, 10:1 – 15, 2015.
https://doi.org/10.1088/1748-0221/10/12/P12014.

[28] H. Stelzer, D. Vranić, C. Garabatos, G. Augustinski, P. Braun-Munzinger, H. Daues, J. Fiess, U. Frankenfeld, P. Glässel, J. Hehner, M. Ivanov, R. Renfordt, H. Samn, H. R. Schmidt, and B. Windelband. The ALICE TPC Readout Chamber: From Prototypes to Series Production. Technical Report ALICE-INT-2003-017, CERN, 2003.
https://edms.cern.ch/document/384259/2.

[29] W. R. Leo. *Techniques for Nuclear and Particle Physics Experiments - A How-to Approach*. Springer-Verlag Berlin Heidelberg, second revised edition, 1994.
https://doi.org/10.1007/978-3-642-57920-2.

[30] A. T. Pérez Fontenla. Microscope investigation of a Gas Electron Multiplier (GEM) after long-term irradiation. Technical Report EDMS NO: 2150714 v. 1, Engineering Departement of CERN, 2019.
https://edms.cern.ch/document/2150714/1.

[31] J. A. Bearden. X-Ray Wavelengths. *Reviews of Modern Physics*, 39:78 – 124, 1967.
https://doi.org/10.1103/RevModPhys.39.78.

[32] M. Jung. *Investigation of GEM amplification structures for the ALICE TPC Upgrade (original title: Untersuchungen von GEM-Verstärkungsstrukturen für den ALICE TPC Upgrade)*. Bachelorthesis, Goethe University Frankfurt, 2015.
https://www.uni-frankfurt.de/46295382/Bachelor_Theses.

[33] A. Deisting, C. Garabatos, and A. Szabo. Ion mobility measurements in Ar-CO_2, Ne-CO_2 and Ne-CO_2-N_2 mixtures, and the effect of water. *Nuclear Instruments and Methods in Physics Research Section A: Accelerators, Spectrometers, Detectors and Associated Equipment*, 904:1 – 8, 2018.
https://doi.org/10.1016/j.nima.2018.07.008.

[34] D. Zavazieva. *Degradation in Gas Electron Multipliers under the influence of X-ray flux of high density (original title: Деградационные изменения в Газовых Электронных Умножителях под воздействием плотных потоков рентгеновского излучения).* Bachelorthesis, National Research Tomsk Polytechnic University, 2017.
http://earchive.tpu.ru/bitstream/11683/39790/1/TPU394797.pdf.

[35] R. Bouclier, M. Capeáns, C. Garabatos, R. D. Heuer, M. Jeanrenaud, T. C. Meyer, F. Sauli, and K. Silander. Results of wire chamber ageing tests with CH_4- and DME-based gas mixtures. *Nuclear Instruments and Methods in Physics Research Section A: Accelerators, Spectrometers, Detectors and Associated Equipment*, 346:114 – 119, 1994.
https://doi.org/10.1016/0168-9002(94)90694-7.

[36] A. Algeri, H. G. Fischer, S-O. Holmgren, and M. Szeptycka. Anode wire ageing in proportional counters: the problem of analog response. *Nuclear Instruments and Methods in Physics Research Section A: Accelerators, Spectrometers, Detectors and Associated Equipment*, 338:348 – 367, 1994.
https://doi.org/10.1016/0168-9002(94)91318-8.

[37] National Institute of Standards and Technology. *XCOM: Photon Cross Sections Database*, retrieved 23rd March 2019.
https://dx.doi.org/10.18434/T48G6X.

[38] National Institute of Standards and Technology. *NIST Chemistry WebBook*, retrieved 23rd March 2019.
https://doi.org/10.18434/T4D303.

[39] National Institute of Standards and Technology. *Chapter 2: X-Ray Mass Attenuation Coefficients*, retrieved 23rd March 2019.
https://dx.doi.org/10.18434/T4D01F.

[40] J. Ordan. CERN-PHOTO-201901-004-3, 14th January 2019.
https://cds.cern.ch/record/2653650.

List of Figures

1 Picture of the open ALICE Experiment, cut out from [40] 1

1.1 The ALICE experiment 10
1.2 Schematic drawing and picture of the ALICE Time Projection Chamber 11
1.3 Wire geometry of the IROC 12
1.4 Development of an electron avalanche close to an anode wire 12
1.5 Images of a GEM made by a Scanning Electron Microscope 14
1.6 2-dimensional projections of a 3-dimensional simulated single GEM hole 14
1.7 GEM stack with the S-LP-LP-S configuration 15
1.8 Pulse-height spectrum of a ^{55}Fe source in Ne-CO_2-N_2 (90-10-5) 16

2.1 Experimental setup in the RD51 laboratory 20
2.2 Overview of the gas system 21
2.3 The GEM detector used for the ageing tests 22
2.4 Overview of the readout scheme 23
2.5 Energy calibration of the ADC using a pulse-height spectrum obtained in Ar-CO_2 (70-30) 24
2.6 Flowchart of the LabVIEW program 25
2.7 Screenshots of the LabVIEW program 26
2.8 Example of the normalization procedure 29
2.9 Pictures of the samples of the tested components 30
2.10 Measured and corrected results of the first measurement testing an empty outgassing box, screws and frames, performed in Ar-CO_2 (70-30) 32
2.11 Two examples of calibrated and fitted pulse-height spectra of the first measurement testing an empty outgassing box, screws and frames, performed in Ar-CO_2 (70-30) 33
2.12 Images of GEM4 Top made with a camera, digital USB microscope and SEM, showing top views of the foil. Microscopic analysis of GEM4 used in the first measurement testing an empty outgassing box, screws and frames, performed in Ar-CO_2 (70-30) 35
2.13 Images of GEM4 Top made with a SEM, showing single holes of the foil. Microscopic analysis of GEM4 used in the first measurement testing an empty outgassing box, screws and frames, performed in Ar-CO_2 (70-30) 36
2.14 Images of GEM4 and images of cross sections of GEM4 made with a SEM, showing the reduction of the kapton layer between the electrodes. Microscopic analysis of GEM4 used in the second measurement testing an empty outgassing box and frames, performed in Ar-CO_2 (70-30) 37
2.15 Results of the first measurement testing the epoxy adhesive, performed in Ar-CO_2 (70-30) 39

2.16 Results of the first measurement testing the SMDs cleaned with acetone, performed in Ar-CO_2 (70-30) . . . 41
2.17 Results of the second part of the first measurement, performed in Ar-CH_4 (95-5) 43
2.18 Images of GEM4 Top, made with a camera and SEM, showing top views of the foil. Microscopic analysis of GEM4 used in the first measurement performed in Ar-CH_4 (95-5) . . . 44
2.19 Images made with a SEM and EDXS spectra of GEM4 Top. Microscopic and elemental analysis of GEM4 used in the first measurement performed in Ar-CH_4 (95-5) . . . 45
2.20 Images of GEM4 Top made with a camera and SEM, showing a comparison of irradiated and non-irradiated hole diameters. Microscopic analysis of GEM4 used in the second measurement performed in Ar-CH_4 (95-5) . . . 46
2.21 Results of the measurement performed in Ne-CO_2-N_2 (90-10-5) . . . 48

3.1 Schematic drawing of the simulated setup of the Garfield^{++} simulation . . . 49
3.2 Simulated elementary cells of a GEM . . . 50
3.3 2-dimensional projection of ion drift lines inside a simulated GEM hole . . . 51
3.4 Elementary cell of primary electrons above the simulated GEM . . . 52
3.5 Simulated distributions of gain and multiplication of a ^{55}Fe source for three different hole diameters . . . 53
3.6 Relative change in gain and multiplication as a function of the inner diameter of the GEM hole . . . 53
3.7 Distribution of the production points of secondary electrons inside a GEM hole . 54
3.8 Two examples of summing Gaussian distributions . . . 55
3.9 Change in energy resolution and gain for different etching stages . . . 56
3.10 Endpoints of the simulated ions on the top electrode . . . 57

4.1 Comparison of the top electrode between measurement and simualtion . . . 60
4.2 Comparison of the ageing measurements performed in Ar-CH_4 (95-5) and Ar-CO_2 (70-30) . . . 62
4.3 Computed gain drop for different ageing rates R' . . . 63
4.4 Schematic drawing of top views and side views of a GEM, single-wire proportional counter and MWPC, showing the irradiated areas and drift lines. . . . 64
4.5 Fitted relativ gain drop of the first and second measurement performed in Ar-CH_4 (95-5). . . . 65
4.6 Comparison of ageing rates for GEMs, single-wire proportional counters and MWPCs . . . 66

B.1 Schematic drawing of the triple GEM detector used to measure the source profile 78
B.2 Projections of the measured X-ray distributions . . . 78
B.3 Standard deviation of the X-ray distributions as a function of the distance between source and GEM1 . . . 79
B.4 Attenuation of 5.89 keV X-rays in the different gas mixtures . . . 81

C.1 Images of GEM3 Top made with a camera and SEM, showing the removal of the kapton layer between the electrodes. Microscopic analysis of GEM3 used in the first measurement testing an empty outgassing box, screws and frames, performed in Ar-CO_2 (70-30) . . . 83

C.2 Results of the second measurement testing an empty outgassing box and frames, performed in Ar-CO_2 (70-30). 85
C.3 Images of GEM3 Top made with a camera and SEM. Microscopic analysis of GEM3 used in the second measurement testing an empty outgassing box and frames, performed in Ar-CO_2 (70-30) 86
C.4 Images of GEM4 Top made with a camera and SEM, showing the removal of the kapton layer between the electrodes. Microscopic analysis of GEM4 used in the second measurement testing an empty outgassing box and frames, performed in Ar-CO_2 (70-30) 87
C.5 Results of the second measurement testing the epoxy adhesive, performed in Ar-CO_2 (70-30) 88
C.6 Two examples of calibrated and fitted pulse-height spectra of the second measurement testing the epoxy adhesive, performed in Ar-CO_2 (70-30) 89
C.7 Two examples of calibrated and fitted pulse-height spectra of the second measurement testing the SMDs painted with polyurethane, performed in Ar-CO_2 (70-30) 89
C.8 Results of the second measurement testing the SMDs painted with polyurethane, performed in Ar-CO_2 (70-30) 90

D.1 Two examples of calibrated and fitted pulse-height spectra of the first part of the first measurement, performed in Ar-CH_4 (95-5) 91
D.2 Results of the first part of the first measurement, performed in Ar-CH_4 (95-5) . 92
D.3 Results of the second measurement, performed in Ar-CH_4 (95-5) 93
D.4 Images of GEM4 Top made with a camera and SEM. Microscopic analysis of GEM4 used in the second measurement, performed in Ar-CH_4 (95-5) 94
D.5 Images of GEM4 Bottom made with a SEM. Microscopic analysis of GEM4 used in the second measurement, performed in Ar-CH_4 (95-5) 95
D.6 EDXS emission spectra of three different positions on GEM4 Bottom. Elemental analysis of GEM4 used in the second measurement, performed in Ar-CH_4 (95-5) 95

List of Tables

1.1 Overview of the different GEM pitches 15

2.1 Number of primary electrons ejected per 5.89 keV X-ray 27
2.2 Irradiated areas for the different gas mixtures 27
2.3 Tested components, materials and their purpose 30
2.4 Baseline voltage setting of the GEM-based TPC in Ne-CO_2-N_2 (90-10-5) 47

3.1 Parameters of the simulated gain distributions 55
3.2 Different stages of etching and their hole geometries 56

A.1 Effective ionization potential W for the individual constituents of the gas mixtures used in the ageing setup 75
A.2 Effective ionization potential W_{m} and number of electrons per X-ray N_{e} for the gas mixtures 76

B.1 Mass attenuation coefficients, molar masses and densities for the constituents of the gas mixtures 79
B.2 Volume fractions and mass fractions of the constituents of the mixtures and mean molar masses for the gas mixtures 80
B.3 Mass attenuation coefficients, densities, attenuation coefficients and mean free path of the gas mixtures used in the ageing tests 81
B.4 Irradiated areas for the different gas mixtures 82

List of Abbreviations

ADC	**A**nalog-to-**D**igital **C**onverter
ALICE	**A** **L**arge **I**on **C**ollider **E**xperiment
BSE	**B**ack-**S**cattered **E**lectron
CERN	**C**onseil **E**uropéen pour la **R**echerche **N**ucléaire
DESY	**D**eutsches **E**lektronen-**Sy**nchrotron
EDXS	**E**nergy-**D**ispersive **X**-ray **S**pectroscopy
FIB	**F**ocused **I**on **B**eam
FWHM	**F**ull **W**idth at **H**alf **M**aximum
GEM	**G**as **E**lectron **M**ultiplier
HV	**H**igh **V**oltage
IBF	**I**on **B**ack**f**low
IROC	**I**nner **R**ead**o**ut **C**hamber
LBL	**L**awrence **B**erkeley **L**aboratory
LHC	**L**arge **H**adron **C**ollider
LP	**L**arge **P**itch (280 µm)
MCA	**M**ulti**c**hannel **A**nalyzer
MP	**M**edium **P**itch (200 µm)
MWPC	**M**ulti-**W**ire **P**rotortional **C**hamber
NIM	**N**uclear **I**nstrumentation **M**odule
OROC	**O**uter **R**ead**o**ut **C**hamber
Pb-Pb	Lead-Lead collisions (Latin: **P**lum**b**um)
pp	**P**roton-**P**roton collisions
PU	**P**oly**u**rethane

QGP **Q**uark-**G**luon **P**lasma

RS-232 **R**ecommended **S**tandard 232

ROC **R**ead**o**ut **C**hamber

S **S**tandard pitch (140 µm)

SE **S**econdary **E**lectron

SEM **S**canning **E**lectron **M**icroscope

SHV **S**afe **H**igh **V**oltage

SMD **S**urface **M**ounted **D**evice

SP **S**mall **P**itch (90 µm)

TPC **T**ime **P**rojection **C**hamber

UV **U**ltra**v**iolet

Xe-Xe **Xe**non-**Xe**non collisions

Zusammenfassung in deutscher Sprache gemäß § 35 Abs. 3 Allgemeine Bestimmungen für Bachelor- und Masterstudiengänge der Johann Wolfgang Goethe-Universität Frankfurt am Main vom 16.04.2008 in der Fassung vom 13.04.2011.

Für den Umbau der Spurendriftkammer des ALICE Experiments am CERN wurden Langzeitstudien über das Verhalten von Gas-Elektronen-Vervielfachern unter hoher Bestrahlung vorgenommen. Dafür wurde ein Messstand mit einem Detektor bestehend aus vier Lagen dieser Verstärkungsfolien aufgebaut und in Ar-CO_2 und Ne-CO_2-N_2 Gasmischungen betrieben. Es wurde untersucht, ob der Detektor nach einem Ladungsäquivalent von 10 Jahren, sowohl die Gasverstärkung, als auch die Energieauflösung beibehält. Desweiteren wurden Materialien, die für den Umbau benötigt werden, auf etwaige Ausgasungseffekte und daraus folgenden Auswirkungen auf den Detektor untersucht.

Die Studien zeigten, dass der Detektor einen Betrieb unter einer viel höheren Gasverstärkung ohne Leistungseinbußen aushält. Die getesten Materialien zeigten keine negativen Auswirkungen auf die Detektoreigenschaften. Für den getesteten Kleber konnte keine endgültige Schlussfolgerung gezogen werden.

Ein bis dahin unbekanntes Phänomen wurde bei dem Betrieb unter sehr hoher Gasverstärkung entdeckt. Die Geometrie der Löcher in den Verstärkungsfolien änderte sich nach intensiver Bestrahlung, was zu einem dramatischen Verlust der Energieauflösung führte. Um dies genauer zu untersuchen wurden Simulationen mit der Garfield^{++} Software durchgeführt. Es konnte herausgefunden werden, dass eine Änderung der Lochgeometrien in mehreren Folien zu einem Anstieg der lokalen Verstärkungsvariationen führt, was in einem Verlust der Energieauflösung resultiert. Da dieser Effekt bei sehr viel höheren Gasverstärkungen und deponierten Ladungsmengen, als während des Betriebs der Spurendriftkammer, auftritt, ist dieses Phänomen innerhalb deren Lebensdauer nicht relevant.

Zuletzt wurden noch Messungen in einer Ar-CH_4 Gasmischungen durchgeführt. Diese zeigten einen sehr schnellen und drastischen Effekt auf die Detektoreigenschaften. Ein Abfall der Verstärkung und eine Verschlechterung der Energieauflösung wurden beobachtet. Wie bereits aus Alterungsprozessen von Vieldrahtkammern, die in Methangasen betrieben wurden, bekannt ist, bildeten sich Ablagerungen auf den Elektroden. Ein Vergleich der Alterungsraten von Proportionalzählrohren, Drahtkammern und Gas-Elektronen-Vervielfachern konnte angefertigt werden.

Erklärung gemäß § 30 Abs. 12 Ordnung für den Bachelor und den Masterstudiengang Physik der Johann Wolfgang Goethe-Universität Frankfurt am Main vom 24.04.2013.

Hiermit erkläre ich, dass ich die Arbeit selbstständig und ohne Benutzung anderer als der angegebenen Quellen und Hilfsmittel verfasst habe. Alle Stellen der Arbeit, die wörtlich oder sinngemäß aus Veröffentlichungen oder anderen fremden Texten entnommen wurden, sind von mir als solche kenntlich gemacht worden. Ferner erkläre ich, dass die Arbeit nicht - auch nicht auszugsweise - für eine andere Prüfung verwendet wurde.

Michael Jung

Frankfurt am Main, den 15. Mai 2019